SLAC-R-604

Radiative Decays of the B Meson*

Hirohisa Alexander Tanaka

Stanford Linear Accelerator Center
Stanford University
Stanford, CA 94309

SLAC-Report-604

Prepared for the Department of Energy
under contract number DE-AC03-76SF00515

Printed in the United States of America. Available from the National Technical Information Service, U.S. Department of Commerce, 5285 Port Royal Road, Springfield, VA 22161.

* Ph.D. thesis, Stanford University, Stanford, CA 94309.

RADIATIVE DECAYS OF THE B MESON

A DISSERTATION
SUBMITTED TO THE DEPARTMENT OF PHYSICS
AND THE COMMITTEE ON GRADUATE STUDIES
OF STANFORD UNIVERSITY
IN PARTIAL FULFILLMENT OF THE REQUIREMENTS
FOR THE DEGREE OF
DOCTOR OF PHILOSOPHY

Hirohisa Alexander Tanaka
August 2002

I certify that I have read this dissertation and that, in my opinion, it is fully adequate in scope and quality as a dissertation for the degree of Doctor of Philosophy.

Colin P. Jessop
(Principal Advisor)

I certify that I have read this dissertation and that, in my opinion, it is fully adequate in scope and quality as a dissertation for the degree of Doctor of Philosophy.

David Goldhaber-Gordon

I certify that I have read this dissertation and that, in my opinion, it is fully adequate in scope and quality as a dissertation for the degree of Doctor of Philosophy.

JoAnne L. Hewett

I certify that I have read this dissertation and that, in my opinion, it is fully adequate in scope and quality as a dissertation for the degree of Doctor of Philosophy.

David W.G.S. Leith

I certify that I have read this dissertation and that, in my opinion, it is fully adequate in scope and quality as a dissertation for the degree of Doctor of Philosophy.

Vera G. Lüth

I certify that I have read this dissertation and that, in my opinion, it is fully adequate in scope and quality as a dissertation for the degree of Doctor of Philosophy.

Rafe H. Schindler

Approved for the University Committee on Graduate Studies:

Forward

The radiative decays of the B meson to the final states $K^*(892)\gamma$ and $\rho(770)\gamma$ proceed through virtual effective flavor-changing neutral current processes which are sensitive to contributions from high mass scales from within the Standard Model of particle interactions and from possible new physics. In the context of the Standard Model, these transitions are of interest in probing the weak interaction behavior of the top quark. In particular, the ratio of branching fractions for the two processes can be used to extract the ratio of Cabibbo-Kobayashi-Maskawa matrix elements $|V_{td}/V_{ts}|$. Potential new physics contributions in these virtual transitions may induce new sources of direct CP violation and enhancement or suppression of the rate of these processes.

The $B \to K^*\gamma$ is a manifestation of the $b \to s\gamma$ radiative transition. This process has been previously observed by the CLEO collaboration and its branching fraction measured. While the theoretical prediction for the inclusive rate of $b \to s\gamma$ transitions is more robust than that of the exclusive $B \to K^*\gamma$, the prospects for precise measurements of $\mathcal{B}[B \to K^*\gamma]$ and direct CP violation in this channel has attracted considerable attention. The analysis described here represents an improved measurement of the $B \to K^*\gamma$ branching factions and a more sensitive search for direct CP violation.

In 22.7×10^6 $B\overline{B}$ events collected by the *BABAR* detector in 1999-2000, we measure:

$$\mathcal{B}[B^0 \to K^{*0}\gamma] = 4.23 \pm 0.40(\text{stat.}) \pm 0.22(\text{syst.}) \times 10^{-5}$$
$$\mathcal{B}[B^+ \to K^{*+}\gamma] = 3.83 \pm 0.62(\text{stat.}) \pm 0.22(\text{syst.}) \times 10^{-5}$$

We find no evidence for direct CP violation in the decays and constrain $-0.170 < A_{CP} < 0.082$ at 90% Confidence Level.

The $B \to \rho\gamma$ proceeds through the analogous $b \to d\gamma$ radiative transition. As such, its rate is suppressed by a factor of $|V_{td}/V_{ts}|^2 \sim \mathcal{O}(50)$ relative to $B \to K^*\gamma$ and remains unobserved. Current limits on the branching fractions of $B \to \rho\gamma$ are still an order of magnitude above the theoretical predictions. While the uncertainty in the theoretical predictions for the branching fraction of this mode are large, it may be possible to reduce these uncertainties by considering the ratio of the branching fractions for $B \to \rho\gamma$ and $B \to K^*\gamma$ which would lead to a measurement of $|V_{td}/V_{ts}|$. The analysis presented here represents a search with nearly an order of magnitude more data and new analysis techniques.

In a sample of 61.7×10^6 $B\overline{B}$ events, we find no significant evidence for the decay $B \to \rho\gamma$ is and establish the following 90% Confidence Level upper limits on the branching fraction:

$$\mathcal{B}[B^0 \to \rho^0\gamma] < 1.5 \times 10^{-6}$$
$$\mathcal{B}[B^+ \to \rho^+\gamma] < 2.8 \times 10^{-6}$$

Acknowledgments

It is rare to find discussion about graduate studies that is not marked with some degree of ambivalence and cynicism. One ponders lost opportunities, difficult colleagues, failed projects, stagnant social life and wonders whether it is worth all the time and effort.

I am happy to provide an exception. With a few brief paragraphs, I would like to thank the many people who have made my five years at Stanford a complete pleasure. While the ample supply of good weather, food and wine in the Bay Area certainly life better, it is certainly the people that have made my graduate school experience enjoyable and lots of fun.

My foremost debt is to Colin Jessop. Starting by convincing me to come to Stanford and work on *BABAR*, his advice and guidance was invaluable in finding interesting projects and making timely progress. This is easy to say, but even with the best intentions and careful thought, dispensing genuinely helpful advice and guidance is not easy. It is hard to imagine that anyone could have been a better advisor than Colin, and I hope that many more students will have the opportunity to work with him.

I would like to thank the members of Group C, my home at SLAC, for their support and help throughout my studies. In particular, I would like to thank our group leader Vera Lüth, who is responsible for making Group C a wonderful place to do research, as well as Helmut Marsiske, Urs Langenegger and Sven Menke. I also thank Aaron Roodman for his advice and guidance on many things.

In the final stages of the studies, the Reading Committee, (JoAnne Hewett, David Goldhaber-Gordon, David Leith, Vera Lüth, and Rafe Schindler), provided critical

guidance and support in writing this dissertation. I acknowledge a particular debt to David Leith, who patiently reviewed not only my dissertation, but the analysis documents and publications associated with the analyses.

It is with great pleasure that I thank the people who worked with me on these analyses, in particular Teela Pulliam and Tilmann Colberg on the $B \to K^*\gamma$ analysis, and Mark Convery on the $B \to \rho\gamma$ analysis. The open discussion and exchange of ideas that carried through our collaborative effort are what I enjoy most about research.

I must also thank the administrative staff both here at SLAC and at the Physics Department, in particular Anna Pacheco, Nuria Ayala, Lilian DePorcel, Marcia Keating and Kathleen Guan, who have rescued me on numerous occasions from bureaucratic oblivion.

Of course, graduate studies is not only about research: it is a way of life. I have been fortunate to have great friends who are true team players when it comes to endless procrastination, drinking a beer or several, and voyaging up and down the Peninsula on minutes notice. I thank Clarence Chang, Rhiju Das, Devarati Ghosh and Christopher Barnes for helping me live the graduate student experience to its fullest as we celebrated and laughed at life and, quite often, each other.

There are those who helped out far from the Stanford area. I would like to thank our neighbors on Long Island the Amorettys, the Kimuras, and the Niederers for their support and company when I visited home. Even from Boston, Carrie managed without a hitch cheer me and encourage me, despite her own work and studies. Her visits to Stanford were always something to look forward to.

It is impossible for me to express my debt to my sister and mother, who looked after me even as I nearly disappeared in my work, and as they took on their own careers as graduate students.

I regret that my father did not live to see where we are today. I would like to have shared with him these exciting five years.

Contents

Forward **v**

Acknowledgments **vii**

1 The Theory of Radiative B Decays **1**

1.1 Introduction 1

1.2 The Standard Model 1

1.2.1 Basic Principles 1

1.2.2 The Fundamental Constituents and their Interactions 3

1.2.3 The Weak Interaction 4

1.2.4 Flavor-Changing Interactions 6

1.3 Radiative Decays in the Standard Model 9

1.3.1 The Operator Product Expansion 11

1.3.2 Operators for $B \to \rho\gamma$ and $B \to K^*\gamma$ 12

1.3.3 Form Factors: Sum Rules and Lattice Calculations 14

1.3.4 Summary of Form Factor Calculations 17

1.3.5 Factorization 17

1.3.6 Direct CP Violation 18

1.4 Current Theoretical and Experimental Status 19

2 The *BABAR* Detector **21**

2.1 The $PEP-II$ Collider 21

2.2 The *BABAR* Detector 22

2.3 The Silicon Vertex Tracker (SVT) 23

2.3.1 SVT Layout . . . 24
2.3.2 SVT Electronics . . . 25
2.3.3 Reconstruction and Performance . . . 25
2.4 The Drift Chamber . . . 26
2.4.1 Design and Geometry . . . 26
2.4.2 Electronics and Readout . . . 28
2.4.3 Reconstruction . . . 28
2.4.4 Tracking . . . 28
2.5 The Ring-Imaging Cherenkov Detector (DIRC) . . . 29
2.5.1 Design and Geometry . . . 31
2.5.2 Electronics and Reconstruction . . . 31
2.6 The Electromagnetic Calorimeter . . . 32
2.6.1 Geometry . . . 33
2.6.2 Electronics . . . 33
2.6.3 Calibration and Monitoring . . . 34
2.6.4 Performance . . . 34
2.7 The Instrumented Flux Return . . . 35
2.7.1 The Resistive Plate Chambers . . . 35
2.7.2 Reconstruction . . . 36
2.8 Trigger . . . 36
2.8.1 The Level 1 Trigger . . . 37
2.8.2 The Level 3 Trigger . . . 38
2.9 The Data . . . 39

3 The Radiative Bhabha Calibration 40
3.1 Overview of the EMC Calibration . . . 40
3.1.1 Crystal Light Yield Calibration . . . 41
3.1.2 Leakage Corrections . . . 42
3.2 The Radiative Bhabha Calibration . . . 43
3.2.1 The Kinematic Fit . . . 43
3.2.2 Event Reconstruction and Photon Selection . . . 44

3.2.3 Determining the Correction 45
3.2.4 The Calibration 47
3.3 Performance 50

4 The $B \to K^*\gamma$ Analysis **51**
4.1 Global Event Selection 52
4.2 Photon Selection 54
4.2.1 Selection of Single Photon Candidates 54
4.2.2 π^0 and η Veto 55
4.3 K^* Reconstruction 56
4.3.1 Track reconstruction 56
4.3.2 Particle Identification 57
4.3.3 K^0_S Reconstruction 58
4.3.4 π^0 Reconstruction 59
4.3.5 Selection of K^* Candidates 60
4.4 Reconstruction of the B Candidate 60
4.5 Event Shape Criteria 62
4.5.1 $\cos\Theta^*_T$ 63
4.5.2 $\cos\Theta^*_B$ 65
4.5.3 $\cos\Theta_H$ 65
4.5.4 Event Shape selection 65
4.6 Efficiencies and Systematic Corrections 66
4.6.1 Photon and π^0 Efficiency Correction 66
4.6.2 Tracking Efficiency Correction 67
4.7 Signal Extraction 69
4.7.1 CP-Averaged Yield Extraction 70
4.7.2 Extraction of Conjugate Yields 72
4.8 Systematic Uncertainties 75
4.8.1 Photon Reconstruction 75
4.8.2 K^* Reconstruction 78
4.8.3 Systematics for A_{CP} Measurement 79

4.8.4 Signal Extraction 81
4.9 Cross checks 82
4.10 Averaged Results and Conclusions 83

5 The Search for $B \to \rho\gamma$ 86
5.1 Introduction 86
5.2 Event Reconstruction 88
5.3 Continuum Background Supression 90
5.3.1 Vertexing: Δz ($B^0 \to \rho^0\gamma$ only) 90
5.3.2 Tagside Flavor 93
5.3.3 Event Shape Variables 94
5.3.4 Neural Network 97
5.3.5 Background Suppression 101
5.3.6 Helicity Angle Cut 103
5.4 Signal Extraction 104
5.4.1 Event Rates 104
5.4.2 Signal Extraction Strategy 105
5.4.3 Validation of Signal Extraction Procedure 107
5.4.4 B decay backgrounds: 113
5.5 Systematic Studies of PDF Parameterzations: 114
5.5.1 Uncertainties from Fixed Parameters 116
5.5.2 Systematic Error on the Neural Network Selection 116
5.5.3 Consistency Check: $B \to K^*\gamma$ 118
5.5.4 Summary of Systematic Uncertainties 120
5.6 Results 121

6 Conclusions 125
6.1 Interpretation of Results 125
6.1.1 $B \to K^*\gamma$ Analysis 125
6.1.2 $B \to \rho\gamma$ Analysis 126
6.2 Future Prospects 127

Bibliography **130**

List of Tables

1.1 Results of form factor calculations 17

1.2 Theoretical predictions for $\mathcal{B}[B \to \rho\gamma]$ and $\mathcal{B}[B \to K^*\gamma]$ and current experimental results. 19

4.1 Expected number of $B \to K^*\gamma$ events in 22.7×10^6 $B\overline{B}$ decays 52

4.2 Signal and sideband regions for selected $B \to K^*\gamma$ candidates 63

4.3 Reconstruction efficiency for $B \to K^*\gamma$ from Monte Carlo simulation 68

4.4 Signal $m_{\rm ES}$ probability distributions. 71

4.5 Results of $B \to K^*\gamma$ signal extraction fit 72

4.6 The measured A_{CP} in signal and background samples. 74

4.7 Systematic uncertainties expressed as percent of $\mathcal{B}[B \to K^*\gamma]$ in each mode. 74

4.8 ARGUS ζ with and without kaon selection. 81

4.9 Branching fraction and A_{CP} measurements for individual final states. 84

4.10 Averaged results for $\mathcal{B}[B^0 \to K^{*0}\gamma]$, $\mathcal{B}[B^+ \to K^{*+}\gamma]$ and A_{CP} for all self tagging modes. 84

5.1 Current theoretical predictions and experimental limits for $B \to \rho\gamma$. . 88

5.2 Reconstruction efficiency for $B \to \rho\gamma$ from Monte Carlo simulation. . 105

5.3 Expected backgrounds artes for $B^0 \to \rho^0\gamma$ 106

5.4 Expected background rates in $B^+ \to \rho^+\gamma$ 106

5.5 Parameterizations used for $m_{\rm ES}$, ΔE^*, $M_{\pi\pi}$ signal extraction studies in the $B^0 \to \rho^0\gamma$ analysis. 108

5.6 Parameterizations used for $m_{\rm ES}$, ΔE^*, $M_{\pi\pi}$ signal extraction studies in the $B^+ \to \rho^+\gamma$ analysis. 108
5.7 Mean number of generated events, fitted yields and error from the toy Monte Carlo study 113
5.8 Signal distribution obtained from $B \to K^*\gamma$ control sample. 118
5.9 Efficiency for the neural network selection for the signal $B \to \rho\gamma$ Monte Carlo and $B \to D\pi$ control samples in Monte Carlo and data. 118
5.10 Results of signal extraction on the $B \to K^*\gamma$-enhanced sample 119
5.11 Summary of systematic errors for $B \to \rho\gamma$ 119
5.12 The fitted yields, biases from $B\overline{B}$ backgrounds, reconstruction efficiencies for $B^0 \to \rho^0\gamma$ and $B^+ \to \rho^+\gamma$. 120

6.1 Experimental results on $B \to K^*\gamma$ with theoretical predictions 126
6.2 Experimental results on $B \to \rho\gamma$ with theoretical predictions 126

List of Figures

1.1 The constituents of the Standard Model of Particle Interactions . . . 2
1.2 The Unitarity Triangle . . . 8
1.3 Effective flavor-changing neutral processes . . . 8
1.4 Primary operators for the $B \to \rho\gamma$ and $B \to K^*\gamma$ . . . 13

2.1 The *BABAR* detector . . . 24
2.2 The Silicon Vertex Detector (SVT) . . . 25
2.3 The Drift Chamber (DCH) . . . 27
2.4 The DIRC . . . 30
2.5 The Electromagnetic Calorimeter (EMC) . . . 33
2.6 The Instrumented Flux Return (IFR) . . . 35

3.1 The EMC source calibration . . . 42
3.2 E_{Fit}/E_{True} for Monte Carlo-simulated radiative Bhabha events. . . . 46
3.3 E_R/E_F peak positions versus Θ in three energy bins. . . . 48
3.4 Energy correction as a function of raw energy and Θ . . . 48
3.5 Mass spectrum of photon pairs . . . 49
3.6 Validation of calibration in π^0 and η decays . . . 49

4.1 Selection of $B\overline{B}$ events with a high-energy photon . . . 54
4.2 Lab frame kinematics of signal photon. . . . 55
4.3 Veto of photons from π^0 and η decays . . . 56
4.4 Charged kaon selection . . . 57
4.5 Reconstruction of $K^0_S \to \pi^+\pi^-$ decays . . . 59

4.6 Invariant mass distribution of photon pairs in hadronic events. . . . 60
4.7 Kinematic variables for the $B^0 \to K^{*0}\gamma$, $K^{*0} \to K^+\pi^-$ reconstruction: ΔE^* and $m_{\rm ES}$ 61
4.8 $m_{\rm ES}$ for the continuum background in off-resonance data 61
4.9 ΔE^* and $m_{\rm ES}$ distribution for signal and background processes 63
4.10 Event topology of signal and background processes 64
4.11 Event shape variables 66
4.12 Extended maximum likelihood fit for $B^0 \to K^{*0}\gamma$, $K^{*0}K^+\pi^-$ 69
4.13 Fitted $m_{\rm ES}$ distributions for $B \to K^*\gamma$ 70
4.14 Extraction of A_{CP} in $B^0 \to K^{*0}\gamma$, $K^{*0} \to K^+\pi^-$ 73
4.15 Systematic uncertainties in the ΔE^* selection 75
4.16 Systematic uncertainties in the ΔE^* selection 76
4.17 Systematic uncertainties of the π^0/η veto 76
4.18 Distance distributions from embedded photon events. 78
4.19 Systematic uncertainties of the A_{CP} measurement 79
4.20 ΔE^* and $M_{K^+\pi^-}$ for $B^0 \to K^{*0}\gamma$, $K^{*0} \to K^+\pi^-$ candidates 83

5.1 Reconstruction of $\rho^0 \to \pi^+\pi^-$ 88
5.2 Pion selection for $B \to \rho\gamma$ 90
5.3 $m_{\rm ES}$ and ΔE^* for $B \to \rho\gamma$ Monte Carlo simulation 91
5.4 $|\Delta z|$ distribution for signal and background in $B^0 \to \rho^0\gamma$ 92
5.5 Tag-side flavor production in $B \to \rho\gamma$ 95
5.6 E^*_{Ci} for $B^0 \to D^-\pi^+$ events 96
5.7 E^*_{Ci} for continuum events 96
5.8 Basic structure of a single hidden layer neural network. 98
5.9 Training of neural network for $B \to \rho\gamma$ 99
5.10 Output of $B^0 \to \rho^0\gamma$ neural network: Monte Carlo simulation 101
5.11 Output for $B^0 \to \rho^0\gamma$ neural network: control samples 101
5.12 Output for $B^+ \to \rho^+\gamma$ neural network: Monte Carlo simulation 102
5.13 Output for $B^+ \to \rho^+\gamma$ neural network: control samples 102
5.14 Optimization of the neural network selection 103

5.15 Helicity angle distribution for $B^+ \to \rho^+\gamma$ and $B^+ \to \rho^+\gamma$ 104
5.16 $m_{\rm ES}$, ΔE^*, $M_{\pi\pi}$ distributions for $B^0 \to \rho^0\gamma$ candidates in the off-resonance data. 109
5.17 $m_{\rm ES}$, ΔE^*, and $M_{\pi\pi}$ distributions for $B^+ \to \rho^+\gamma$ candidates in the off-resonance data. 109
5.18 ΔE^* vs. $m_{\rm ES}$ distributions for $B\overline{B}$ background in $B^0 \to \rho^0\gamma$ 110
5.19 ΔE^* vs. $m_{\rm ES}$ distributions for $B\overline{B}$ background in $B^+ \to \rho^+\gamma$ 110
5.20 $m_{\rm ES}$, ΔE^* and $M_{\pi\pi}$ projections for $B\overline{B}$ background in $B^0 \to \rho^0\gamma$ . . . 111
5.21 $m_{\rm ES}$, ΔE^* and $M_{\pi\pi}$ projections for $B\overline{B}$ background in $B^+ \to \rho^+\gamma$ . . 112
5.22 Fitted signal yields for $B^0 \to \rho^0\gamma$ with B decay backgrounds modeled using KEYS 114
5.23 Fitted signal yields for $B^0 \to \rho^0\gamma$ with B decay backgrounds modeled with parameterizations 114
5.24 Fitted signal yields for $B^+ \to \rho^+\gamma$ with B decay backgrounds modeled using KEYS 115
5.25 Fitted signal yields for $B^+ \to \rho^+\gamma$ with B decay backgrounds modeled with parameterizations 115
5.26 Fitted $m_{\rm ES}$ and ΔE^* distributions for $B^0 \to K^{*0}\gamma$ and $B^+ \to K^{*+}\gamma$ in on-resonance data 117
5.27 Parameterized distribution of $m_{\rm ES}$, ΔE^* and $M_{\pi\pi}$ for $B^0 \to K^{*0}\gamma$ and $B^+ \to K^{*+}\gamma$ Monte Carlo simulation 120
5.28 ΔE^* vs $m_{\rm ES}$, for $B \to K^*\gamma$-enhanced sample in the on-resonance data 121
5.29 Minimum of $-\log\mathcal{L}$ of the signal extraction fit in on-resonance data compared with Monte Carlo expectation 122
5.30 ΔE^* vs. $m_{\rm ES}$ distributions 122
5.31 Projections of fit results 123
5.32 Change in $-\log\mathcal{L}$ as a function of signal yield 123

6.1 Current experimental constraints on the CKM Unitarity Triangle [56]. 128

Chapter 1

The Theory of Radiative B Decays

1.1 Introduction

The decays $B \to \rho\gamma$ and $B \to K^*\gamma$ are effective flavor-changing neutral current interactions. In this chapter, we discuss how these processes arise in the Standard Model of particle interactions and why they are of interest, particularly in extracting the ratio of the Cabibbo-Kobayashi-Maskawa matrix elements $|V_{td}/V_{ts}|$. We investigate how the theory allows the rate of these decays to be predicted using techniques such as the Operator Product Expansion and Factorization. The decays $B \to \rho\gamma$ and $B \to K^*\gamma$ are also probes of new physics processes outside of the Standard Model. We discuss possible signatures of such new phenomena in these decays. Finally, we summarize the current status of experimental results and theoretical calculations.

1.2 The Standard Model

1.2.1 Basic Principles

The Standard Model endeavors to explain phenomena within the realm of elementary particles and their interactions. It has thus far explained all experimental results, with exception of the generation of neutrino masses and the unobserved Higgs boson. The Standard Model is built upon a foundation of relativistic *quantum field theory*,

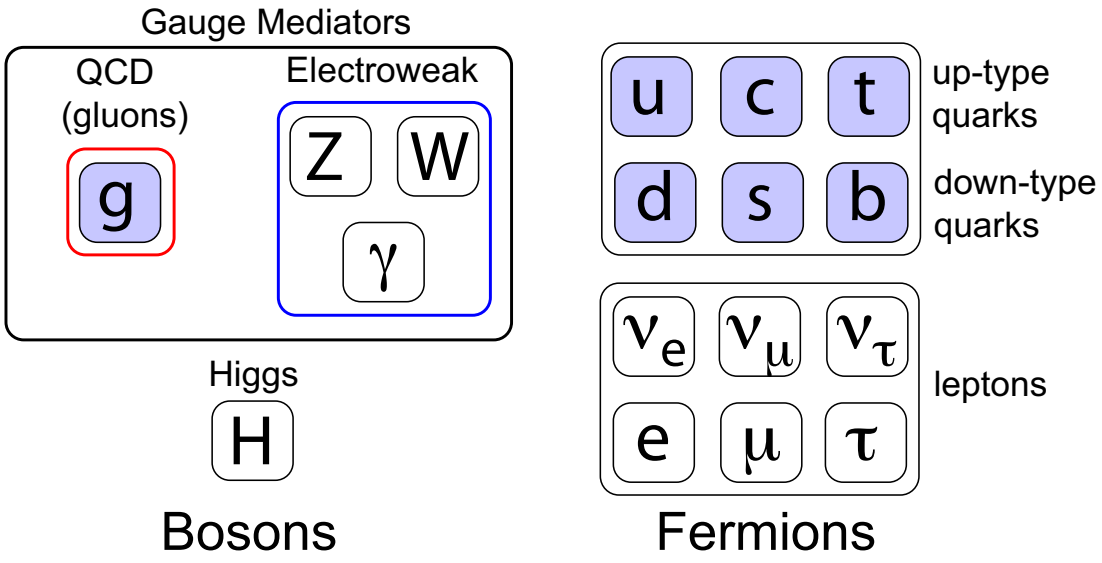

Figure 1.1: The constituents of the Standard Model of Particle Interactions

which embeds the dynamical framework of quantum mechanics within the space-time structure of special relativity [1]. To this, we add the principle of *local gauge invariance* [2], which postulates that the theory is invariant under transformations of the fields of the form:

$$\psi(x_\mu) \rightarrow e^{i\alpha_a(x_\mu)T_a}\psi(x_\mu), \tag{1.1}$$

where the T_a are the generators of a Lie group and $\alpha_a(x)$ are a set of arbitrary real functions of the space-time coordinate x_μ, one for each generator. Local gauge invariance within a quantum field theory forces the introduction of a set of spin-1 bosons which mediate interactions between the fields characterized by a universal coupling constant and conserved charge. Quantum electrodynamics can be expressed as a quantum field theory with gauge invariance under the group $U(1)$. The Standard Model involves more complicated groups which endow it with a richer structure. Finally, we will need the mechanism of *spontaneous symmetry breaking* [3] to generate the observed masses of the particles. We will find that effective flavor-changing neutral current processes, otherwise forbidden, are enabled as a consequence.

1.2.2 The Fundamental Constituents and their Interactions

The Standard Model of particle interactions is illustrated in Figure 1.1 as a survey of the elementary particles. The first division among these particles occurs between *bosons* carrying integer spin and *fermions* carrying half-integer spin. Each particle has a corresponding antiparticle which carries the opposite quantum numbers. In some cases, as in the photon and the Z, the particle is its own antiparticle.

The spin-1 bosons are responsible for the electroweak and the strong interactions, which are described by quantum chromodynamics (QCD). We set aside the spin-0 Higgs field for later discussion. The bosons arise from the local gauge invariance of the quantum field theory: in order to preserve the local gauge invariance of the kinetic term, it is necessary to introduce *gauge fields* A^a_μ by modifying the derivative term ∂_μ into the *covariant derivative* D_μ:

$$\partial_\mu \Rightarrow D_\mu = \partial_\mu + igT^a A^a_\mu \tag{1.2}$$

where the A^a_μ transform as:

$$A^a_\mu \rightarrow A^a_\mu - \frac{1}{g}\partial_\mu \alpha_a(x_\mu) \tag{1.3}$$

The T_a are the generators of the chosen Lie algebra, $SU(3)$ [4] in the case of QCD and $SU(2)_L \times U(1)_Y$ [5] for the electroweak interactions. The A^a_μ are the particles mediating the elementary interactions in the Standard Model. Local gauge and Lorentz invariance dictate that they are Spin-1 Lorentz vectors transforming under the adjoint representation of the group. The factor g is the universal coupling constant for the gauge group determining the strength of the interaction, with the covariant derivative constructed in such a way that the transformations of the gauge field cancel terms arising from the derivative of the gauge-transformed field.

The eight gauge bosons mediating chromodynamics are called gluons, while the four gauge bosons of the electroweak interactions after spontaneous symmetry breaking (described in Section 1.2.3) are the W, the Z, and the photon γ.

The representation of the T_a matrices within the covariant derivative for the fermions determines their group transformation and gauge interaction properties. If the T_a

are a non-trivial representation of the group, the fermions couple with the corresponding gauge bosons via terms in the covariant derivative. Otherwise, they are singlets under the gauge group and do not interact through this interaction.
In this way, the fermions are divided into two categories:

- Six *quarks*, which transform under the fundamental representation of chromodynamic $SU(3)$, are said to carry color (chromodynamic charge) and hence participate in QCD.
- Six *leptons*, which are $SU(3)$ singlets, carry no color and do not interact via QCD.

The six quarks are classified into "up"-type quarks with electric charge +2/3 and "down"-type quarks with electric charge -1/3. Horizontally, they are divided into three generations. Pairs of left-handed up and down-type quarks in each generation are doublets of the $SU(2)_L$ gauge group of the electroweak interaction. The interaction projects out the left-handed component of the fermion field, resulting in parity violation. The right-handed components are singlets of $SU(2)_L$. The anti-fermions appear as conjugate terms in the Lagrangian, with the right-handed fermions forming doublets and left-handed fermions forming singlets.
The leptons are likewise divided horizontally into generations and vertically into a $SU(2)_L$ doublet consisting of a neutrino, carrying no electric charge, and a charged lepton with electric charge -1. The various types of quarks and leptons (e.g. up, strange, μ, τ) are collectively called *flavors*.

1.2.3 The Weak Interaction

Spontaneous Symmetry Breaking

The manifestation of the mediators of the electromagnetic and weak interactions in the form of the massless photon and the massive W and Z is the result of the *spontaneous symmetry breaking* of the $SU(2)_L \times U(1)_Y$ gauge symmetry. Spontaneous symmetry breaking allows the creation of massive gauge bosons without spoiling the gauge symmetry which would otherwise result if explicit mass terms were inserted

directly into the Lagrangian for the W and Z.

At the heart of the symmetry breaking is the introduction of the Higgs scalar field. While any number of gauge invariant configurations that are non-trivial representations of $SU(2)_L$ can break the symmetry, the simplest is a single $SU(2)_L$ doublet:

$$\phi = \begin{pmatrix} \phi^+ \\ \phi^0 \end{pmatrix} \tag{1.4}$$

We assume that the Higgs field carries no color.

In order to preserve the gauge symmetry, the kinetic term of the Higgs field must enter via the gauge-covariant derivative:

$$\mathcal{L} = \left| \left(\partial_\mu + igT^i \cdot W^i_\mu + ig' \frac{Y}{2} B_\mu \right) \phi \right|^2 - V(\phi) \tag{1.5}$$

Here, the W^i_μ triplet and B_μ gauge bosons are introduced via gauge symmetry under the $SU(2)_L$ and $U(1)_Y$ groups, respectively. The Higgs potential $V(\phi)$ is such that its minima are at non-zero values of the Higgs field. The Higgs field then has a non-zero vacuum expectation value v and the $SU(2)_L \times U(1)_Y$ gauge fields acquire a mass from terms quadratic in the Higgs field. In order to identify the physical manifestation of these fields, we identify the mass eigenstates. The combination $W^\pm_\mu = W^1_\mu \pm iW^2_\mu$ is diagonal with mass $\frac{1}{2}vg$. The other two fields are off-diagonal in the mass matrix; after diagonalizing the mass matrix, the eigenstates are:

$$A_\mu = \frac{g'W^3_\mu + gB_\mu}{\sqrt{g^2+g'^2}} \qquad Z_\mu = \frac{gW^3_\mu - g'B_\mu}{\sqrt{g^2+g'^2}} \tag{1.6}$$

with eigenvalues:

$$M_A = 0 \qquad M_Z = \tfrac{1}{2}v\sqrt{g^2+g'^2} \tag{1.7}$$

In the aftermath, we identify the massless gauge field from the remaining $U(1)$ symmetry with the photon and the three massive bosons with the weak interaction. Fermion masses are likewise generated from the vacuum expectation value of the Higgs field via Yukawa terms:

$$-M[\overline{\chi}_L\,\phi\,\chi_R + \overline{\chi}_R\,\phi^\dagger\,\chi_L] \tag{1.8}$$

where M is arbitrarily chosen to construct the observed mass of the fermion. The Standard Model makes no predictions for these fermion masses; they are inputs parameters to the theory that must be determined from experiment.
The mechanism of spontaneous symmetry breaking thus generates all boson and fermion masses in the Standard Model. Since we defined the Higgs field as a $SU(3)$ singlet, the $SU(3)$ symmetry of QCD is not broken, leaving the gluons massless.

1.2.4 Flavor-Changing Interactions

The Weak Charged Current

The W boson can mediate flavor-changing charged current interactions in the quark sector arising from the terms:

$$-i\frac{g}{\sqrt{2}}\,\overline{d}\gamma^\mu\frac{1-\gamma^5}{2}u\,W^-_\mu \;+\; \text{Hermitean Conjugate.} \tag{1.9}$$

where d is a down-type quark and u is an up-type quark. However, the mass eigenstates of the six quarks do not correspond to the flavor eigenstates, but are mixed in a unitary transformation of the three down-type quarks. The transformation is described by a unitary 3×3 matrix V, known as the Cabibbo-Kobayashi-Maskawa (CKM) matrix [6]. The charged current interactions between the three up-type quarks and the three down-type quarks can be summarized as:

$$(\overline{u},\ \overline{c},\ \overline{t})\,\frac{\gamma^\mu(1-\gamma^5)}{2}\begin{pmatrix} V_{ud} & V_{us} & V_{ub}\\ V_{cd} & V_{cs} & V_{cb}\\ V_{td} & V_{ts} & V_{tb}\end{pmatrix}\begin{pmatrix} d\\ s\\ b\end{pmatrix}W^-_\mu \;+\; \text{H.C.} \tag{1.10}$$

where we have spelled out the CKM matrix explicitly. Unitarity and phase rotations of the quark wavefunctions allow the nine elements of the matrix to be expressed in terms of three angles and one phase. Kobayashi and Maskawa proposed that this phase was the origin of CP Violation and argued that at least three generations of

quarks must exist in order for unitarity to permit a non-trivial phase. This prediction was made at a when time only three quarks were known to exist.

While the weak interactions are characterized by a universal coupling constant resulting from the $SU(2)_L \times U(1)_Y$ symmetry, the intergenerational quark interactions are scaled by the appropriate CKM matrix elements; certain transitions have greater rates due to favorable CKM elements, while others are suppressed. The theory makes no predictions for the values of these elements aside from unitarity; they are yet another set of arbitrary parameters which must be obtained from experiment. Since the individual elements of the CKM matrix can be measured independently without invoking the theoretical requirement of unitarity, the requirement of unitarity can be used to overconstrain the CKM matrix and test the Standard Model of weak interactions.

The unitarity of the CKM matrix is conveniently summarized in *unitarity triangles*. In particular, unitarity imposes the following constraint on elements of the first and third column of the CKM matrix:

$$V_{ud}^* V_{ub} + V_{cd}^* V_{cs} + V_{td}^* V_{tb} = 0 \tag{1.11}$$

This is expressed graphically in the complex plane as a triangle in Figure 1.2, where the sides of the triangle have been normalized and rotated by dividing by the second term in Equation 1.11, which consists of relatively well known elements of the CKM matrix. The sides of the triangle, which correspond to magnitudes of CKM elements, can be measured by analyzing the rates of processes which involve these CKM elements, while the angles, which correspond to the relative phases between the elements, can be measured by CP-violating asymmetries.

GIM Mechanism

The coupling of the quarks to the neutral Z boson are flavor-diagonal by definition, with the result that there are no tree-level *flavor-changing neutral currents* in the Standard Model. Such processes can only proceed at higher orders in loop processes such as the "penguin" and "box" diagrams shown in Figure 1.3. These processes

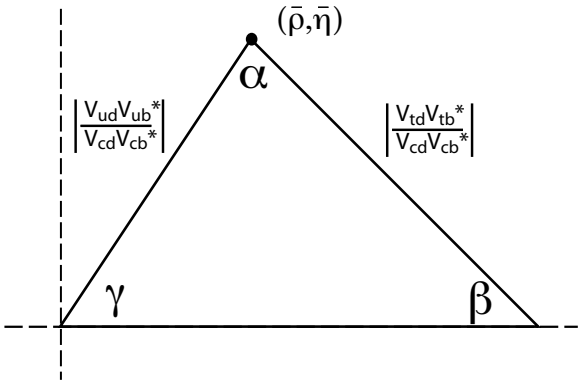

Figure 1.2: Unitarity triangle summarizing the orthogonality of the first and third columns of the CKM matrix.

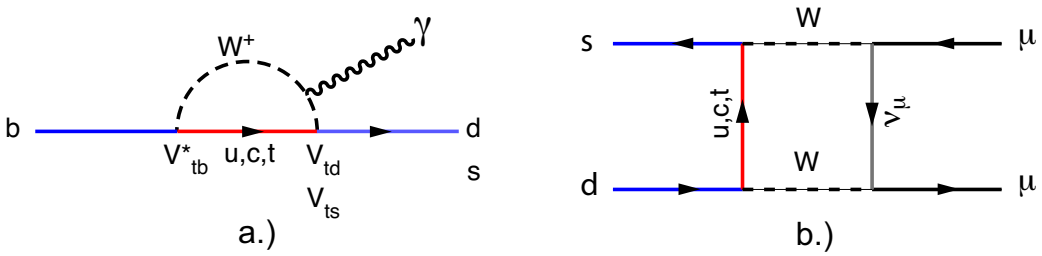

Figure 1.3: Effective flavor-changing neutral current processes a.) The $b \to d/s\gamma$ penguin diagram. b.) The $K^0 \to \mu^+\mu^-$ box diagram.

are collectively known as *effective flavor-changing neutral currents*. Unitarity of the CKM matrix has profound consequences for effective flavor-changing neutral currents. In the limit of degenerate quark masses, they are forbidden: unitarity of the CKM matrix demands that the separate contributions from the quarks that mediate the loop cancel each other in sum [7]. As an example, the $b \to s\gamma$ penguin transition in Figure 1.3 contains contributions from the three up-type quarks that mediate the loop scaled by the appropriate CKM matrix elements:

$$V_{tb}^* V_{ts} + V_{cb}^* V_{cs} + V_{ub}^* V_{us} \tag{1.12}$$

This quantity is identically zero from the unitarity relations between the second and third columns of the CKM matrix. The different quark masses break the degeneracy and allow these processes to occur at suppressed rates. Historically, Glashow, Iliopolous and Maiani proposed the existence of the charm quark at a time when only three quarks were thought to exist to explain the highly suppressed rate of $K_L^0 \to \mu^+\mu^-$, which could only proceed through diagrams like the box diagram in Figure 1.3. In the GIM mechanism, the contribution of the charm quark in the loop would cancel the contribution of the up quark in the diagram through orthogonality of the 2×2 matrix (corresponding to unitarity of the CKM matrix). The GIM mechanism also explained the absence of flavor-changing Z interactions which would occur if the strange quark were not part of a weak $SU(2)_L$ doublet [8].
The spontaneous symmetry breaking process, which endows the quarks with differing masses, is thus responsible for breaking the GIM mechanism in loop processes by disturbing the balance imposed by the unitarity of the CKM matrix, which would otherwise forbid effective flavor-changing neutral currents processes.

1.3 Radiative Decays in the Standard Model

Effective flavor-changing neutral current processes proceed through virtual loops and thereby offer a testing ground of physics at high mass scales. We find a peculiar situation where the enormous mass of the top quark relative to the other quarks weakens the GIM suppression and enhances its contribution in these processes. If the CKM matrix elements of the up and charm contributions are known, we can isolate the top contribution to such processes, allowing the extraction of the corresponding CKM matrix elements involving the top quark. The weak interaction properties of the top quark, with mass $\sim 174\,\mathrm{GeV}/c^2$, are thus accessible at much lower energy through these processes.
In addition, these processes are sensitive to any other flavor-changing particles not present in the Standard Model that may mediate the loop. These contributions can affect the rate of the process and induce CP violation. In this way, flavor-changing neutral currents are also sensitive to physics beyond the Standard Model. In all

cases, the usefulness of any given process is contingent on the ability to make reliable theoretical predictions of its rate and CP violation.

The radiative decays $B \to \rho\gamma$ and $B \to K^*\gamma$ are examples of effective flavor changing neutral current interactions which offer an opportunity to study the top quark and potential non-Standard Model contributions. The principle aim of the studying these decays is to probe the CKM matrix elements V_{td} and V_{ts} through the underlying $b \to d\gamma$ and $b \to s\gamma$ transitions shown in the first diagram of Figure 1.3. This goal is greatly complicated by the need to properly account for the QCD effects. The most notable difficulty arises from the evolution of the QCD coupling from small values at scales much larger than $\Lambda_{QCD} \sim 250\,\mathrm{MeV}$, where perturbative calculations are possible, to large values at scales $\sim \Lambda_{QCD}$, where they break down [9].

The large QCD couplings at low energies have profound consequences for the phenomenology of quarks. The strength of the coupling results in *confinement*: colored objects, such as quarks, can only appear in colorless combinations. The two possible configurations for quarks are antisymmetric color triplets corresponding to baryons, such as the familiar proton and neutron, and quark-antiquark pairs resulting in mesons such as the pion, the kaon, and the B meson. The upshot is that quarks can only be studied experimentally within the confines of baryons and mesons, with the exception of the top quark, which decays before forming a bound state via QCD. In order to make connection between our experimental observations and the CKM parameters, we must be able calculate the effects of confinement. Thus, while we are interested in parameters which are fundamental to the weak interaction, we must inevitably confront QCD.

The challenge posed by this dramatic evolution of the behavior of the QCD is tackled by dividing the problem into several parts. The Operator Product Expansion provides a framework in which to separate contributions of high-mass physics, occurring at scales larger than the B meson mass, where perturbative QCD calculations are reliable, from the contributions from lower mass scales, where they start to break down. Theoretical estimates of the effects from below this scale, called "long distance" contributions, come from non-perturbative techniques such as QCD sum rules or lattice calculations. Heavy Quark Effective Theory then provides the interface between the

long-distance contributions and the perturbative calculations.

1.3.1 The Operator Product Expansion

The Operator Product Expansion [10] expresses the full diagrammatic theory as an effective Hamilitonian constructed from a set of local operators O_i, where the amplitude for a given process $I \to F$ is expressed as a sum of matrix elements of the local operators:

$$\langle F|\mathcal{H}_{Eff}|I\rangle = \frac{G_F}{\sqrt{2}} \sum_i V_i C_i(\mu) \langle F|O_i(\mu)|I\rangle \tag{1.13}$$

Here, G_F is the Fermi constant, characterizing the strength of the underlying weak processes. The V_i are CKM matrix elements appropriate for the quark transitions and the O_i are the local operators categorized by Dirac and color structure forming a complete set for a given transition. The *Wilson coefficients* C_i serve are the numerical coefficients associated with these effective interactions. The amplitude of the effective Hamiltonian is thus expressed as a sum of local operator amplitudes and their Wilson coefficients.

The division of mass scales is implied by the μ-dependence of the Wilson coefficients and the operators. The Wilson coefficients summarize the effects of interactions at scales higher than μ, while the operators absorb all the effects that occur at scales below μ. The choice of μ is arbitrary, but is typically chosen to be $\mathcal{O}(m_b)$ for the study of B decays, which is fortunately well above the scale Λ_{QCD} where perturbative QCD starts to break down. The operator product expansion offers a useful way to summarize the expected effects of new physics contributions from scales higher than μ: since we integrate over these new degrees of freedom, they simply result in a modification of the Wilson coefficients in the Standard Model or additional Wilson coefficients associated with new operators that may be introduced with the new physics.

In principle, the choice of μ should have no impact on the physical results of the calculation. It represents an arbitrary border line between physics occurring at "higher" and "lower" scales. As a result, the μ-dependence of the Wilson coefficients and the

operator matrix elements must cancel. In practice, however, the Wilson coefficients contain explicit dependence on μ due to the truncation of the perturbation expansion; a full calculation to all orders would eliminate this dependence.

Determining the Wilson Coefficients

The Wilson coefficients are calculated by matching the predictions of the effective theory with the full theory with all degrees of freedom at a high mass scale, typically M_W, where the relevant diagrams and their QCD corrections can be calculated via perturbation theory and evolved down to the relevant energy scale (in this case the b quark mass) via renormalization group equations. After renormalization, the operators can be identified within the full calculation and the Wilson coefficients extracted. The QCD corrections result in two interesting effects. First, the QCD contributions can introduce contributions from other operators, resulting in operator mixing. Operator mixing can significantly affect the decay rate: in $b \to s\gamma$, this results in a three-fold enhancement [11]. Second, the resulting expressions for the Wilson coefficients contain an expansion in $\alpha_s \ln \frac{M_W^2}{\mu^2}$. Since μ is typically chosen to be smaller than M_W, the expansion diverges. Solving the renormalization group equation allows us to sum these logarithm terms by determining the evolution of the Wilson coefficients as a function of μ in a manner completely analogous to determining the evolution of a gauge coupling.

1.3.2 Operators for $B \to \rho\gamma$ and $B \to K^*\gamma$

The largest contributions for the radiative decays $B \to \rho\gamma$ and $B \to K^*\gamma$ arise from the four-quark operators O_1 and O_2, and the electromagnetic penguin operator O_7. Also relevant is the chromomagnetic penguin operator O_8, particularly for CP violation studies. The operators have the following form:

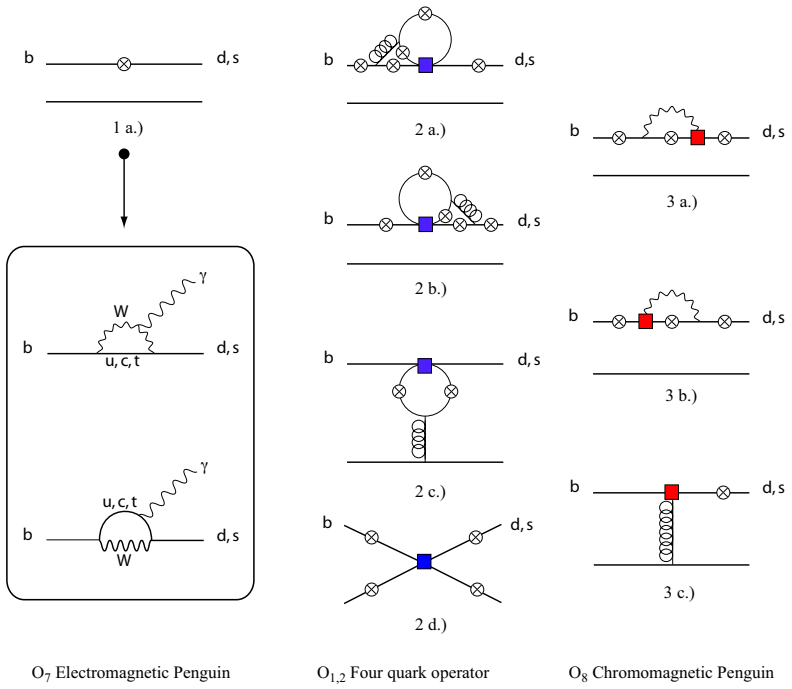

Figure 1.4: Primary operators for the $B \to \rho\gamma$ and $B \to K^*\gamma$ processes, up to $\mathcal{O}(\alpha_s)$. On the left, the operator O_7 is expressed in diagrammatic form. The crossed circles represent possible insertions of the radiated photon.

$$O_1 = \overline{q}_\alpha(1-\gamma^5)p_\alpha\,\overline{p}_\beta(1-\gamma^5)b_\beta \qquad O_2 = \overline{q}_\alpha(1-\gamma^5)p_\beta\,\overline{p}_\alpha(1-\gamma^5)b$$

$$O_7 = \tfrac{e}{8\pi^2}\,m_b\,\overline{q}_\alpha\sigma^{\mu\nu}(1+\gamma^5)b_\alpha\,F_{\mu\nu} \qquad O_8 = \tfrac{g}{8\pi^2}\,m_b\,\overline{q}_\alpha\sigma^{\mu\nu}(1+\gamma^5)T^a_{\alpha\beta}b_\beta\,G^a_{\mu\nu} \tag{1.14}$$

We follow the convention used by Bosch and Buchalla for the numbering of the operators [22]. α and β are color indices, q refers to $d(s)$ for $B \to \rho\gamma(B \to K^*\gamma)$, and p can be either u or c. The effective Hamilitonian for the process can be written explicitly as:

$$\mathcal{H}_{Eff} = \frac{G_F}{\sqrt{2}}\sum_{p=u,c} V^*_{pq}V_{pb}\;[C_1O_1^p + C_2O_2^p + C_7O_7 + C_8O_8] \tag{1.15}$$

At one-loop order, the decay is mediated entirely by the O_7 electromagnetic penguin operator without mixing with the four-quark operators; mixing between these sets of operators only occurs at the two-loop level at $\mathcal{O}(eg^2)$ and $\mathcal{O}(g^3)$. The rate of the *inclusive* $b \to s\gamma$ transition can then be written at one-loop order as:

$$\Gamma[b \to s\gamma] = \frac{\alpha G_F^2 m_b^5}{128\pi^4} \left| \sum_{p=u,c} V_{ps}^* V_{pb}\, C_7(m_b) \right|^2 . \tag{1.16}$$

The extraction of the rates to exclusive final states (*e.g.* K^*) require matrix elements from non-perturbative calculations, as described below. Several groups have completed the next-to-leading order evaluation of the Wilson Coefficients at three-loop level [12].

1.3.3 Form Factors: Sum Rules and Lattice Calculations

With the Wilson coefficients in hand, we turn to the task of calculating the operator matrix elements. For the decays $B \to V\gamma$, where V is a vector meson, we parameterize the matrix element with a form factor:

$$\langle V(\lambda, p_V)|\overline{f}\, \sigma_{\mu\nu} q^\nu b|B\rangle = 2i\varepsilon_{\mu\nu\rho\sigma}\epsilon(\lambda)^{*\nu} p_B^\rho p_V^\sigma F_1^{B\to V}(q^2) \tag{1.17}$$

where $\epsilon(\lambda)$ is the polarization vector, B is the parent B meson, and p_B, p_V and $q = p_B - p_V$ are the momenta of the B meson, the outgoing vector meson, and photon respectively. Form factors, which summarize the non-perturbative effects of QCD interactions, have been calculated in two approaches: *sum rules* and *lattice calculations*.

Sum Rules

The *QCD sum rule* [14] approach relates the vacuum-to-vacuum correlation function to a dispersion integral via analytic continuation:

$$\Pi(Q^2 = -q^2) = i \int d^4y e^{iq\cdot y} \langle \text{vac}|T\left[J(y)J(0)\right]|\text{vac}\rangle = \frac{1}{\pi}\int_{s_0}^{\infty} ds \frac{\rho(s)}{s+Q^2} + \text{subtractions} \tag{1.18}$$

The currents J are composed of the quarks in the Dirac structure we are interested in. The first integral is the Fourier transform of the non-perturbative transition from the initial state hadronic state (*i.e.* the B meson) at $x = 0$ to the final hadronic state at $x = y$. In the second integral, the information about the hadronic states is contained in the *spectral function* $\rho(s) = \text{Im}\Pi(s)$, with s ranging from the threshold s_0 and extending to infinity. The spectral function consists of δ functions and Breit-Wigner distributions representing the hadronic states we are interested in, and a continuum contribution.

$$\rho(s) = \rho_H(s) + \Theta(s - s_a)\rho(s)_{AF} \tag{1.19}$$

Here $\Theta(x)$ is the Heavyside-Lorentz function and s_a is the threshold for the onset of asymptotic freedom.

With the help of the operator product expansion, $\Pi(Q^2)$ is calculated at large Q^2 well above Λ^2_{QCD}. The expansion, as described above, separates the short distance contributions into Wilson coefficients obtained from perturbative calculations and matrix elements of vacuum matrix called *vacuum condensates*:

$$\Pi_{QCD}(Q^2) = \sum_k C_{2k}(Q^2, \alpha_s, \mu)\frac{1}{(Q^2)^k}\langle \text{vac}|O_{2k}(\mu)|\text{vac}\rangle \tag{1.20}$$

The vacuum condensates are universal quantities and can be obtained experimentally from processes where the spectral function is well known and transferred to the calculation of other processes.

The primary assumption of the QCD sum rule approach is *quark-hadron duality* which states that $\Pi(Q^2) = \Pi(Q^2)_{QCD}$, allowing the dispersion integral to be expressed in terms of QCD parameters such as α_s and quark masses.

The *light cone QCD sum rule* [15] approach is a variant of the sum rule approach in which the hadrons are represented as external states in the correlation function. For

$B \to V\gamma$, the correlation function takes the form [17]:

$$i\varepsilon_{\mu\nu\rho\sigma}\,\epsilon(\lambda)^{*\nu} q^\rho p^\sigma T\left((p+q)^2\right) = i\int dx\; e^{iq\cdot x}\;\langle\, V(p,\lambda)\,|\,T[\,\overline{f}\,\sigma_{\mu\nu}q^\nu b(x)\,\overline{b}(0)i\gamma_5 f(0)\,]\,|\,\mathrm{vac}\rangle \tag{1.21}$$

The contribution of the B meson in the function $T(p+q)^2$ can be identified as a pole function in the dispersion integral, which gives us the relation of the correlation function to the form factor [18]. The matrix element is expanded in the operator product expansion with the light cone wavefunctions of the hadron ordered in increasing *twist*, defined as $d - s$, where d and s are the dimension and spin of the operator, respectively. Quark-hadron duality then relates the twist expansion to the desired form factor.

Lattice Calculations

Lattice QCD calculations [16] involve simulating the quantum field theory on a discrete mesh of space-time points. Two parameters govern the reliability of the calculations: the size of the simulated lattice, which must be at least the size of the particle being simulated ($\gg 1\,\mathrm{fm}$), and the lattice spacing, which must be small enough to make the effects of the discretization small ($\ll 1/\Lambda_{QCD}$). The heavy mass of the b quark, which requires small lattice spacings due to its small Compton wavelength, introduces another complication. When the spacing is not small enough, the b quark cannot be simulated directly; it is simulated at lower masses and the results extrapolated to the b quark mass.

The fast emission of the meson in the two body decay at $q^2 = 0$ relevant for $B \to \rho\gamma$ and $B \to K^*\gamma$ likewise cannot be directly simulated on the lattice [18]. While the lattice calculations are limited in their ability to directly calculate the form factors in the kinematic range we are interested in, they nonetheless provide important cross-checks on the sum rule techniques.

	LCSR [18]	LCSR [17]	lattice+LCSR [19]	QCD SR [20]
$F_1^\rho(0)$	0.29 ± 0.04	0.24 ± 0.07		
$F_1^{K^*}(0)$	0.38 ± 0.06	0.32 ± 0.05	$0.32^{+0.04}_{-0.02}$	0.38 ± 0.06
ζ	0.77 ± 0.08	0.76 ± 0.06		

Table 1.1: Results of form factor calculations using light cone sum rule (LCSR), lattice and QCD sum rules (QCDSR).

1.3.4 Summary of Form Factor Calculations

A summary of the relevant form factors $F_1^\rho(0)$, $F_1^{K^*}(0)$ and the ratio of form factors $\zeta = F_1^\rho(0)/F_1^{K^*}(0)$ calculated with the various methods is shown in Table 1.1.

1.3.5 Factorization

The theoretical calculation of the rates of $B \to \rho\gamma$ and $B \to K^*\gamma$ is completed by incorporating the form factors into the operator matrix elements. The situation is complicated by contributions from purely hadronic operators in which the radiated photon results from electromagnetic corrections. It is necessary to separate these processes, which involve hard gluon exchange and can be calculated perturbatively, from the non-perturbative form factors. To this end, *heavy quark effective theory* [21] is employed to simplify the QCD dynamics which occur within the B meson.
The central assumption of heavy quark effective theory is that within the B meson, the b quark interacts with the light degrees of freedom, consisting of gluons, quarks and anti-quarks, through the exchange of soft gluons with momentum transfer $\mathcal{O}(\Lambda_{QCD})$. Heavy quark effective theory is derived in the limit $m_b \gg \Lambda_{QCD}$ where these interactions effect no change in the four-velocity of the b quark, with corrections in powers of Λ_{QCD}/m_b. This allows the factorization of the hard gluon exchange contributions from the form factor in the form [22][23]:

$$\langle V\gamma(\epsilon)|O_i|\overline{B}\rangle = F_1^{B\to V}(0)T_i^I + \left[\int_0^1 d\xi\, dv T_i^{II}(\xi, v)\Phi_B(\xi)\Phi_V(v)\right]\cdot\epsilon \qquad (1.22)$$

The *hard-scattering kernels* T_i^I and T_i^{II} represent contributions from the perturbative hard-gluon exchange, categorized according to whether the exchange occurs along the $b \to d/s$ quark line (T_i^I), or with the spectator quark (T_i^{II}). The diagrams contributing to the hard scattering kernels at $\mathcal{O}(\alpha_s)$ are shown in Figure 1.4. Diagrams 2a and 2b, from $O_{1,2}$ and diagrams 3a and 3b from O_8 contribute to T_i^I. Diagrams 2c and 3c contribute to T_i^{II}.

1.3.6 Direct CP Violation

Direct CP violation in the decays $B \to K^*\gamma$ and $B \to \rho\gamma$ results in different decay rates for the charge-conjugate processes. The magnitude of direct CP violation is characterized by comparing the difference to the CP averaged rate:

$$A_{CP} = \frac{\Gamma[\overline{B} \to \overline{V}\gamma] - \Gamma[B \to V\gamma]}{\Gamma[\overline{B} \to \overline{V}\gamma] + \Gamma[B \to V\gamma]} \tag{1.23}$$

where $V = \rho,\ K^*$. While the Standard Model predicts larger direct CP violation in $B \to \rho\gamma$, the theoretical status is rather uncertain [24]. Since the analysis presented here is unlikely to be sensitive to this, we confine our discussion to $B \to K^*\gamma$.

Direct CP violation results from the interference of amplitude contributions with different strong and weak (CP even and odd) phases. For the $b \to s\gamma$ process, the weak phases come from the the relevant CKM matrix elements in the Standard Model and new physics contributions which can provide non-trivial phases to the Wilson coefficients. The imaginary parts of the operator matrix elements from $\mathcal{O}(\alpha_s)$ loops involving light and charm quarks and gluons produce strong phases [25].

Two features of the Standard Model suppress CP violation in the $b \to s\gamma$ transition. First, the interference resulting from any non-trivial CKM phase is modulated by the magnitude of the CKM matrix elements involved. Since the up and charm contributions are small relative to the top contributions, this interference is suppressed by the magnitude of the CKM elements. Second, the generation of the non-trivial strong phases occurs at $\mathcal{O}(\alpha_s(m_b)) \approx 0.214$. As a result, A_{CP} in $b \to s\gamma$ is expected to be less than 1% in the Standard Model [26].

New physics contributions can significantly enhance A_{CP} by introducing weak phases in the Wilson coefficients. In particular, the $O_7 - O_8$ interference can generate significant direct CP violation in supersymmetric theories with light gluinos ($m_{\tilde{g}} \tilde{<} m_{\tilde{q}}$) which also significantly enhance the magnitude of O_8. In such cases $A_{CP} \sim 20\%$ is possible. Due to the unambiguous expectation for small A_{CP} in $B \to K^*\gamma$, any observation of large A_{CP} would be an indication of new physics.

Authors	$\mathcal{B}[B^0 \to K^{*0}\gamma]/10^{-5}$	$\mathcal{B}[B^+ \to K^{*+}\gamma]/10^{-5}$
Bosch and Buchalla [22]	7.1 ± 2.5	7.45 ± 2.5
Beneke *et al.* [23]	$7.9^{+3.5}_{-3.0}$	$7.9^{+3.5}_{-3.0}$
Ali and Parkhamenko [24]	7.2 ± 2.7	7.2 ± 2.7
CLEO [31]	$4.55 \pm 0.70 \pm 0.34$	$3.76 \pm 0.86 \pm 0.28$
BELLE [33]	$4.96 \pm 0.67 \pm 0.45$	$3.89 \pm 0.93 \pm 0.41$

Authors	$\mathcal{B}[B^0 \to \rho^0\gamma]/10^{-6}$	$\mathcal{B}[B^+ \to \rho^+\gamma]/10^{-6}$
Bosch and Buchalla [22]		1.6 ± 0.5
Ali and Parkhomenko [24]	0.49 ± 0.18	0.90 ± 0.33
CLEO [31]	< 17	< 13
BELLE [33]	< 10.6	< 9.9

Table 1.2: Theoretical predictions for $\mathcal{B}[B \to \rho\gamma]$ and $\mathcal{B}[B \to K^*\gamma]$ and current experimental results.

1.4 Current Theoretical and Experimental Status

Several groups have calculated $\mathcal{B}[B \to \rho\gamma]$ and $\mathcal{B}[B \to K^*\gamma]$ employing factorization and heavy quark effective theory at leading order in Λ_{QCD}/m_B to incorporate form factors into the weak effective Hamiltonian. Their results are summarized in Table 1.2 together with recent measurements by the CLEO and BELLE collaborations. The theoretical calculations for $\mathcal{B}[B \to K^*\gamma]$ are consistently higher than the experimentally measured rates. Two of the papers discuss this discrepancy resulting from the form factor calculations [22][24]. By comparing the experimentally obtained

results for the exclusive rate $\mathcal{B}[B \to K^*\gamma]$ and the inclusive rate $\mathcal{B}[B \to X_s\gamma]$, one obtains an estimate for the form factor which is considerably smaller than the calculations shown in Table 1.1. The estimate of $\mathcal{B}[B \to \rho\gamma]$ by Ali and Parkhomenko [24] is calculated using the smaller form factor extracted in this manner, while Bosch and Buchalla use the higher value obtained from the light cone sum rules.

Due to these uncertainties, it is not possible to obtain a useful estimate on $|V_{td}|$ or $|V_{ts}|$ individually from $\mathcal{B}[B \to \rho\gamma]$ and $\mathcal{B}[B \to K^*\gamma]$. Ali and Parkhomenko [24] explore the possibility of extracting the ratio $|V_{td}/V_{ts}|$ through the ratio of the two decay rates:

$$\frac{\mathcal{B}[B \to \rho\gamma]}{\mathcal{B}[B \to K^*\gamma]} = S_\rho \left|\frac{V_{td}}{V_{ts}}\right|^2 \left[\frac{1 - m_\rho^2/M^2}{1 - m_{K^*}^2/M^2}\right]^3 \zeta^2[1 + \Delta R(\rho/K^*)], \tag{1.24}$$

where S_ρ is an isospin factor (1 for $B^+ \to \rho^+\gamma$, 1/2 for $B^0 \to \rho^0\gamma$) and some of the uncertainty in the form factors is expected to cancel in the ratio $\zeta = F_1^{B\to\rho}(0)/F_1^{B\to K^*}(0)$. The light cone sum rule calculation predict $\zeta = 0.76 \pm 0.06$ [17] and $\zeta = 0.75 \pm 0.07$ [18]. The uncertainty in ΔR, which represent corrections from hard-spectator interactions and annihilation contributions, is expected to be less than 25%. If true, $|V_{td}/V_{ts}|$ can be extracted with less than 15% theoretical uncertainty. However, the discrepancy in the prediction of $\mathcal{B}[B \to K^*\gamma]$ has opened a debate of whether the form factor calculations are reliable, both individually or in the ratio. Other authors assign a more conservative error to the form factor ratio of up to 30% [27]. Nonetheless, current experimental limits are still an order of magnitude larger than the most optimistic estimates of $\mathcal{B}[B \to \rho\gamma]$. Observation of this decay is of considerable interest as first evidence of the $b \to d\gamma$ transition and the first step towards determining $|V_{td}/V_{ts}|$ in radiative B decays.

Chapter 2

The *BABAR* Detector

The *BABAR* detector was built to study the decay of B mesons produced by the $PEP-II$ asymmetric electron-positron collider. The primary purpose of the detector is the study of time-dependent asymmetries of B and $\overline{B}$ meson decays which shed light on CP violation in the CKM Model. However, the detector is versatile enough to cover the full range of B meson physics performed by previous experiments. This section details the various components of the *BABAR* detector, following a brief description of the $PEP-II$ storage ring and its performance.

2.1 The $PEP-II$ Collider

The $PEP-II$ asymmetric collider consists of two storage rings which collide 9.0 GeV electrons on 3.1 GeV positrons. The energies are selected to produce the $\Upsilon(4S)$ resonance with a boost of $\beta\gamma = 0.56$. In the interaction region where the *BABAR* detector is located, the beams are brought into head-on collision and separated using dipole magnets.

The electron and positron beams are stored with currents of over 1.0 A and 1.5 A, respectively, in 1658 bunches $120\,\mu\text{m} \times 5.6\,\mu\text{m} \times 9\,\text{mm}$ in size. The design luminosity of $3 \times 10^{33}\,\text{cm}^{-2}\,\text{s}^{-1}$ has been achieved and exceeded. Approximately 10% of the data is taken 40 MeV below the $\Upsilon(4S)$ resonance (*off-resonance* data), resulting in a control sample of u, d, s and c quark-antiquark pairs and $\tau^+\tau^-$ pairs produced in

the continuum without $B\overline{B}$ production.

2.2 The *BABAR* Detector

The study of the B decays typically proceeds by fully reconstructing the decay chain to its final state particles consisting of charged hadrons (pions, kaons and protons), charged leptons (electrons and muons) and photons. Intermediate states in the decay chain are reconstructed as a composition of the appropriate particles, *e.g.* $K_S^0 \to \pi^+\pi^-$ and $\pi^0 \to \gamma\gamma$. In general, the unambiguous reconstruction of the complete decay chain and kinematics requires the following information from the detector:

- The momentum and charge of charged tracks.
- The identity of each charged track: electron, muon, pion, kaon or proton.
- The energy and direction (momentum) of photons.

For the study of time-dependent asymmetries, the vertex information of the decay is also necessary. This is obtained from precise measurement of not only the momenta of the charged tracks, but also their trajectory through the detector.
The *BABAR* detector is composed of the five components shown in Figure 2.1, each providing complementary information about the decay products necessary for the full reconstruction of the B decay. In order from innermost to outermost, the sub-components, together with their primary tasks, are:

- Silicon Vertex Detector (SVT):
  Precise tracking of charged particles near the interaction region.
- Drift Chamber (DCH):
  Precise tracking and momentum measurements of charged particles
- Ring-imaging Cherenkov Detector (DIRC):
  Charged particle identification: pion/kaon/proton discrimination.
- Electromagnetic Calorimeter (EMC):
  Position and energy reconstruction of photons and identification of electrons.

- Instrumented Flux Return (IFR):
  Hadron/muon discrimination

Except for the IFR, the components are embedded in the 1.5 T superconducting solenoid. The curvature of the charged tracks in the magnetic field enables the measurement of the momentum and sign of each track.
The electronics of the various components share a common architecture. Each detector component has front-end electronics (FEE) mounted directly on the detector system which digitize the detector output, forward the information to the trigger system and buffer the information for readout pending an accept trigger. The output from the FEE are transferred to storage via Readout Modules (ROM) consisting of a *personality card* which interfaces via optical cables to the component-specific FEE and a single board computer that processes the FEE output for the fast control and timing system (FCTS) and the event builder.
The following sections describe the design and performance of each of the subdetectors. A detailed description of the EMC and its calibration is given in the following chapter.

2.3 The Silicon Vertex Tracker (SVT)

The purpose of the silicon vertex tracker (SVT) is to measure the trajectories of charged particles near the beam interaction region and provide precise information on decay vertices. The SVT is capable of stand-alone tracking of tracks with insufficient transverse momentum to traverse the drift chamber. Measurements of the charge collected in the silicon strips provide information on the specific ionization used for particle identification. The SVT also measures the angles of the tracks necessary for the DIRC reconstruction.

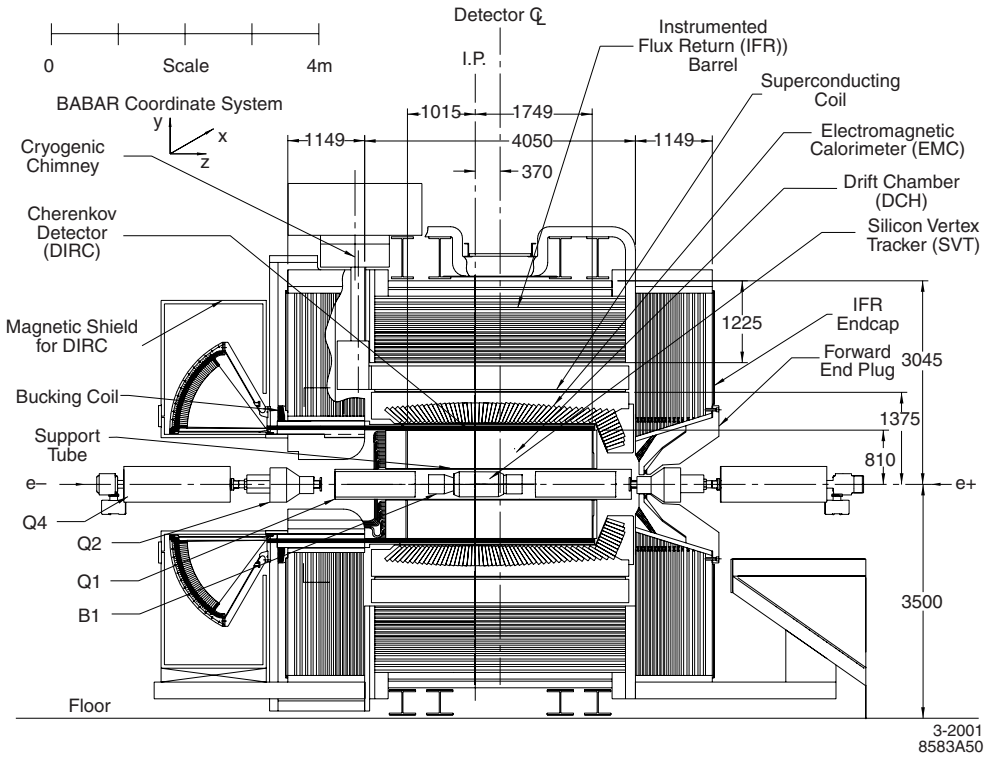

Figure 2.1: Longitudinal section of the *BABAR* detector.

2.3.1 SVT Layout

The SVT layout is depicted in Figure 2.2. The detector consists of five sets of silicon strip modules arranged in concentric layers. The three innermost layers consist of six modules, and the two outermost layers are composed of sixteen and eighteen modules. The silicon detectors are double-sided: on one side, the readout strips run parallel to the beam (ϕ strips), on the other, the strips run perpendicular to the beam (z strips). The readout pitch varies from 50 to 210 μm; in some cases there are *floating strips* (a strip that is not read out) between two active strips.

The modules of the three innermost layers are assembled straight and positioned close to the beam pipe to optimize point resolution. The outer two layers are arch-shaped to increase coverage and reduce the angle of incidence. The forward and backward acceptance, which extend to 350 mrad and 520 mrad respectively, as well

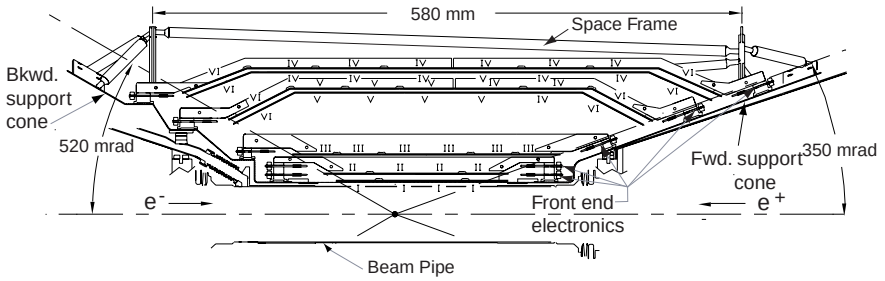

Figure 2.2: Longitudinal section of the SVT

as the proximity of the innermost layer to the interaction point (32 mm radius), are limited by the beam pipe and magnets in the interaction region.

2.3.2 SVT Electronics

Data from the approximately 150,000 readout channels are delivered via fanout circuits to a custom ATOM (A Time-Over-Threshold Machine) integrated circuit. In the ATOM, the analog signal is preprocessed by a preamplifier and shaping circuit and transformed into a pulse varying quasi-logarithmically with the integrated charge by a comparator. The comparator output is sampled at 15 MHz onto a 193 bin circular buffer. The Level I trigger (see Section 2.8.1) initiates the readout of the buffer into an event buffer, which is delivered with a time stamp and strip address to the Read-Out Module (ROM) if the Level I accept is received. The front-end electronics are mounted adjacent to the silicon strips on the beam pipe support and support structure.

2.3.3 Reconstruction and Performance

The reconstruction of SVT hits starts by removing hits that are out-of-time relative to the event time derived from the DCH. The remaining adjacent hits are clustered, with hit positions weighted by charge to calculate the cluster position. The cluster

positions are then used by the track-finding algorithms. Accurate alignment information is critical in obtaining precise trajectory measurements. The alignment of the SVT is determined in two steps: the local alignment, which determines the relative positions of the individual SVT modules, and the global alignment, which determines the position of the SVT as a whole relative to the DCH. The local alignment is performed as often as necessary, typically after detector access, using $e^+e^- \to \mu^+\mu^-$ and isolated tracks from hadronic events. The global alignment is performed every few hours in order to correct for diurnal motion of the SVT resulting from temperature variations. The procedure minimizes the offset between tracks sections reconstructed in the SVT and the DCH by varying three rotation and three translation parameters. The achieved hit resolution varies between 20 to 40 μm depending on the incident angle of the track on the SVT module. The dE/dx resolution for minimum-ionizing particles sampled over five layers is 14%.

2.4 The Drift Chamber

The Drift Chamber (DCH) provides the detection of charged particles and the precise measurement of their kinematics necessary for the reconstruction of B meson decays with high efficiency and low background. Ionization loss measurements provide dE/dx information for particle identification which complements the SVT and DIRC. The DCH also reconstructs the decay vertices of long-lived particles, such as the K^0_S and Λ^0, which may decay outside of the SVT.

2.4.1 Design and Geometry

The DCH is constructed from two concentric cylinders with radii of 236 mm and 809 mm as shown in Figure 2.3. There are 40 radial layers of hexagonal cells organized in 10 superlayers of four layers each. In total, there are 7,104 drift cells. The wires are oriented at various angles with respect to the z axis by superlayer to obtain longitudinal information as shown on the right in Figure 2.3. The stereo angles alternate in

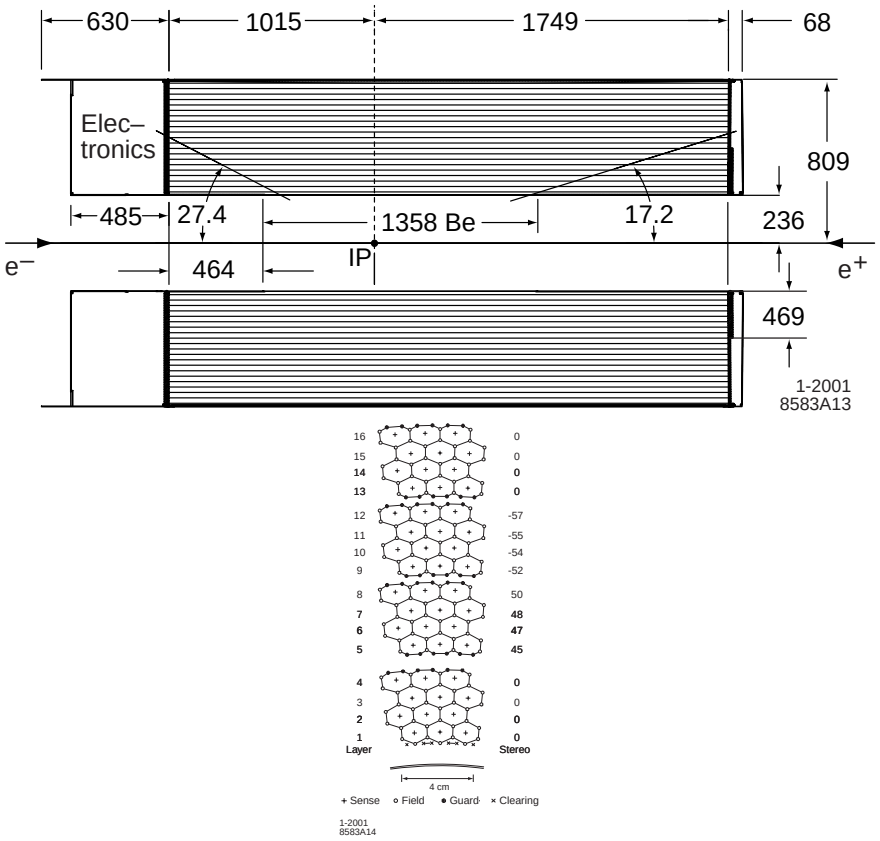

Figure 2.3: Left: Longitudinal section of the DCH. Right: Schematic layout of drift cells in the four inner superlayers.

the pattern AUVAUVAUVA for the ten superlayers, where A is axial view (parallel to the z axis), and U and V are the stereo views, with angles increasing radially from 45 and 76 mrads.

The DCH uses 80:20 mixture of helium and isobutane to minimize multiple-scattering, the dominant component of the resolution at momenta below $1\,\mathrm{GeV}/c$, the typical momentum of tracks from B decays. In total, the DCH contributes $1.08\%X_0$ of material in front of the DIRC.

The polar acceptance of the detector, defined as the extreme angle at which a particle from the origin crosses at least 20 layers, is 17.2° in the forward direction, and 27.4° in the backward direction, as shown in Figure 2.3. The azimuthal acceptance

is complete.

2.4.2 Electronics and Readout

The front-end electronics of the DCH are mounted on the back endplate in 16 azimuthal sectors. No components are mounted on the front endplate in order to minimize material in front of the EMC. Each sector consists of service boards providing high voltage to the wires and the Front- End Assembly (FEA) mounted on the back of the service boards. On the FEAs, a combination 4 bit TDC and 6 bit 15 MHz FADC circuit processes the amplified sense wire output and digitizes the charge deposition and drift time.

2.4.3 Reconstruction

The drift time-to-distance relationship and gas gain are needed to determine the drift distance and ionization loss from the recorded information. The time-to-distance relationship for a given layer is obtained using tracks from Bhabha and μ-pair events. The track trajectory is reconstructed with all the hits excepting the wire in question. The drift time together with the point of nearest approach to the wire for this trajectory is used to determine the time-to-distance relationship. The overall gas gain is obtained from the charge collected from tracks in Bhabha scattering events. The charge collected on individual wires is corrected for geometric effects, as well as variations in the electronics response.

2.4.4 Tracking

Track Finding

The track reconstruction starts from track segments and pattern recognition information obtained from the Level 3 DCH algorithm (Section 2.8.2). Using the track segments found by the Level 3 algorithm, the event time t_0 is improved by re-fitting the track parameters in each segment with varying t_0. Additional hits are added to the tracks as the t_0 is recalculated with the newly added hits. Using the improved t_0

information, two additional track-finding algorithms are employed to identify tracks which do not originate from the interaction point or do not traverse the entire length of the DCH.
The tracks found by this algorithm are re-fit using the Kalman filter, which accounts for local variations in material and magnetic field in the fitted trajectory, and extrapolated through the SVT. SVT track segments are added to the track if they are consistent with the extrapolation. Two additional track-finding algorithms are used to find SVT stand-alone tracks.

Performance

The efficiency for DCH tracking has been determined to be $98 \pm 1\%$ by comparing the number of tracks found in the SVT that extrapolate into the DCH acceptance with the number of tracks actually found by the DCH. For SVT-only tracks, the efficiency is greater than 80% down to $p_T \approx 70\,\mathrm{MeV}/c$
The tracking resolution in the parameters d_0, z_0 (transverse distance and z coordinate at the closest approach to the z axis), ϕ_0 (azimuthal angle) and λ (dip angle to the transverse plane) can be obtained from Bhabha scattering and $e^+e^- \to \mu^+\mu^-$ events by comparing the difference of the parameters obtained for the two tracks at the point of their closest approach. The p_T resolution, dominated by the DCH, can likewise be studied with cosmic ray muons. The resolutions obtained from these studies are:

$$\begin{aligned} \delta d_0 &= 23\,\mu\mathrm{m} & \delta z_0 &= 29\,\mu\mathrm{m} \\ \delta\phi_0 &= 0.43\mathrm{mrad} & \delta\tan\lambda &= 0.53 \times 10^{-3} \end{aligned} \tag{2.1}$$

$$\sigma_{p_T}/p_T = (0.13 \pm 0.01\%)p_T + (0.45 \pm 0.03)\%$$

2.5 The Ring-Imaging Cherenkov Detector (DIRC)

The DIRC (Detector of Internally Reflected Cherenkov light) is a novel ring-imaging Cherenkov radiation detector used for the identification of charged hadrons. The required momentum coverage of the DIRC is characterized on one end by kaon tagging

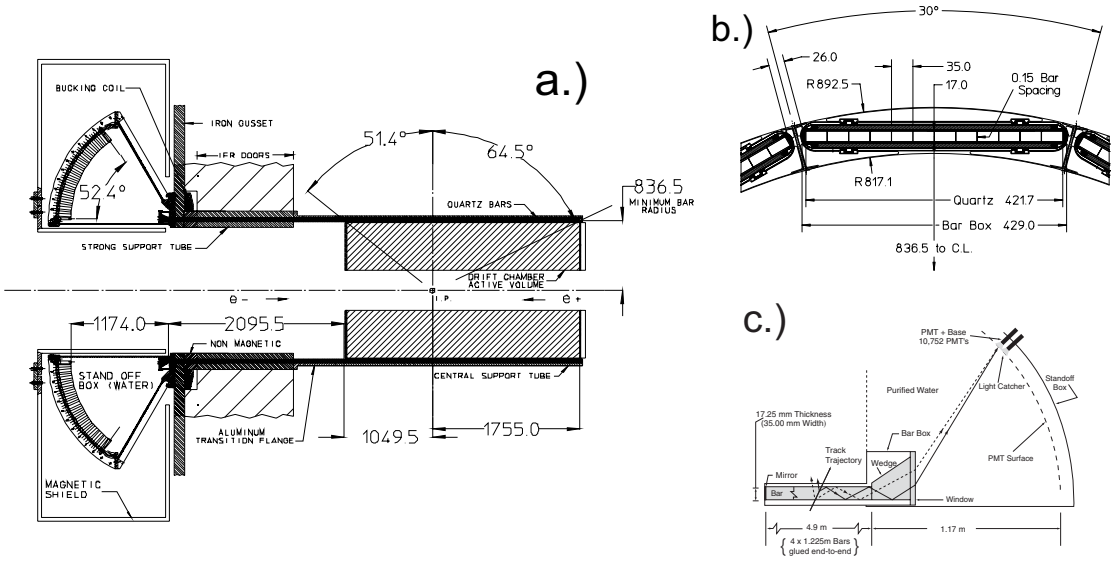

Figure 2.4: a.) The elevated view of overall DIRC geometry. b.) Barbox construction. c.) Bar/SOB transition region.

for time-dependent asymmetry measurements, where the typical momentum is less than 1 GeV/c, and on the other end by K/π separation for the $B^0 \to \pi^+\pi^-/K^+\pi^-$ analysis, where momenta range from 1.7 to 4.2 GeV/c. The lower threshold for the DIRC is dictated by the 280 MeV/c of transverse momenta necessary to traverse the DCH and reach the DIRC.

2.5.1 Design and Geometry

The DIRC is implemented as a barrel of 144 synthetic fused silica bars surrounding the DCH and an array of 10752 photomultipliers in the standoff box (SOB) behind the rear IFR doors as shown in Figure 2.4. Cherenkov radiation emitted by charged particles traversing the bars is propagated by internal reflection to the photomultiplier array in the SOB, where the ring is reconstructed to determine the Cherenkov angle. The index of refraction of the bars is 1.473.

The quartz bars are mounted inside 12 aluminum bar boxes, each containing 12 bars. The bars extend along the entire length of the DCH, covering polar angles down to 25.5°. The acceptance in the backward direction ends at 38.6°. The bars extend backward through the IFR doors to the SOB. The barbox construction is shown on the top right in Figure 2.4

The SOB is a water tank extending conically from the bars. An array of 29 mm ETL 8125 photomultipliers (PMTs) is mounted on the back wall in twelve sectors of 896. The index of refraction of water ($n = 1.346$) is close to that of the silica bars, resulting in minimal reflection at the interface. At the end of each bar is a silica wedge prism designed to recover photons at wide angles relative to the bar axis by reflection, as shown in Figure 2.4. The typical distance between the end of the bar and the photomultipliers is 1.17 meters. At this distance, the photon angular resolution resulting from granularity of the photomultiplier array is approximately 7 mrad, so that this geometric contribution to the resolution is larger than the intrinsic dispersion of the Cherenkov cone (approximately 5.4 mrad) and the dispersion from photon transmission.

2.5.2 Electronics and Reconstruction

The DIRC Front-end Boards (DFBs) hold TDC and FADC circuits for 64 photomultiplier signals. The 16-channel TDC has 0.5 ns binning in order to determine the photon arrival time to within the 1.5 ns spread resulting from the transit time. The digitized information is sent to the ROMs via optical fibers.

Precise timing of DIRC PMT signals is critical for the reconstruction. The DIRC

timing calibration uses a 1 ns pulses from blue LED light pulsers. With approximately 65,000 TDC times accumulated in the Readout Modules from each PMT, the timing is calibrated to a statistical accuracy of less than 0.1 ns. A complementary method uses comparisons of observed and expected arrival times from tracks in the collision data. The two calibrations are found to be consistent.

The DIRC reconstruction of a charged track starts by determining for each photomultiplier signal the coordinates in the Cherenkov cone system based on the PMT location and the position of the end of the bar through which the track traversed. The coordinates are θ_C and ϕ_C, the polar and azimuthal angle relative to the cone direction, and δt, the time relative to the expected arrival. A sixteen-fold ambiguity results from the last reflection in the bar (top/bottom, left/right), whether the photon scattered off the wedge, and whether the photon propagated initially forward or backward. The timing resolution is critical in reducing this to a threefold ambiguity and reducing background hits by a factor of forty. The reconstruction algorithm then maximizes likelihood of the entire event based on the individual track likelihoods for the electron, muon, pion, kaon and proton hypotheses. For momenta between 0.5 and 3 GeV, combined with dE/dx information from the SVT and DCH, the DIRC achieves kaon identification with efficiency greater than 90% and less than 3% pion misidentification for tracks that intersect the radiator bars.

2.6 The Electromagnetic Calorimeter

The Electromagnetic Calorimeter (EMC) provides the precise measurement of photon energy and direction from 20 MeV up to the kinematic limit of 9 GeV. The range is necessary in part to reconstruct the mode $B^0 \to \pi^0\pi^0$, where the fast π^0 produce highly asymmetric photon pairs. The measurement of energy deposited in the EMC by charged tracks (E) is also the primary input for electron identification through E/p.

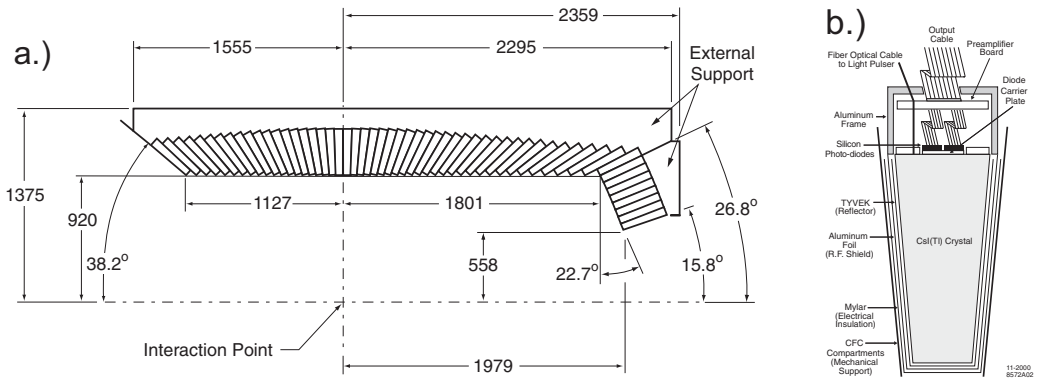

Figure 2.5: a.) Longitudinal section of top half of the EMC. b.) Crystal housing with front-end electronics.

2.6.1 Geometry

The EMC is an array of Thallium-doped Cesium Iodide (CsI(Tl)) crystals consisting of two parts: the cylindrical barrel and the forward endcap. In total, the EMC contains 6580 crystals arranged in 48 rings of 120 crystals comprising the barrel and rings of 120, 100 and 80 crystals comprising the endcap. The segmentation gives the excellent angular resolution ($\sim$ few mrad) necessary for high energy π^0 reconstruction. The geometry of the detector is shown in Figure 2.5. The choice of CsI(Tl) results from the requirements of energy resolution, radiation hardness and stopping power. The typical light yield for the crystals is 50000 photoelectrons per MeV.

2.6.2 Electronics

Two silicon photodiodes are mounted at the end of the CsI(Tl) crystals, as shown in Figure 2.5, along with two low-noise preamplifier contained within the crystal fixture. The output from the photodiodes feeds into the *custom auto-range coding* (CARE) circuit with amplification factors of either 1 or 32. Since these front-end components are inaccessible during normal operation of the detector, the twofold photodiode/preamplifier redundancy is adopted to ensure reliability. The CARE chip can be set to read either channel or an average of both.

Further choice of amplification using the CARE chip allow gains of 256, 32, 4 and 1 for the energy ranges $0 - 40\,\mathrm{MeV}$, $50 - 400\,\mathrm{MeV}$ $0.4 - 3.2\,\mathrm{GeV}$ and $3.2 - 13\,\mathrm{GeV}$, respectively. This choice of ranging effectively allows a 18 bit dynamic range across the entire energy spectrum. The signal output from the CARE chip, along with the rangebits, are sent via optical fiber to the ROMs.

2.6.3 Calibration and Monitoring

The EMC response and stability are monitored by a number of calibrations. The crystal light yields, which decrease with radiation damage, are calibrated at low energies by circulating irradiated Fluorinert through the detector and measuring the $6.13\,\mathrm{MeV}$ peak of the emitted photons. A high energy calibration of the light yield using Bhabha scattering events calibrates the measured deposited energy to the predictions from Monte Carlo simulation. These calibrations are described in detail in Section 3. A third system, the Xenon light pulser, performs daily monitoring of the relative crystal response.

2.6.4 Performance

The energy and angular resolution of photons reconstructed in the EMC has been determined from data control samples such as symmetric π^0 and η decays. At one end of the energy range, the source calibration at $6.13\,\mathrm{MeV}$ gives a fractional resolution of $5.0 \pm 0.8\%$, and at the other end, Bhabha scattering events give a resolution of $1.9 \pm 0.07\%$ from $3 - 9\,\mathrm{GeV}$. The energy resolution can be parameterized by:

$$\frac{\sigma_E}{E} = \frac{(2.32 \pm 0.30)\%}{\sqrt[4]{E(\,\mathrm{GeV})}} \oplus (1.85 \pm 0.12)\% \tag{2.2}$$

The first term results from statistical fluctuations in the scintillation photon yield, as well as beam background and electronics noise. These effects become relatively less important at higher energies. The second term, constant in energy, is associated with leakage and absorption in front and in between crystals.

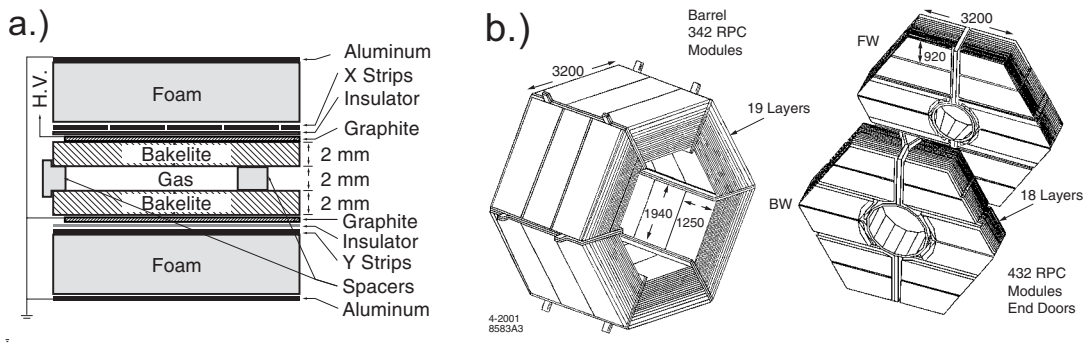

Figure 2.6: a.) The Resistive Plate Chamber (RPC) system. b.) Geometry of the IFR system

2.7 The Instrumented Flux Return

The Instrumented Flux Return (IFR) identifies muons by providing information on the penetration of charge particles through the steel of the solenoid flux return. Neutral hadrons, such as neutrons and K_L^0 are also identified through their interaction in the steel. The neutral hadron reconstruction is limited to direction; the calorimetric information is too coarse to provide useful input. The steel of the IFR is segmented into nineteen layers arranged in hexagons extending radially in the barrel section. For forward and backward coverage, the end door steel has 18 gaps, as shown in Figure 2.6. The gaps are instrumented with resistive plate chambers (RPCs) which detect charged particles and interactions of neutral hadrons traversing the steel.

2.7.1 The Resistive Plate Chambers

The configuration of the RPC system is shown on the left in Figure 2.6. The 2 mm gap between the two layers of Bakelite is filled with a mixture of Argon, Freon, and isobutane at $\sim$ 1500 torr of pressure. A potential of 8 kV is maintained via a graphite layer deposited on the external surface of the Bakelite. When the gas is ionized by a charged particle traversing the gap, the discharge is detected by aluminum strip electrodes which run in perpendicular directions on the outside of the Bakelite. The Bakelite is chosen for its resistive properties ($10^{11-12}\Omega$ - cm) which

localize the discharge.
The RPCs modules are produced in modules of up to $320 \times 130\,\mathrm{cm}^2$. In the barrel, three modules are used to cover the gaps in each hexagonal face of the steel in each layer. The set of modules extending radially and covering the same z and ϕ regions define a *sector*. The readout strips in each module are arranged in 32 rows perpendicular to the beam, providing z coordinate information and 96 rows parallel to the beam for the ϕ coordinate. Each half of the end doors have three vertical sections, each containing two RPC modules.

2.7.2 Reconstruction

The IFR reconstruction joins hits across layers into two-dimensional clusters in each dimension. Within each sector, clusters in each dimension are then combined into a three dimensional cluster.
Muon identification in the IFR starts by associating hits in the RPC strips within a certain transverse distance from the extrapolated trajectory of a reconstructed charged track. Selections are based on information such as the quality of the cluster-track match and a comparsion of the interaction lengths traversed by the track in the detector and the expected number of interaction lengths for a muon of the same momentum and angle. The minimum momentum for muon identification using the IFR is about $600\,\mathrm{MeV}/c$, based on the transverse momentum necessary to enter the detector. Between momenta of 1.5 and $3.0\,\mathrm{GeV}/c$, where most of the primary leptons from semileptonic decays of the B meson lie, the IFR achieves nearly 90% efficiency for muon identification with $6 - 8\%$ pion misidentification.

2.8 Trigger

At the $PEP - II$ design luminosity, beam-related background events occur at over 20 kHz, while events of physics interest ($B\overline{B}$, τ events, etc.) occur at rates of several Hz. The trigger system must reduce the data-taking rate to a manageable rate for

the online reconstruction (approximately 120 Hz), while selecting events of interest with high efficiency and low deadtime. In particular, the trigger system is required to have at least 99% efficiency for $B\overline{B}$ events and 95% for continuum events with at most 1% deadtime.
The trigger is implemented in two layers: The Level 1 (L1) hardware trigger, designed to reduce the output rate to 1 kHz, and the Level 3 (L3) software trigger.

2.8.1 The Level 1 Trigger

The Level 1 trigger consists of three components: one based on DCH information (DCT), one on EMC information (EMT) and diagnostic trigger based on IFR information (IFT).

The Drift Chamber Trigger

The DCT takes data from each of the DCH cells and implements a fast 24 module *Track Segment Finder* (TSF) using the ϕ coordinate and drift times of the hits. These segments are passed to the *Binary Link Tracker*, which bins the segments into *supercells* dividing the DCH into 32 ϕ bins and 10 superlayers. The BLT starts from the innermost layer and links segments in contiguous supercells. Eight transverse momentum discriminator (PTD) modules determine the number of tracks above a certain threshold. The output of the DCT are 16 bit *trigger primitives* which categorize the BLT and PTD results into short (traversing half the DCH), long (traversing the entire DCH) and high P_T ($> 800\,\mathrm{MeV}/c$) tracks.

The EMC Trigger

For the EMT, the EMC is divided into 280 towers which bin the detector into 7 regions in θ and 40 sectors in ϕ. In each ϕ sector, the energy is summed considering all crystal depositions above 20 MeV. These sums are used to make the EMT trigger primitives which consist of energy depositions in three bins, as well as an Endcap minimum-ionizing deposition primitive and a high-energy backward barrel deposition

primitive.
The DCT and EMT inputs are processed by the *global trigger* (GLT) to form specific triggers. The processing times for the DCT and EMT is approximately 5μs with an addition 4μs for the GLT to process and begin readout from the ROMs. The combined L1 triggers achieve nearly 100% efficiency for generic $B\overline{B}$ events.

2.8.2 The Level 3 Trigger

The Level 3 trigger runs a track-finding algorithm in the DCH (L3Dch) and a clustering algorithm in the EMC (L3Emc) to initiate the event reconstruction process.

The L3 DCH Reconstruction

The track-finding algorithm uses a Monte Carlo-based lookup table of hit patterns in order to associate track segments from the TSF to a track. A pattern matched to an entry in the lookup table is passed to an iterative fitting algorithm, which uses the segment hits and adds or drops hits based on their proximity to the fitted trajectory.

The L3 EMC Reconstruction

The clustering algorithm eliminates hits which are more than 1.3μs from the event time and isolated crystals with less than 20 MeV of energy. Clusters are formed from adjacent energy depositions, and the energy, lateral energy profile, time and centroid calculated for clusters with at least 100 MeV of energy.

Performance

Using the L3 tracks and clusters, events can be reconstructed, categorized, and accepted or rejected. The L3 information allows copious electrodynamic processes useful for calibration purposes, such as (radiative) Bhabha scattering and $e^+e^- \to \gamma\gamma$ events, to be identified and passed at reduced rates. Multiplicity criteria identify hadronic events from $B\overline{B}$ decays and the continuum. The combined L1 and L3 trigger achieves over 99.9% efficiency for $B\overline{B}$ events and over 95% for continuum events.

2.9 The Data

The data used in the $B \to K^*\gamma$ analysis consists of $20.7\,\mathrm{fb}^{-1}$ of on-resonance data and $2.6\,\mathrm{fb}^{-1}$ of off-resonance data taken in 1999-2000, while the $B \to \rho\gamma$ analysis includes data taken in 2001, for a total of $56.2\,\mathrm{fb}^{-1}$ of on-resonance data and $7.8\,\mathrm{fb}^{-1}$ of off-resonance data. The luminosity measurements typically have an error of 0.5%. Within the collision environment, the $\Upsilon(4S)$ production which actually produces $B\overline{B}$ pairs accounts for about a quarter of the total cross-section of hadronic production; the rest is continuum production. Other processes such as $e^+e^- \to \mu^+\mu^-$ and $e^+e^- \to \tau^+\tau^-$ are produced at rates comparable to the $\Upsilon(4S)$ production, while Bhabha scattering occurs at rates nearly forty times higher.

The total number of $B\overline{B}$ pairs produced in the data is determined by comparing the yield of hadronic events in the on and off-resonance data [39]. The yield in the off-resonance data is scaled by the luminosity determined from the yield of $e^+e^- \to \mu^+\mu^-$ to the on-resonance data and subtracted; the remainder is attributed to $B\overline{B}$ production in the on-resonance data. The number of $B\overline{B}$ pairs produced is determined to be $22.7 \pm 0.36 \times 10^6$ for the 1999-2000 data and $61.7 \pm 0.70 \times 10^6$ for the 1999-2001 data. Equal production of $B^0\overline{B}^0$ and B^+B^- is assumed.

The Monte Carlo simulation of specific channels as well as generic continuum and $B\overline{B}$ processes is based on a detailed detector simulation using GEANT [30]. Background estimates from these samples are obtained by scaling the event yields using the equivalent luminosity for the simulated sample based on the known cross-section for these processes. Due to the large amount of data available, the equivalent luminosity of the simulated generic background Monte Carlo samples is typically half that of the actual data.

Chapter 3

The Radiative Bhabha Calibration

3.1 Overview of the EMC Calibration

The reconstruction of high energy photons is a key ingredient of the $B \to \rho\gamma$ and $B \to K^*\gamma$ analyses. In the laboratory frame, the primary photons from these decay range from $1.5 - 4.5\,\mathrm{GeV}$. Proper calibration of the EMC response to photons of this energy is necessary to allow the exclusive kinematic reconstruction of these decays. The energy calibration of the EMC proceeds in two steps:

- A crystal light yield calibration which corrects the relative response for each crystal to a given amount of energy deposited in the crystal.

- A shower energy correction which corrects for energy not contained within the crystals due to material in front of and in between crystals, as well as leakage out of the back and in between the crystals. This correction is applied to reconstructed clusters and not to individual crystals.

The first corrects for the EMC response to energy actually deposited in the crystals, while the second corrects for energy not contained in the crystals.

3.1.1 Crystal Light Yield Calibration

The light yield calibrations occur at the extreme ends of the EMC energy range. At the lower end, the calibration is performed with 6.13 MeV photons from a source. At the high end, the corrections are obtained from Bhabha scattering events, which provide a large sample of electrons and positrons at the kinematic limit ($3 - 9$ GeV depending on polar angle) produced *in situ* from the e^+e^- collisions.

Source Calibration

The source calibration uses 6.13 MeV photons from the following radioactive decay chain initiated by bombarding Fluorine with neutrons:

$$^{19}\mathrm{F} + n \rightarrow {}^{16}\mathrm{N} + \alpha,\ {}^{16}\mathrm{N} \rightarrow {}^{16}\mathrm{O}^* + \beta,\ {}^{16}\mathrm{O}^* \rightarrow {}^{16}\mathrm{O} + \gamma(6.13\,\mathrm{MeV}) \tag{3.1}$$

The fluorine is distributed in the form of Fluorinert[29]. A neutron gun is used to irradiate Fluorinert, which is circulated immediately in front of the crystals by aluminum pipes. The decay photons are observed in the crystals, resulting in the spectrum shown in Figure 3.1 with two escape peaks at 5.62 MeV and 5.11 MeV. The fitted peak position then gives the crystal light yield correction. The calibration can be performed in forty minutes to obtain a statistical precision of 0.35%. Weekly calibrations monitor the degradation in the light yield from radiation damage, as shown in Figure 3.1. The damage is worst in the forward region, where the light yield decreased approximately 8% in the first year of data taking. However, the observed damage is less than the 10% loss expected in the design of the EMC.

The Bhabha Calibration

A clean sample of Bhabha scattering events, which provide electrons and positrons monoenergetic at a given polar angle, can be extracted from the two prong event sample by simple kinematic selection based on the reconstructed tracks. The calibration compares the reconstructed deposited energy in the calorimeter to a table of expected values derived from Monte Carlo simulation as a function of the entry

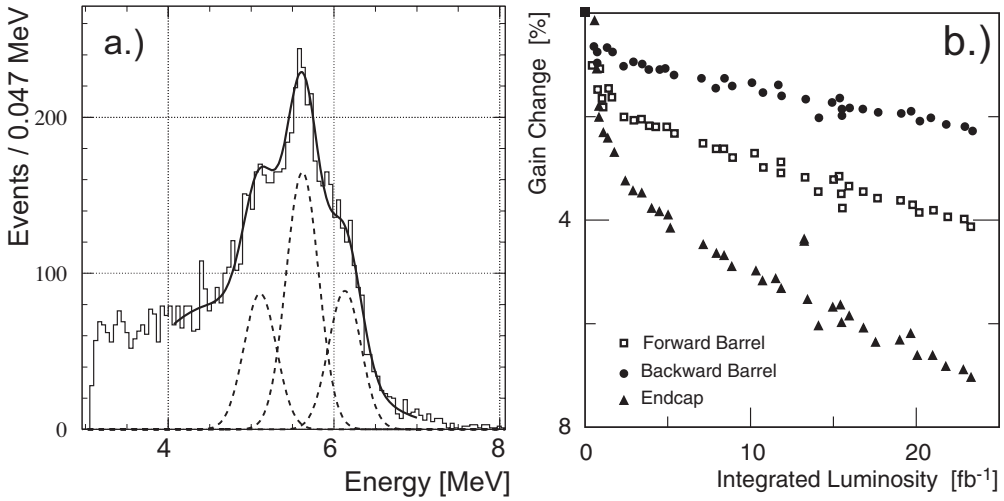

Figure 3.1: a.) Typical spectrum from the 6.13 MeV source photons. b.) Measured light output in the first year of data taking.

position of the track into the EMC. The table accounts for variations in the expected deposited energy due to differences in the material in front of the EMC, most notably the DIRC, as well as the intercrystal leakage properties that vary with the entrance point of the track on the face of the crystal. The calibration, however, does not calibrate for these variations; they are inputs from the Monte Carlo simulation
The calibration for each crystal is obtained by solving a series of linear equations resulting from a χ^2 minimization of the difference between the expected and observed deposited energy as a function of the crystal calibrations.

3.1.2 Leakage Corrections

Currently, the leakage corrections are derived from two sources: at low energies, the $\pi^0 \rightarrow \gamma\gamma$ decay is used to determine a correction in terms of the polar angle and energy of the photons by constraining the reconstructed mass to the known π^0 mass. At higher energy, where photons from π^0 decays are typically highly asymmetric in energy, a correction from the Monte Carlo simulation is used. It is desirable to have a data-based control sample that can cross check this calibration and determine effects that may not be properly simulated in the Monte Carlo. The radiative Bhabha

scattering process provides such a sample.

3.2 The Radiative Bhabha Calibration

The radiative Bhabha scattering process, in which a Bhabha scattering event is accompanied by the radiation of a photon from the electron or positron in the initial or final state, provides a large sample of photons across nearly the entire phase space. The reconstruction of the electron and the positron in the DCH, along with the photon direction, allow the energy of the photon to be determined in a kinematic fit. The predicted energy can be compared with the reconstructed energy to determine a correction. The photons can be binned in angle and energy to correct for leakage effects that may vary as a function of energy and angle of the radiated photon. The goal of the calibration is to provide corrections with an accuracy of 0.5% across the entire EMC for photons with momenta greater than 500 MeV.

3.2.1 The Kinematic Fit

The kinematic fit follows from energy and momentum conservation based on the kinematics of the initial state (the electron and positron beam), the detector-reconstructed kinematics of the outgoing electron and positron tracks, and the direction of the photon obtained from the reconstructed centroid of the photon cluster. Altogether, nineteen variables are determined in the fit:

- momenta of incoming electron and positron (six variables)
- momenta of outgoing electron and positron (six variables)
- Θ_γ, Φ_γ and E_γ: direction and energy of the photon (three variables).
- λ_i: Four Lagrange multipliers for the energy and momentum conservation constraints.

The χ^2 of the fitted result can be expressed as:

$$\begin{aligned}\chi^2 &= (f-m)^T V^{-1}(f-m)+ \\ &\quad \lambda_1[p_x^i - p_x^f - E_\gamma \sin\Theta_\gamma \cos\Phi_\gamma] \\ &\quad \lambda_2[p_y^i - p_y^f - E_\gamma \sin\Theta_\gamma \sin\Phi_\gamma] \\ &\quad \lambda_3[p_z^i - p_z^f - E_\gamma \cos\Theta_\gamma] \\ &\quad \lambda_4[E^i - E^f - E_\gamma]\end{aligned} \tag{3.2}$$

Here, f is the vector of fourteen quantities determined by the fit (incoming e^+e^- momenta, outgoing e^+e^- momenta and the direction of the photon in terms of Θ_γ and Φ_γ), m is the vector of corresponding measured values and V is the covariance matrix for these fourteen quantities. p^i and p^f are the incoming and outgoing momentum vectors of the e^+e^- pair determined by the fit, and E_γ, Θ_γ and Φ_γ are the energy, polar angle, and azimuthal angle of the outgoing photon determined by the fit. The first line in Equation 3.2 assesses the χ^2 from the deviation of the fitted quantities to their measured values and covariances, while the four Lagrange multiplier terms enforce energy and momentum conservation. By minimizing the χ^2, the expected photon energy E_γ is determined along with the other kinematic quantities independent of the energy reconstructed in the EMC. The iterative algorithm for minimizing the χ^2 used in this fit are documented in Reference [35].

3.2.2 Event Reconstruction and Photon Selection

The event reconstruction proceeds by identifying electron-positron tracks and requiring that there are no other tracks in the event. A simple electron selection requires the EMC deposition of both tracks to be greater than 500 MeV. This removes radiative muon pair production, which in principle are valid calibration candidates, but are kinematically different due to the muon mass.

Photons reconstructed in the EMC are selected by requiring that they are separated from the electron and positron clusters, and that they contain no problematic channels. For each photon candidate, the χ^2 of the $e^+e^-\gamma$ combination is estimated by

the reconstructed kinematics. The energy of the photon is estimated from energy conservation, and a χ^2 is calculated by determining the difference in the total initial and final state momentum vector, which should be zero. The covariance matrix for this 3×3 matrix is determined from the full 14×14 matrix according to the derivatives of the momentum vector with respect to the each of the fourteen quantities, resulting in a 3×14 transformation matrix which translates the covariance of the fourteen quantities to the covariance of the three components of the total momentum. The estimated χ^2 analytically determines the compatibility of the $e^+e^-\gamma$ combination with momentum conservation analytically, independent of the photon energy reconstructed in the EMC, and without resorting to the time-consuming iterative procedure for each combination.

The $e^+e^-\gamma$ combination with the least estimated χ^2 is selected and the full iterative χ^2 fit is performed with this combination. The fit predicts the energy of the photon, which can be compared to the reconstructed energy to determine the correction. The performance of the fit in determining the true energy of the photon is illustrated from the Monte Carlo simulation in Figure 3.2 for three different energies spanning the range of the calibration, and three different polar angles spanning the geometric acceptance of the EMC. The distributions show the ratio of the fitted photon energy to the true energy fit to the sum of two Gaussian distributions. The tails to the right of the distribution result from additional radiation in the event, which leads to an overestimate of the photon energy in the fit.

3.2.3 Determining the Correction

The correction is determined from the ratio E_R/E_F, where the E_R is the reconstructed energy in the EMC prior to the correction and the E_F is the energy predicted by the fit. The E_R/E_F values are binned in polar angle Θ, azimuthal angle Φ and fitted energy E_F. The distribution of E_R/E_F from events within the bin are fit to determine the peak position of E_R/E_F, which in turn gives the correction for

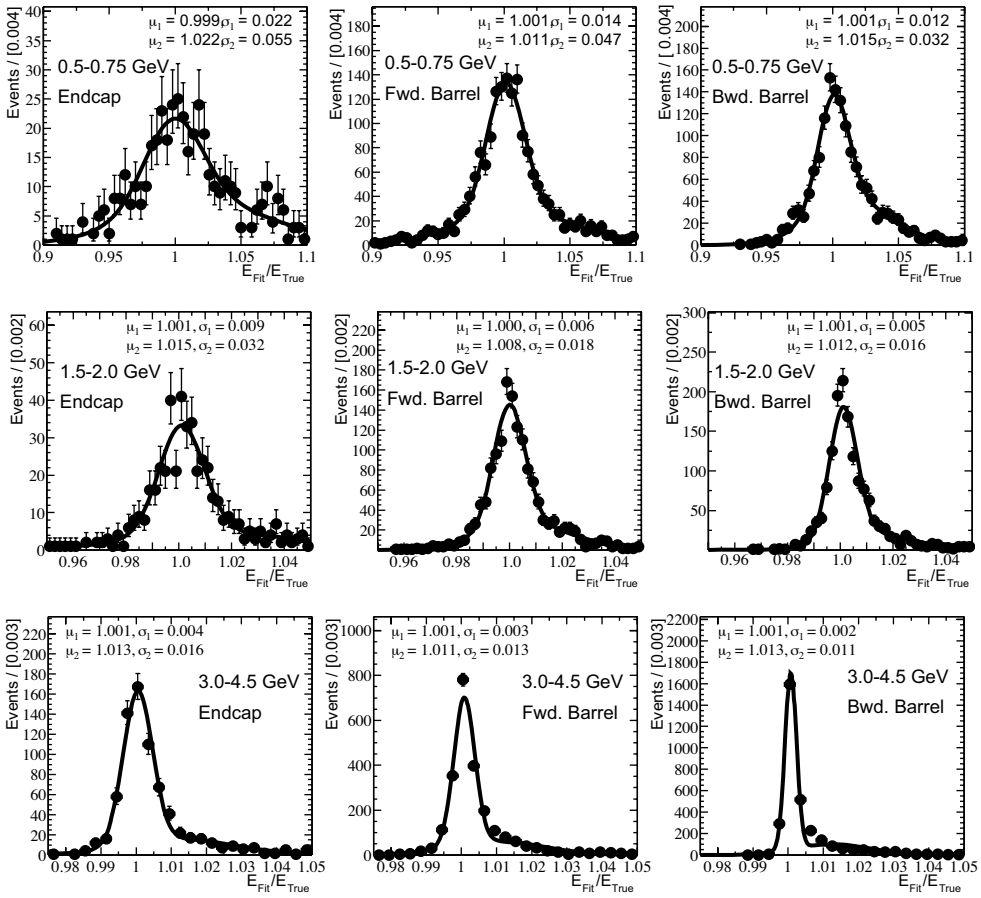

Figure 3.2: E_{Fit}/E_{True} in Monte Carlo-simulated radiative Bhabha events in three different regions of the detector and three different energies.

this bin. For this purpose, we use the "Crystal Ball" function:

$$f_{CB} = \{ \begin{array}{ll} \frac{x-\mu}{\sigma} > \alpha: & \exp -\frac{(x-\mu)^2}{2\sigma^2} \\ \frac{x-\mu}{\sigma} < \alpha: & A \times (B - \frac{x-\mu}{\sigma}^{-n}) \end{array} , \tag{3.3}$$

where:

$$\begin{array}{l} A \equiv \left(\frac{n}{\alpha}\right)^n \exp -\frac{1}{2}|\alpha|^2 \\ B \equiv \frac{n}{\alpha} - |\alpha| \end{array} \tag{3.4}$$

This distribution is a modified Gaussian distribution in which two additional parameters, α and β describe a transition to the tail described by a power function at some point in the Gaussian. The "cut" parameter α describes the position of this transition; a negative(positive) value places the transition on the lower(upper) side, and the β parameter describes the slope of the power function; a larger value indicates a more rapidly decreasing tail. A and B are defined to enforce continuity of the function and its first derivative at the transition.
The binning is determined by the empirically observed variations in the peak positions of the E_R/E_F distribution and the available statistics. In particular, there are some expected changes as a function of polar angle due to the varying amount of material in the detector. There are some unexpected variations associated with the differences in the electronics in the EMC. In particular, the detector is binned twofold in Φ due to two batches of preamplifiers with different shaping times which exhibit calibrations that are systematically different by up to a few percent. Another observed variation is the differing behavior of the high-gain preamplifiers in the back of the detector and the low-gain preamplifiers in the front. This difference is incorporated into the binning in Θ. The following binning scheme is chosen:

- Energy: 100 MeV bins from $0.3 - 1.0$ GeV, 200 MeV bins from $1.0 - 5.0$ GeV and one bin for $6.0 - 7.0$ GeV
- Θ: 21 bins, typically 2 or 3 Φ rings per bin.
- Φ: Two bins, $-2.0 < \Phi < 2.6$ radians, and the compliment, corresponding to the two areas with different preamplifier shaping times..

The fitted peak position of E_R/E_F as function of Θ for three energy ranges are shown in Figure 3.3 for the two Φ regions defined by the preamplifier batches. The corrections vary across the detector by up to 3%.

3.2.4 The Calibration

The radiative Bhabha events from the 2001 data consisting of $35.7\,\mathrm{fb}^{-1}$ of data are used for the calibration. The sample yields approximately 6 million events with

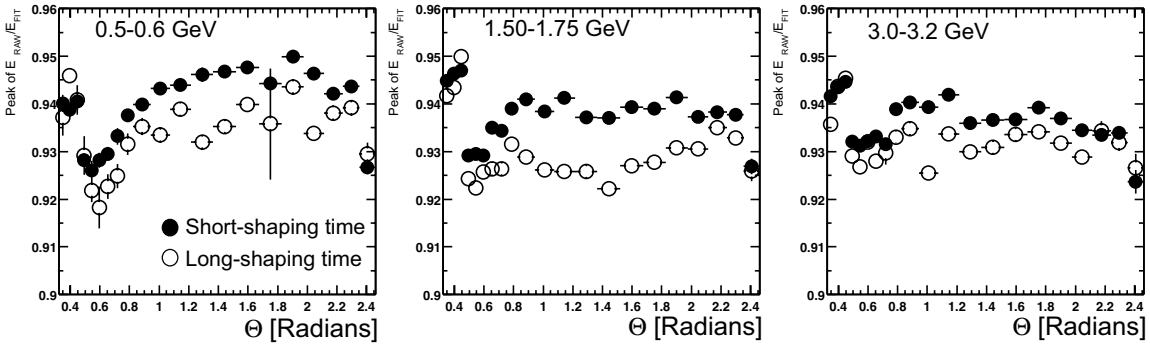

Figure 3.3: E_R/E_F peak positions versus Θ in three energy bins.

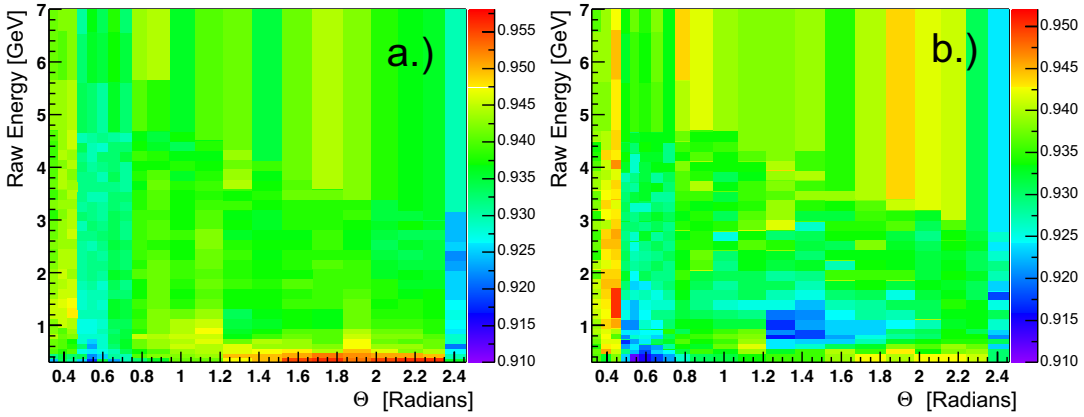

Figure 3.4: Energy correction as a function of raw energy and Θ. a.) long shaping time region. b.) short shaping time region.

successful kinematic fits which are used for the E_R/E_F distributions.

The E_R/E_F peak positions are linearly interpolated between the energy bins, but not in Θ. The result is a correction $C(E_F, \Theta, \Phi)$ that gives the expected E_R for a given fitted energy E_F and Θ in each of the two Φ regions. In practice, we are given E_R and wish to determine the true energy of the photon. This inversion is accomplished by a procedure that starts with $C(E_R, \Theta, \Phi)$. The predicted energy is then $E_{R2} = E_R/C(E_R, \Theta, \Phi)$. The correction is then recalculated with this new predicted energy and the procedure iterated until $E_{Ri+1} = E_{Ri}/C(E_{Ri}, \Theta, \Phi)$ within 0.1 MeV. The E_R correction determined this way is shown Figure 3.4 as a function

of Θ and E_R for the two Φ regions. The E_R is divided by the correction to determine the expected photon energy.

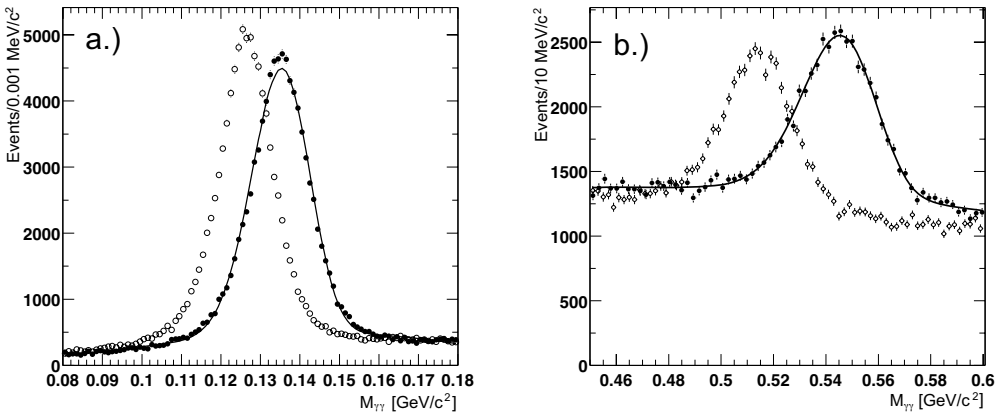

Figure 3.5: Mass spectrum of photons pairs in a.) symmetric π^0 decays and b.) symmetric η decays before and after calibration.

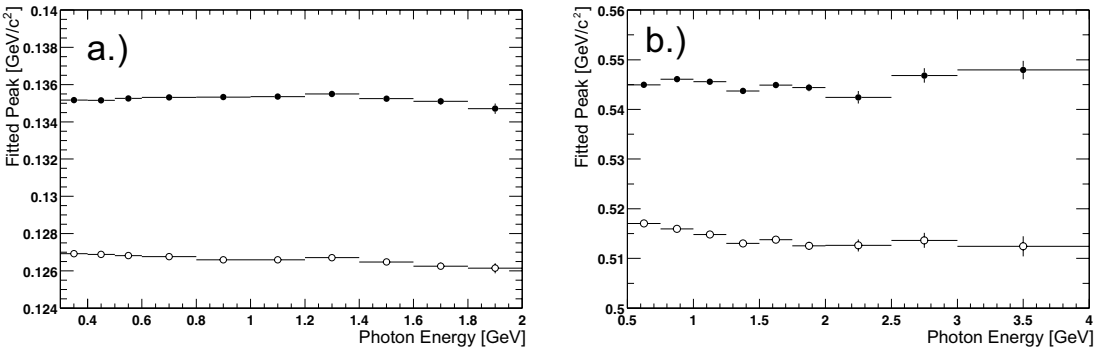

Figure 3.6: Peak of fitted mass distributions as a function of photon energy for symmetric a.) π^0 decays and b.) symmetric η decays before and after calibration.

3.3 Performance

The validation of the calibration is performed on a sample of symmetric π^0 and η decays in which both photons required to have energy within a certain range, thus isolating the EMC response to a photon of this energy. The mass spectrum of the photon pairs is fit to determine the peak position. The peak position is then compared with the measured values of $m_{\pi^0} = 0.13497\,\mathrm{GeV}/c^2$ and $m_\eta = 0.54230\,\mathrm{GeV}/c^2$ [36]. The reconstructed mass distribution for π^0 decays in which both photons have between 1.0 and 1.2 GeV of energy is shown in Figure 3.5 before and after the correction. The peak position is determined by a fit to a modified Gaussian distribution known as the "Novosibirsk" distribution:

$$dN/dm_{\mathrm{ES}} = A_S \exp\left[-0.5(\ln^2(1+\Lambda\tau(m_{\mathrm{ES}}-m_0))/\tau^2+\tau^2)\right] \tag{3.5}$$

where $\Lambda = \sinh(\tau\sqrt{\ln 4})/(\sigma\tau\sqrt{\ln 4})$, the peak position is m_0, the width is σ, and τ is the tail parameter. In the limit $\tau \to 0$, the Novosibirsk distribution reduces to the Gaussian. The combinatoric background is described by a third-order polynomial. Figure 3.5 also shows the same for η decays in which both photons have between 1.0 and 1.25 GeV of energy. The correction brings the peak position to the expected value. The peak positions determined in this manner are shown in Figure 3.6 as a function of photon energy for symmetric π^0 decays (left) and symmetric η decays (right), before and after the correction. The peak positions after the correction are within 0.5% of their expected values, validating the calibration up to 4 GeV in photon energy.

Chapter 4

The $B \to K^*\gamma$ Analysis

The $B \to K^*\gamma$ process is reconstructed in four decay modes of the $K^*(892)$ resonance: $K^{*0} \to K^+\pi^-$, $K^0\pi^0$ and $K^{*+} \to K^+\pi^0$, $K^0\pi^+$. Charged conjugate modes are implied throughout. The K^0 are reconstructed in the decay $K^0_S \to \pi^+\pi^-$ and the π^0 in the decay to two photons. The analysis was conducted on the 1999-2000 *BABAR* dataset of 20.7fb^{-1} of on-resonance data containing 22.7 million $B\overline{B}$ decays and 2.6fb^{-1} of off-resonance data. The expected signal properties are studied using a detailed detector simulation based on GEANT [30], while the off-resonance data are used to cross check Monte Carlo predictions for the dominant background coming from the $q\overline{q}$ continuum events. Numerous control samples in the data are used to evaluate and correct the detector performance predicted by the Monte Carlo simulation.

The branching fractions are obtained for each of the four modes and averaged separately for B^0 and B^+. The CP asymmetry A_{CP} (defined in Equation 1.23) is measured using the three self-tagging decay modes.

The CLEO collaboration has previously measured the branching fractions of $B \to K^*\gamma$, obtaining [31]:

$$\begin{aligned} \mathcal{B}[B^0 \to K^{*0}\gamma] &= 4.55^{+0.72}_{-0.68} \pm 0.34 \times 10^{-5} \\ \mathcal{B}[B^+ \to K^{*+}\gamma] &= 3.76^{+0.89}_{-0.83} \pm 0.28 \times 10^{-5} \\ A_{CP} &= 0.08 \pm 0.13 \pm 0.03 \end{aligned} \tag{4.1}$$

Mode	Branching fraction ($/10^{-5}$)	Expected Yield (Events)
$B^0 \to K^{*0}\gamma$, $K^{*0} \to K^+\pi^-$	2.77 ± 0.41	630 ± 94
$B^0 \to K^{*0}\gamma$, $K^{*0} \to K^0_S\pi^0$, $K^0_S \to \pi^+\pi^-$	0.46 ± 0.10	105 ± 16
$B^+ \to K^{*+}\gamma$, $K^{*+} \to K^+\pi^0$	1.39 ± 0.31	315 ± 47
$B^+ \to K^{*+}\gamma$, $K^{*+} \to K^0_S\pi^+$, $K^0_S \to \pi^+\pi^-$	0.94 ± 0.20	210 ± 31

Table 4.1: Expected number of $B \to K^*\gamma$ events produced in a dataset of 22.7×10^6 $B\overline{B}$ events assuming the branching ratio $\mathcal{B}[B \to K^*\gamma] = 4.2 \times 10^{-5}$.

The expected yields are tabulated in Table 4.1 for the modes under consideration assuming isospin symmetry and an average branching fraction of $\mathcal{B}[B \to K^*\gamma] = 4.2 \times 10^{-5}$.

The candidate selection criteria used in this analysis are determined by maximizing $S^2/(S+B)$, where S is the expected signal yield based on the average measured branching fraction from CLEO, and B is the expected background yield from the Monte Carlo simulation. This optimization produces the selection with the minimum expected relative statistical uncertainty on the yield. The optimal selection for each variable is determined by varying the selection, determining the expected signal and background yields with no other selection criteria applied, and calculating the $S^2/(S+B)$.

While the optimal selection for a given variable depends on the selection criteria that have already been applied on the other variables, in practice, we find that the simultaneous or iterative optimization of the variables produces similar results to the individual optimizations.

4.1 Global Event Selection

The analysis starts by identifying $B\overline{B}$ events with a high energy photon candidate. Generic $B\overline{B}$ decays are characterized by high multiplicity and isotropic decay structure in the center-of-mass system (CMS) resulting from the cascade of weak decays of the B mesons, which are slowly moving in this frame. This is different from the

background electromagnetic processes, which have low multiplicity (typically one or two tracks) and the continuum, which tend to have a more collimated decay structure from the hadronic jet production resulting from the fast recoil of the quark-antiquark pair. The selection of hadronic events begins by requiring at least three reconstructed tracks in the event. The track multiplicity of Monte Carlo-simulated signal and off-resonance background events is shown in Figure 4.1. The large fraction of events in the off-resonance data with two tracks are from electromagnetic processes such as Bhabha scattering. Next, we consider the event topology characterized by the ratio of second and zeroth Fox-Wolfram moments R_2 [34] shown in Figure 4.1 after the track multiplicity requirement. The peak in R_2 near one in the background distribution is from the remaining events from electromagnetic processes. These events are removed by requiring R_2 of the event be less than 0.9.

The signal process produces the photon in a two-body B decay. Since the B meson is slowly moving in the center-of-mass (CMS) frame, the photons are nearly mono-energetic in this frame with $E_\gamma^* \sim 2.5\,\mathrm{GeV}$. Hadronic events in which the most energetic photons has $1.5 < E_\gamma^* < 3.5\,\mathrm{GeV}$ are selected for further analysis.

The primary background in this analysis are high energy photons produced by energetic π^0 and η decays in the continuum. Prior to the suppression of this background as described in Section 4.2, this is the primary source of background. Initial state radiation (ISR), where a high-energy photon is radiated from the initial state electron or positron prior to interaction, is another source of background. After the suppression of the π^0 and η backgrounds, the ISR background contribution is approximately equal to the π^0 and η backgrounds. A study of Monte Carlo-simulated $B\overline{B}$ events indicates that there are no significant backgrounds apart from crossfeed between the $B \to K^*\gamma$ modes and downfeed from other $b \to s\gamma$ processes. The treatment of these backgrounds is described in Section 4.7.

The E_γ^* distributions for signal $B \to K^*\gamma$ and background events are shown in Figure 4.1 after the track multiplicity and R_2 selection. The spread in the signal E_γ^* distribution is dominated by the momentum of the B meson in the CMS frame of $325\,\mathrm{MeV}/c$, while the background distribution has a continuous falling distribution. The initial event selection reduces the hadronic event sample by more than a factor

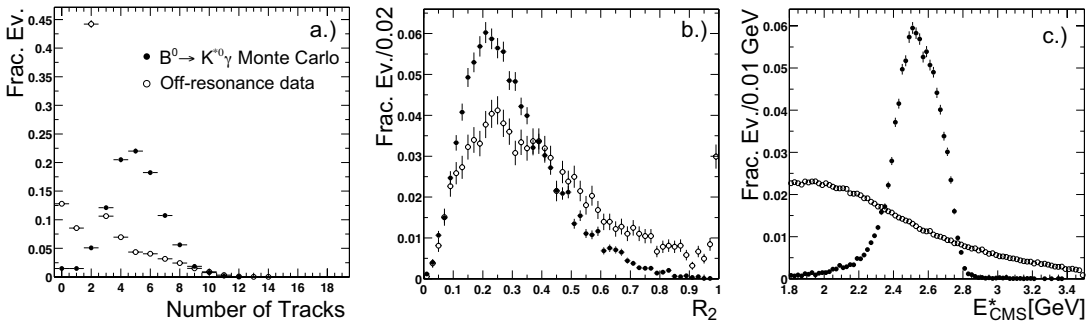

Figure 4.1: Variables used to select $B\overline{B}$ events with a high-energy photon. a.) Charged track multiplicity. b.) Second Fox-Wolfram Moment R_2. c.) Energy of the most energetic photon in the CMS frame. The distributions are normalized to unity.

of ten with nearly 80% efficiency for the signal process.

4.2 Photon Selection

4.2.1 Selection of Single Photon Candidates

A photon candidate is identified as a local energy maximum ("*bump*") within a contiguous cluster of crystals in the EMC that does not overlap any charged tracks [28]. In this analysis, we further require that the photon is isolated from any other local maxima in the EMC by at least 25 cm. This suppresses contributions from hadronic interactions, which may produce multiple local maxima within close proximity. In order to ensure that the photon candidate is not associated with a charge track, we limit the polar acceptance to $-0.74 < \cos\Theta_\gamma < 0.93$ as shown in Figure 4.2; outside of this range, the tracking coverage is limited by the acceptance of the SVT and DCH. The photon must also not contain any crystal readout channels identified as problematic, dead, or noisy by the online monitoring. Occasionally, the monitoring may miss noisy channels. In this case, the EMC cluster will typically contain only one or a few crystals. These are eliminated by requiring that the cluster contain more than four crystals.

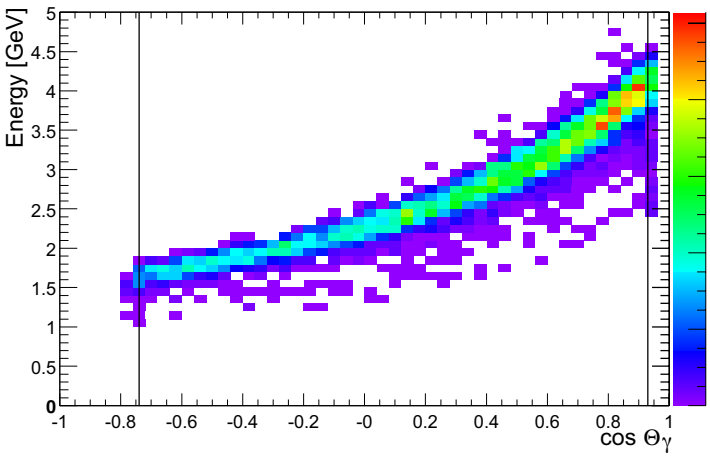

Figure 4.2: Lab frame kinematics of primary photon in $B \to K^*\gamma$: E_{lab} vs. $\cos\Theta_\gamma$. The lines indicate the acceptance used in this analysis.

4.2.2 π^0 and η Veto

Photons from π^0 production are suppressed by removing photon candidates that form an invariant mass within $25\,\mathrm{MeV}/c^2$ of the π^0 mass when paired with any other photon in the event with energy greater than 50 MeV. A similar veto is imposed on photon candidates that form pairs within $40\,\mathrm{MeV}/c^2$ of the η mass with photons with energy greater than 250 MeV. The π^0 and η vetoes are shown in Figure 4.3, where the invariant mass combination closest to the π^0 or η peak are shown for the photon candidates. A clear peak corresponding to π^0 and η production can be seen in the continuum Monte Carlo simulation that is not present in the signal.

At energies above 3 GeV, the decay photons may be sufficiently collimated that the reconstruction cannot distinguish the two photons as two local maxima. Such candidates ("*merged* π^0"), however, have wider lateral energy deposition profile which can be characterized by the *second moment* L_2:

$$L_2 = \sum_{\text{crystals } i} \frac{E_i\left[(\theta_i - \theta_c)^2 + (\phi_i - \phi_c)^2\right]}{\sum_i E_i} \tag{4.2}$$

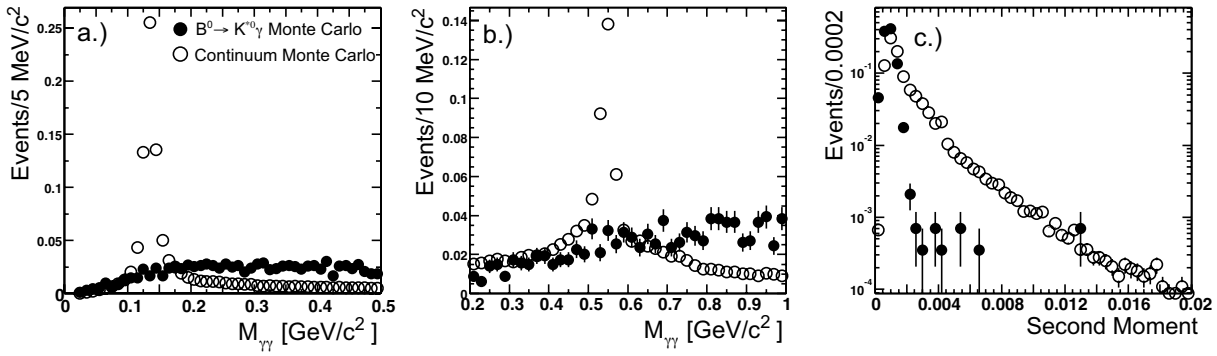

Figure 4.3: π^0 and η suppression. a.) Invariant mass combination closest to the π^0 mass. b.) Same for the η. c.) Second moment distribution. The distributions are normalized to unity.

where $\theta_c,\ \phi_c$ are angular coordinates of the centroid maxima, and $E_i,\ \theta_i,\ \phi_i$ are the energy and coordinates of the ith crystal in the bump. True single photons bumps have smaller second moment than the merged photons from π^0 decays. This contamination is reduced by requiring $L_2 < 0.002$. Single legs of π^0 and η decays where the partner photon is not reconstructed and photons from initial state radiation are irreducible by these means.

The second moment distribution for signal and background is shown in Figure 4.3. The background has a long tail towards large values of L_2 corresponding to the merged π^0s and hadronic interactions from neutrons and K_L^0 in the EMC.

4.3 K^* Reconstruction

The K^* candidates are reconstructed from their daughter particles: charged kaons and pions, K_S^0, and π^0. The appropriate kaon and pion candidates are combined to make the K^* candidates for each decay mode.

4.3.1 Track reconstruction

The track requirements for the K^* reconstruction are divided between two categories: one for "prompt" tracks which are produced at the B decay vertex, and one for K_S^0

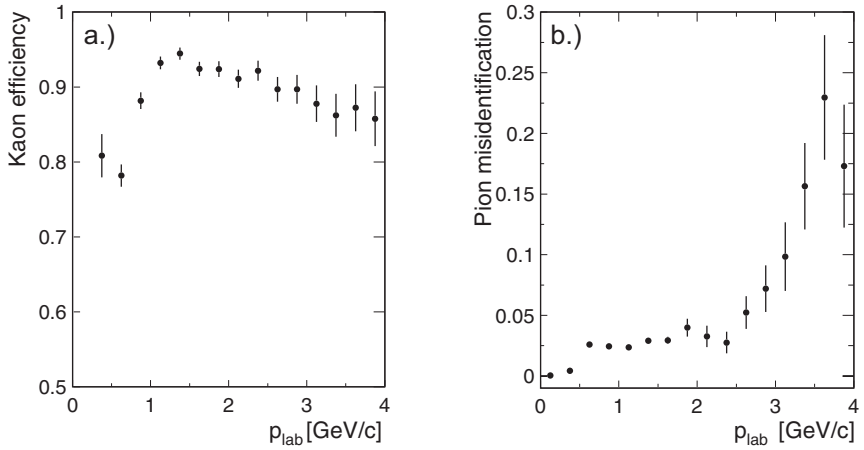

Figure 4.4: a.) Kaon efficiency and b.) pion misidentification rates for tracks in the DIRC acceptance measured from the D^{*+} control sample.

tracks, where the tracks may be produced far from the B decay vertex. In the first case, we require the track to

- Contain at least 12 DCH hits
- Pass close to the interaction point: $|z_0| < 10$ cm and $|d_0| < 1.5$ cm. z_0 is the z position of the track at its closest approach to the detector origin, and d_0 is the transverse distance from the origin at this point.
- Have significant transverse momentum: $p_T > 0.1\,\mathrm{GeV}/c$
- Have non-zero fit χ^2 probability.

This track selection is used for both tracks in the decay $K^{*0} \to K^+\pi^-$, the kaon in $K^{*+} \to K^+\pi^0$ and the primary pion in $K^{*+} \to K^0\pi^+$. For the $K^0_S \to \pi^+\pi^-$ tracks, we use a looser criterion that does not require that the track come from the interaction point, and drop the p_T and DCH hit requirements.

4.3.2 Particle Identification

The charged particle identification information obtained from dE/dx measurements in the SVT and DCH and Cherenkov ring information from the DIRC is used to

identify charged kaons. Charged kaon candidates are selected using a likelihood ratio formed from dE/dx information at low momenta ($< 0.7\,\mathrm{GeV}/c$), and the DIRC reconstruction at momenta well above the kaon Cherenkov threshold ($> 0.6\,\mathrm{GeV}/c$) [44]. The DIRC likelihood is a product of two components: a Gaussian probability describes the likelihood of the reconstructed Cherenkov angle with the expected angle based on the track trajectory through the DIRC, and a Poisson likelihood describes the consistency of the observed number of photons in the ring. The likelihood fit determines the number of signal and background photons in the ring, from which a Poisson probability is calculated based on the expected number of signal photons derived from the Monte Carlo simulation. The likelihood is calculated for the pion, kaon and proton hypothesis and a selection on the ratio of the likelihoods is tuned to obtain the desired properties for the selector. In this analysis, the "tight" kaon selection is designed to maintain a pion misidentification rate of less than 5% up to a momentum of $3\,\mathrm{GeV}/c$. Protons are rejected with a selection on the ratio of kaon and proton likelihoods. The charged pion candidates in the $K^{*0} \to K^+\pi^-$ decay are chosen from tracks rejected by the kaon selection.
The performance of the kaon selector is shown in Figure 4.4 for a sample of kaons and pions in the DIRC acceptance obtained from $D^{*+} \to D^0\pi^+$, $D^0 \to K^+\pi^-$ decays in the data. Most kaons in the $B \to K^*\gamma$ decay have momenta between $1-3\,\mathrm{GeV}/c$, where the selector efficiency is $\sim 90\%$ with pion misidentification rates of $2-3\%$.

4.3.3 K^0_S Reconstruction

The $K^0_S \to \pi^+\pi^-$ reconstruction fits a common vertex for pairs of oppositely charged tracks with invariant mass $300 < M_{\pi^+\pi^-} < 700\,\mathrm{MeV}/c^2$ calculated using the helical track parameters at the origin. The algorithm calculates the point of closest approach of the two tracks based on their trajectories and determines the most likely point of origin by minimizing the χ^2 based on the track covariance matrix. From its lifetime ($\tau_{K^0_S} = 0.894 \times 10^{-10}\,\mathrm{s}$, $c\tau = 2.68$ cm [36]), we expect the K^0_S to traverse an appreciable distance from the production point before decaying. As a result the track parameters may be significantly different at the decay vertex from those obtained at

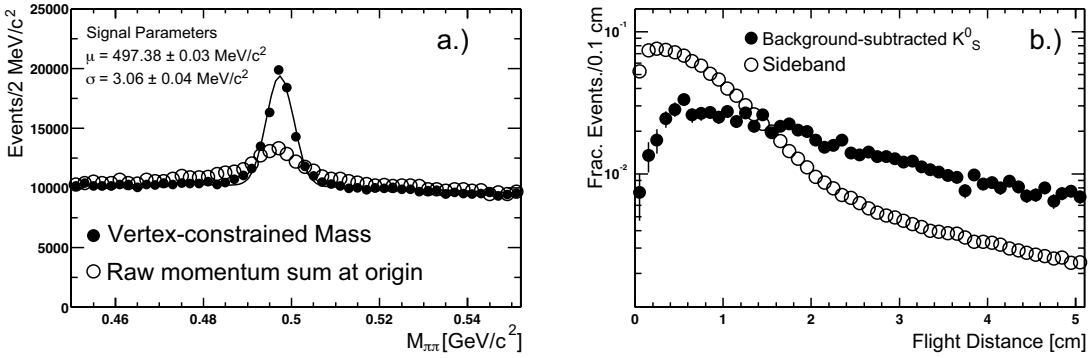

Figure 4.5: The K_S^0 reconstruction. a.) Raw and vertex-constrained $M_{\pi^+\pi^-}$ and b.) Vertex flight distance in off-resonance data.

the origin. The track momenta are reevaluated at the calculated vertex, resulting in significant improvement in the mass resolution.

With the calculated vertex and mass, we select K_S^0 candidates that are displaced by at least 0.2 cm from the beam spot and with $489 < M_{\pi^+\pi^-} < 507\,\mathrm{MeV}/c^2$. The reconstruction is demonstrated in Figure 4.5, which shows the $\pi^+\pi^-$ invariant mass distribution before and after the vertex-constrained fit, as well as the vertex displacement for the same events outside the signal $M_{\pi^+\pi^-}$ region and within the signal region with the background subtracted.

4.3.4 π^0 Reconstruction

The π^0 are reconstructed from their decay $\pi^0 \to \gamma\gamma$. The photon candidates for the π^0 reconstruction are required to have at least 30 MeV of energy. Pairs of selected photons with invariant mass $0.115 < m_{\gamma\gamma} < 0.150\,\mathrm{MeV}/c^2$ (approximately twice the resolution of $\sim 7\,\mathrm{MeV}/c^2$) are fit with the mass constrained to the nominal π^0 mass ($m_{\pi^0} = 134.98\,\mathrm{MeV}/c^2$) to re-determine their momenta. The π^0 reconstruction is illustrated in Figure 4.6, where the invariant mass peak from π^0 decays is fit to the Novosibirsk function and the combinatoric background described by a polynomial.

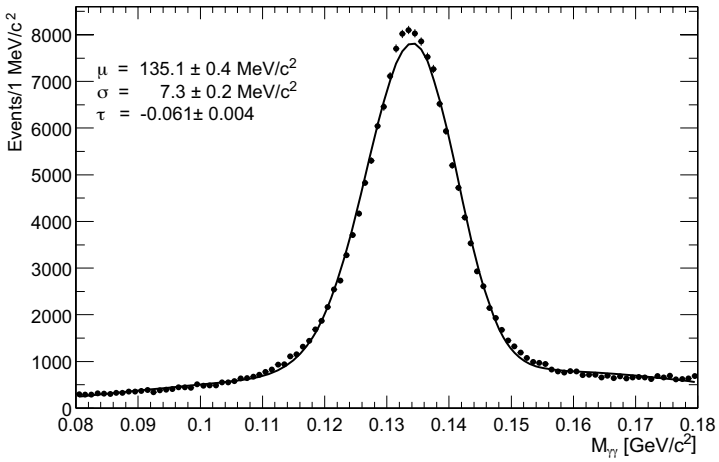

Figure 4.6: Invariant mass distribution of photon pairs in hadronic events.

4.3.5 Selection of K^* Candidates

The four K^* decay modes we consider, $K^{*0} \to K^+\pi^-$, $K^0_S\pi^0$, and $K^{*+} \to K^+\pi^0$, $K^0_S\pi^+$ are reconstructed from the appropriate kaon and pion daughters candidates described above. Candidates with invariant mass $m_{K\pi}$ within $100\,\mathrm{MeV}/c^2$ of the nominal K^* mass ($M_{K^{*0}} = 896\,\mathrm{MeV}/c^2$ and $M_{K^{*+}} = 892\,\mathrm{MeV}/c^2$) and center-of-mass momentum between $2.35 < p^*_{K^*} < 2.8\,\mathrm{GeV}/c$ are selected.

4.4 Reconstruction of the B Candidate

The B candidate is reconstructed by combining the kinematic information from the photon and K^* candidate. We define two variables in the center-of-mass (CMS) frame which are uncorrelated for the signal process:

$$\begin{aligned} m_{\mathrm{ES}} &= \sqrt{E^{*2}_{beam} - p^{*2}_B} \\ \Delta E^* &= E^*_B - E^*_{beam} \end{aligned} \tag{4.3}$$

where p^*_B and E^*_B are the energy and momentum of the B candidate reconstructed by the detector. The two variables determine whether the mass and energy of the B candidate are consistent with the B meson ($m_{\mathrm{ES}} = M_B$) and the beam energy

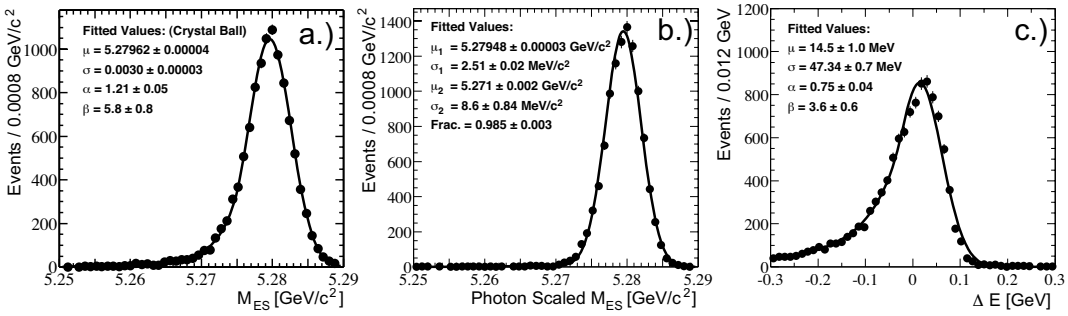

Figure 4.7: Kinematic variables in the $B \to K^*\gamma$ reconstruction. a.) $m_{\rm ES}$ without photon scaling, b.) $m_{\rm ES}$ with photon scaling and c.) ΔE^*.

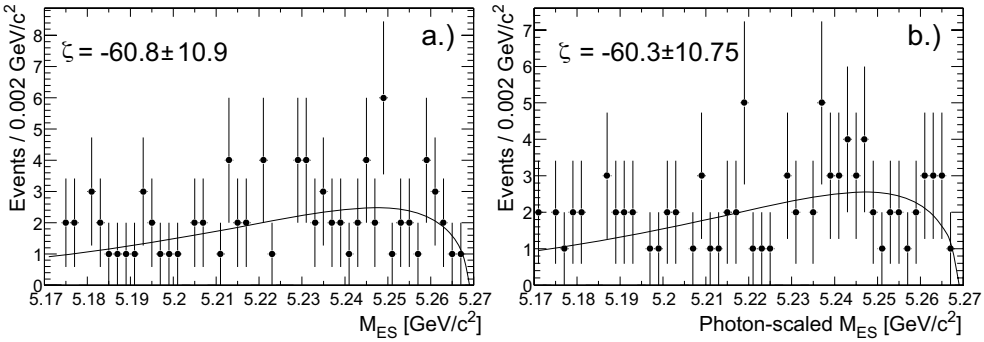

Figure 4.8: $m_{\rm ES}$ for the background $B^0 \to K^{*0}\gamma$, $K^{*0} \to K^+\pi^-$ candidates in off-resonance data: a.) $m_{\rm ES}$ without photon scaling, b.) $m_{\rm ES}$ with photon scaling.

($\Delta E^* = 0$). The beam energy has a spread of 2 MeV in the CMS frame and is more precisely known than any of the kinematic quantities reconstructed in the detector. For the modes in which the K^* final state particles are all charged ($K^{*0} \to K^+\pi^-$ and $K^{*+} \to K^0_S\pi^+$), rather than scaling only the energy of the B candidate to the beam energy, we scale the photon energy individually to the value that would make $\Delta E^* = 0$. Both the energy and momentum of the B candidate are modified according to the new photon momentum. The scaling of the photon individually is motivated by the experimental resolution: the photon momentum resolution is considerably worse than that of the tracks reconstructed in the DCH. This modified $m_{\rm ES}$ reduces the width of the signal $m_{\rm ES}$ distribution from 3.0 MeV/c^2 to 2.5 MeV/c^2 as shown in Figure 4.7. The $m_{\rm ES}$ distribution with this modification is described well by the

Gaussian distribution centered at $m_{\rm ES} = M_B$. The background distributions for the $m_{\rm ES}$ with and without rescaling are shown in Figure 4.8. The background shape is not distorted by the photon rescaling, as indicated by the consistent ζ parameters obtained from the ARGUS parameterizations (described in Section 4.7) of the two distributions.

For the modes $K^{*0} \to K^0_S\pi^0$ and $K^{*+} \to K^+\pi^0$, the $m_{\rm ES}$ distribution is asymmetric due to the energy leakage in the reconstruction of the primary photon and the π^0. The expected asymmetry in the $m_{\rm ES}$ distribution is described by the Novosibirsk function (Equation 3.5).

The signal ΔE^* distribution in all four modes is described by the "Crystal Ball" function (Equation 3.3). The ΔE^* distribution for the $K^{*0} \to K^+\pi^-$ mode is shown on the right in Figure 4.7.

We select candidates with $|\Delta E^*| < 500\,\text{MeV}$ and $m_{\rm ES} > 5.2\,\text{GeV}/c^2$. The expected distribution of signal and continuum background events in the off-resonance data are shown in Figure 4.9. Signal and sideband regions in ΔE^* for each mode are shown in Table 4.2, the differences resulting from the different signal ΔE^* resolutions for modes with and without a π^0 in the final state. Due to the asymmetric distribution of ΔE^* for the signal, which results in signal events populating the ΔE^* region below the signal region, only the upper sideband in ΔE^* in the on-resonance data is used in the signal extraction to obtain a sample of events populated exclusively by the continuum background. Candidates in the off-resonance data are also selected as a background control sample with $m_{\rm ES}$ rescaled with the average on-resonance beam energy of $E^*_{beam} = 5.29\,\text{GeV}/c^2$ to match them with the on-resonance data.

4.5 Event Shape Criteria

The differences in event topology between the continuum background and the signal $B \to K^*\gamma$ can be quantified by a number of variables. For this analysis, we choose:

1. $\cos\Theta^*_T$: the angle between the photon momentum in the CMS frame and thrust axis of the event excluding the B candidate.

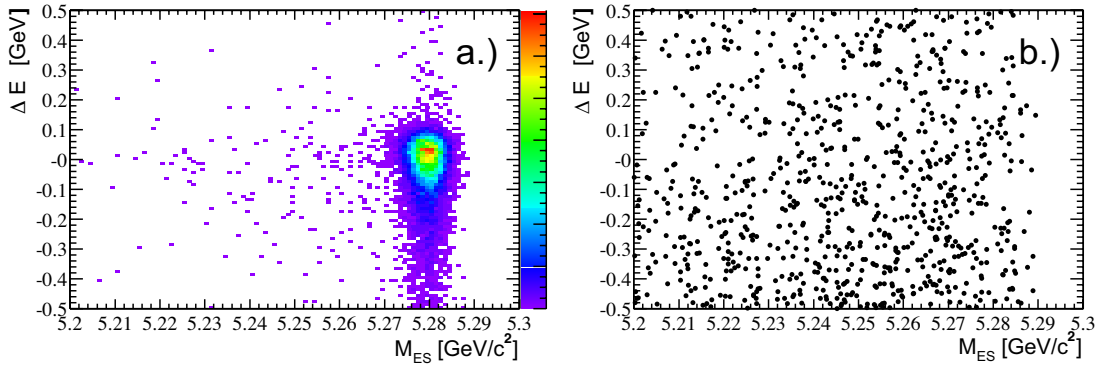

Figure 4.9: ΔE^* vs. $m_{\rm ES}$ distribution for a.) $B^0 \to K^{*0}\gamma$, $K^* \to K^+\pi^-$ signal Monte Carlo and b.) continuum background in the off-resonance data.

Mode	Signal GeV	Upper ΔE^* Sideband GeV	Off-resonance data GeV
$K^+\pi^-$	[-0.200, 0.100]	[0.100, 0.500]	[-0.300, 0.300]
$K^0_S\pi^0$	[-0.225, 0.125]	[0.150, 0.400]	[-0.300, 0.300]
$K^0_S\pi^+$	[-0.200, 0.100]	[0.100, 0.500]	[-0.300, 0.300]
$K^+\pi^0$	[-0.225, 0.125]	[0.150, 0.400]	[-0.300, 0.300]

Table 4.2: Signal and sideband regions in ΔE^* for selected candidates with $m_{\rm ES} > 5.2\,{\rm GeV}/c^2$.

2. $\cos\Theta^*_B$: The polar angle of the B candidate momentum in the center-of-mass.

3. $\cos\Theta_H$: The helicity angle of the K^* decay.

4.5.1 $\cos\Theta^*_T$

The background from the continuum is the result of energetic π^0 and η decays that produce high energy photons. Since these particles are produced in hadronic jets, they are correlated with the jet axis of the event in the CMS frame. Figure 4.10 shows the expected event topologies for the more spherical signal process and the jet-like background continuum background.

For the signal $B \to K^*\gamma$ process, the decay axis of the B candidate is uncorrelated

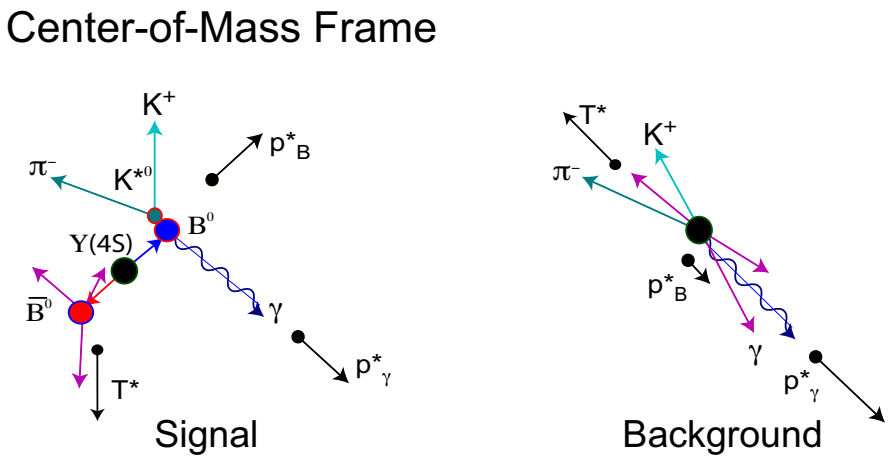

Figure 4.10: Comparison of the expected topology of signal $B \to K^*\gamma$ decays and background continuum.

with the decay axis of the other B-meson. The result is that the angle in the CMS frame between the photon momentum and the jet axis of the rest of the event (decay axis of the other B) are uncorrelated due to the fact that the B mesons are nearly at rest in this frame. The jet/decay axis is reconstructed by calculating the thrust axis $\mathbf{T}$ of the event, defined as the direction that maximizes the quantity:

$$|T| = \frac{\sum_i \left|\mathbf{T} \cdot \vec{p_i^*}\right|}{\sum_i |\vec{p_i}|} \tag{4.4}$$

.

where $\vec{p_i^*}$ are the CMS frame momenta of the reconstructed particles in the event not associated with the B candidate. For this purpose, we use all reconstructed charged tracks and photons with energy greater than 30 MeV. The variable Θ_T^* is then defined as the angle between the thrust axis and the photon momentum in the CMS. The $\cos\Theta_T^*$ distribution for the Monte Carlo-simulated signal candidates and background events from the off-resonance data are shown on the left in Figure 4.11. The signal distribution is flat, indicating that the photon momentum is uncorrelated with the decay axis of the other B meson, whereas for the background, the $|\cos\Theta_T^*|$ distribution peaks towards one, consistent with production along the jet axis.

4.5.2 $\cos\Theta_B^*$

The $B\overline{B}$ mesons emerge from the decay of the $\Upsilon(4S)$ in a P-wave state; thus the decay axis of the $B\overline{B}$ pair follows a $\sin^2\Theta$ distribution in the polar angle Θ. Since the CMS momentum p_B^* of the B meson coincides with the axis of the $\Upsilon(4S)$ decay, we expect Θ_B^*, the polar momentum of p_B^*, to have the same distribution. For the continuum background, the B candidate consists of combinations of oppositely charged tracks with a photon candidate; this should have a distribution flat in $\cos\Theta_B^*$. The reconstruction of $\cos\Theta_B^*$ for Monte Carlo signal events and off-resonance data is shown in the center of Figure 4.11.

4.5.3 $\cos\Theta_H$

For the signal $B \to K^*\gamma$, angular momentum conservation and transverse polarization of the photon dictate that the K^* must be in a transversely polarized $J = 1$ state. The polarization of the K^* can be observed from the helicity angle Θ_H distribution of the decay, which is $\sin^2\Theta_H$. The helicity angle is reconstructed from the angle between the direction of the kaon candidate in the rest frame of the K^* candidate and the momentum of the K^* in the B candidate rest frame.
For continuum background, the $K\pi$ combinations are not polarized, though they may come from K^* production. The helicity distribution for signal and continuum background are shown on the right in Figure 4.11.

4.5.4 Event Shape selection

The $S^2/(S+B)$ optimizations for the event shape criteria result in similar requirements for the four K^* modes. This leads to a common selection of:

$$|\cos\Theta_T^*| < 0.8 \qquad |\cos\Theta_B^*| < 0.8 \qquad |\cos\Theta_H| < 0.75 \tag{4.5}$$

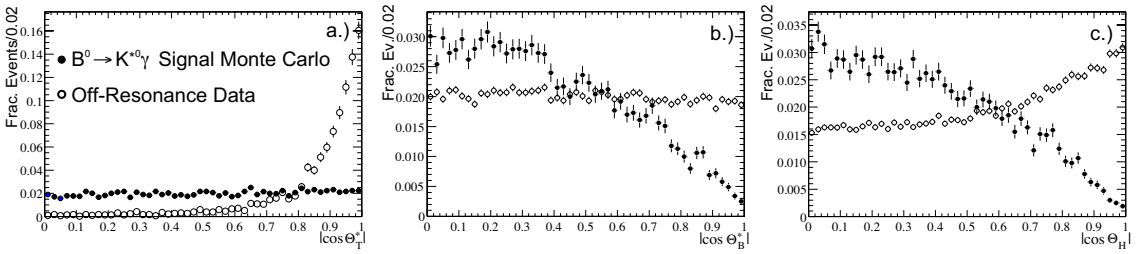

Figure 4.11: Event Shape Variables a.) $\cos\Theta_T^*$, b.) $\cos\Theta_B^*$ and c.) $\cos\Theta_H$.

4.6 Efficiencies and Systematic Corrections

The efficiencies for the signal reconstruction and selection obtained from exclusive Monte Carlo simulation of each decay mode of the K^* under consideration are shown in Table 4.3, along with empirically determined corrections for the track and photon reconstruction efficiencies. The charged track efficiencies include the efficiency for track reconstruction and particle identification criteria. The K_S^0 and π^0 efficiencies involve the reconstruction of both daughter particles and the selection of the composite candidates for the reconstruction of the K^* candidates. The K^* reconstruction efficiency includes the $M_{K\pi}$ and CMS frame momentum selection. The B candidate efficiency is the fraction of reconstructed candidates which lie in the ΔE^* signal band, where the candidate with smallest $|\Delta E^*|$ is selected in the case there are multiple candidates satisfying the all of the selection criteria. In some cases, a combination of tracks and photons is selected that does not actually correspond to the signal decay process. When these events are added, the efficiency in the last row results.

4.6.1 Photon and π^0 Efficiency Correction

A sample of $e^+e^- \to \tau^+\tau^-$ decays were studied to determine the photon reconstruction efficiency in the data relative to the Monte Carlo simulation. The study is documented in Reference [41]. The method utilizes the well-known ratio $\mathcal{B}[\tau \to h^-\pi^0\pi^0\nu_\tau]/\mathcal{B}[\tau \to h^-\pi^0\nu_\tau] = 0.355 \pm 0.006$ [36], [37], where $h^- = \pi^-/K^-$. An event

selection for $\tau^+\tau^-$ decays involving a charged lepton from one τ decay and significant missing momentum pointing within the acceptance of the detector is sufficient to extract this sample. The advantage of this method is that the uncertainties in the event selection from the track reconstruction and lepton selection largely cancel. A comparison of the ratio in data and the Monte Carlo simulation then gives the relative efficiency for reconstructing the second π^0, which can be translated into a correction for the Monte Carlo photon finding efficiency.

The result of this study is that the observed branching ratio in data is $6.1 \pm 1.1\%$ lower in data than in the Monte Carlo simulation; the number of reconstructed τ decays with two π^0s relative to those with π^0 is smaller than expected from the known ratio of branching fractions and the detector simulation. At energies below 3.5 GeV, this is believed to be the result of the incorrect simulation of material in front of the EMC, particularly in the forward region. At π^0 energies greater than 3.5 GeV, the deficit is likely due to discrepancies in the shower simulation which result in higher efficiency for identifying two contiguous bumps in a single cluster, the typical topology for high energy π^0 decays. As a result, the Monte Carlo efficiency for finding each photon in the event is reduced by $2.5\% \pm 1.3\%$. The error is dominated by the statistical uncertainty in the CLEO measurement of the branching ratio [37] and the different levels of occupancy for $e^+e^- \to \tau^+\tau^-$ decays and hadronic decays which may change the efficiency in *BABAR*.

4.6.2 Tracking Efficiency Correction

The Monte Carlo efficiency for track reconstruction and the quality requirements described in Section 4.3.1 are cross-checked using data control samples. The standalone tracking capability of the SVT allows tracks to be reconstructed independently of DCH information. The efficiency for the DCH reconstruction and quality requirements can then be calculated in data and Monte Carlo simulation to determine a correction. For this purpose, three-prong decays of the τ and $D^{*+} \to D^0\pi^+$ decays with four prong D^0 decays are reconstructed requiring all tracks save one to satisfy the track requirements [38]. The efficiency is then obtained by requiring the final

	$K^+\pi^-$	$K^0_S\pi^0$	$K^+\pi^0$	$K^0_S\pi^+$
Selection		Efficiency(%)		
Global Event	78.1	78.9	77.4	77.5
Photon Selection	70.4	71.0	71.1	68.6
Charged Kaon	78.0		72.7	
Charged Pion	88.6			85.4
K^0_S Reconstruction		62.9		60.5
π^0 Reconstruction		51.8	53.6	
K^* Selection	81.0	84.1	83.5	79.8
Event Shape Selection	73.7	71.8	71.6	75.5
B selection	96.2	96.1	96.6	95.4
Photon Correction	97.5	97.5	97.5	97.5
π^0 Correction		95.0	95.0	
Charged track correction	97.7		99.4	98.9
K^0_S correction		104.2		103.0
Truth-matched Cumulative	21.0	11.3	11.3	15.9
Cumulative	21.0	12.6	12.9	17.2

Table 4.3: Signal reconstruction efficiency from the $B \to K^*\gamma$ Monte Carlo simulation with empirical corrections derived from Monte Carlo-data comparisons.

track to satisfy the track requirements. The results are tabulated into an efficiency correction binned by momentum, polar angle, azimuthal angle, and overall event multiplicity. An average track correction is obtained in the signal Monte Carlo simulation by applying the corrections on a track-by-track basis. The correction suggests that the track reconstruction is somewhat less efficient in the data relative to the Monte Carlo simulation.

A separate systematic correction for the K^0_S reconstruction efficiency, which has less stringent track quality requirements, is obtained from the inclusive K^0_S decays[45]. The yield of K^0_S normalized by luminosity is compared between the Monte Carlo simulation of the continuum and inclusive $B\overline{B}$ decays and the on- and off-resonance data. A correction is determined for the reconstruction efficiency in bins of momentum and flight distance and applied event-by-event in the signal Monte Carlo simulation for the reconstructed K^0_S in the simulation to determine an average correction.

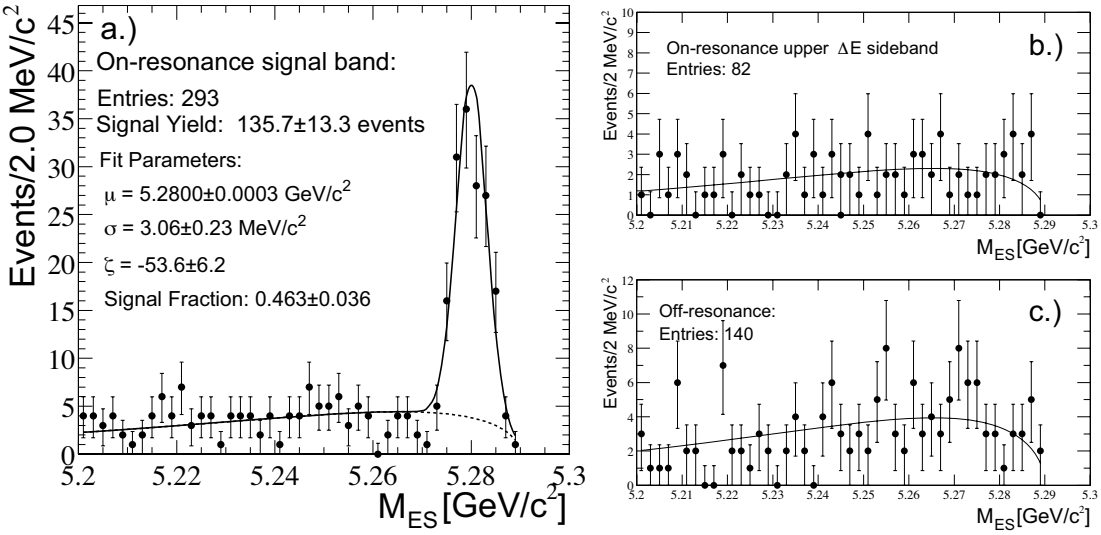

Figure 4.12: Results of the simultaneous extended maximum likelihood fit for the $B^0 \to K^{*0}\gamma$, $K^{*0} \to K^+\pi^-$ mode in a.) signal band $-200\,\mathrm{MeV} < \Delta E^* < 100\,\mathrm{MeV}$, b.) upper ΔE^* sideband from on-resonance data and c.) off-resonance data.

4.7 Signal Extraction

The signal for each $B \to K^*\gamma$ mode is separately extracted by an extended maximum-likelihood fit in the m_{ES} distribution for each final state. The signal probability distribution function is described by a Gaussian distribution centered at $m_{\mathrm{ES}} = M_B$ for the modes $K^{*0} \to K^+\pi^-$ and $K^{*+} \to K^0_S\pi^+$. The modes $K^{*0} \to K^0_S\pi^0$ and $K^{*+} \to K^+\pi^0$ are described by the Novosibirsk distribution (Equation 3.5). The width and peak of the Gaussian and Novosibirsk are free parameters in the maximum likelihood fit for the modes $K^{*0} \to K^+\pi^-$ and $K^{*+} \to K^+\pi^0$, where the number of expected signal events is larger. For the other two modes, the width is fixed to the Monte Carlo value with an empirically determined correction obtained from the observed width of the $K^{*0} \to K^+\pi^-$ mode ($3.1 \pm 0.2\,\mathrm{MeV}/c^2$), which is wider than the Monte Carlo expectation of $2.5\,\mathrm{MeV}/c^2$. The discrepancy may due to a wider beam-energy spread in the data than in the Monte Carlo simulation. This difference is added quadratically to the Monte Carlo expectation for the m_{ES} resolution in $K^{*0} \to K^0_S\pi^0$ and $K^{*+} \to K^+\pi^0$. The tail parameter for the Novosibirsk is fixed

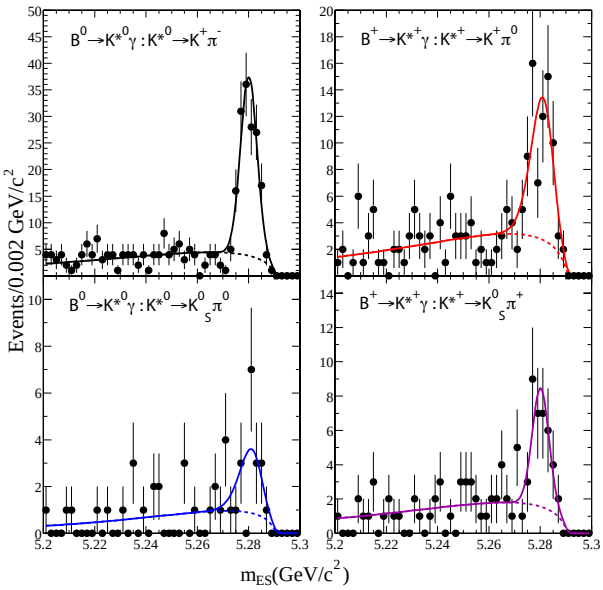

Figure 4.13: Fitted $m_{\rm ES}$ distributions for $B \to K^*\gamma$ candidates in on-resonance data.

to the Monte Carlo expectations. The signal $m_{\rm ES}$ parameters are summarized in Table 4.4.

The continuum background is described by the "ARGUS" threshold shape [42]:

$$dN/dm_{\rm ES} = A_B \frac{m_{\rm ES}}{E^*_{beam}} \sqrt{1 - \frac{{m_{\rm ES}}^2}{E^{*2}_{beam}}} \exp\left[\zeta\left(1 - \frac{{m_{\rm ES}}^2}{E^{*2}_{beam}}\right)\right], \tag{4.6}$$

The ARGUS shape describes the expected $m_{\rm ES}$ distribution resulting from the phase space of random combinations of photon and K^* candidates near the endpoint of the $m_{\rm ES}$ distribution at $m_{\rm ES} = E^*_{beam}$. The empirically determined parameter ζ describes the turnover of the rise in phase space away from the endpoint.

4.7.1 CP-Averaged Yield Extraction

The fit for each mode is performed simultaneously over three samples: the signal band in ΔE^*, where the fit has both a signal and background component, the upper

Mode	Shape	MC σ	Fixed σ	Fixed τ
$K^{*0} \to K^+\pi^-$	Gaussian	$2.51\,\mathrm{MeV}/c^2$	N.A.	N.A.
$K^{*0} \to K^0_S\pi^0$	Novosibirsk	$3.52\,\mathrm{MeV}/c^2$	$4.19 \pm 0.66\,\mathrm{MeV}/c^2$	-0.17 (0)
$K^{*+} \to K^+\pi^0$	Novosibirsk	$3.44\,\mathrm{MeV}/c^2$	N.A.	-0.15 (0.17)
$K^{*+} \to K^0_S\pi^+$	Gaussian	$2.54\,\mathrm{MeV}/c^2$	$3.08 \pm 0.23\,\mathrm{MeV}/c^2$	N.A.

Table 4.4: Signal m_{ES} probability distributions.

sideband in ΔE^* above the signal region, and the off-resonance data, as described in Table 4.2 for each mode. The latter two are fit with only the background component under the assumption that they are populated entirely by the continuum background. For the off-resonance data in the $K^{*0} \to K^+\pi^-$ and $K^{*+} \to K^+\pi^0$, the kaon identification requirement is removed to bolster the statistics.

The fit determines a common ζ parameter of the ARGUS function for both the control samples and the signal band and extracts a signal yield in the signal band by maximizing the overall extended likelihood:

$$\mathcal{L} = \frac{\exp(-\sum_j n_j)}{N!} \prod_{i=1}^{N} \sum_{j=1}^{m} n_j P_j(\alpha_j) \tag{4.7}$$

where the n_j are the number of events for each hypothesis (signal, background) and P_j is the total probability for each of these hypotheses. The total probability is a function of the vector of parameters α_j which describe the probability distribution of each hypothesis. The product runs over the N events of the sample. The n_j and α_j are the parameters that are determined by the fit. The results of the fit for the $K^{*0} \to K^+\pi^-$ mode are shown in Figure 4.12, where the signal band is shown with the two background control samples. The resulting parameters are shown on the signal band plot. The signal band m_{ES} distributions with the fitted signal and background components for all four modes are shown in Figure 4.13. The corresponding signal yield for each mode is tabulated in Table 4.5.

The Monte Carlo simulation is used to determine the expected yield of events reconstructed in one $B \to K^*\gamma$ mode that are actually from another ("cross-feed")

and the yield of events from other $b \to s\gamma$ processes such as decays to higher K^* resonance ("down-feed"). These contributions are subtracted from the signal yield normalized according to the measured CLEO branching fractions [31], [32] as shown in Table 4.5.

The branching fractions in each mode are obtained from the fitted yield minus the expected cross-feed and down-feed contribution. A study of Monte Carlo-simulated $B\overline{B}$ decays finds no other backgrounds from $B\overline{B}$ decays apart from these contributions. This corrected yield is then divided by the efficiency and the number of $B\overline{B}$ events in the on-resonance data sample ($22.7 \times 10^6 B\overline{B}$ events), giving the branching fractions as shown in Table 4.5. The efficiency shown include the partial branching fractions for the appropriate K^* decay (the previously discussed efficiencies were for the reconstruction of the exclusive K^* decay mode). The statistical error is obtained from the fit. The systematic errors for each mode are discussed later in Section 4.8.

Mode	Efficiency %	Signal Yield events	Cross-feed events	Down-feed events	$\mathcal{B}[B \to K^*\gamma]$ $\pm$stat. $\pm$ sys. $\times 10^{-5}$
$K^+\pi^-$	14.0	135.7 ± 13.3	0.4 ± 0.1	0.6 ± 0.1	$4.24 \pm 0.41 \pm 0.22$
$K^0_S\pi^0$	1.4	14.8 ± 5.6	0.4 ± 0.1	1.0 ± 0.2	$4.10 \pm 1.71 \pm 0.42$
$K^0_S\pi^+$	3.9	28.1 ± 6.6	0.7 ± 0.2	1.2 ± 0.2	$3.01 \pm 0.76 \pm 0.21$
$K^+\pi^0$	4.3	57.6 ± 10.4	1.2 ± 0.2	2.6 ± 0.4	$5.52 \pm 1.07 \pm 0.38$

Table 4.5: Signal yields from the maximum likelihood fits with efficiencies, inter-mode cross-feed and down-feed from $b \to s\gamma$ events with higher hadronic mass as predicted by the Monte Carlo simulation

4.7.2 Extraction of Conjugate Yields

A similar simultaneous unbinned extended maximum likelihood fit determines the signal yield of each sign individually for each K^* mode (with the exception of the self-conjugate $K^{*0} \to K^0_S\pi^0$ mode). While the sample is divided into two disjoint subsamples corresponding to the flavor of the B candidates, the yield of each sign is determined simultaneously in a single fit with a common background contribution

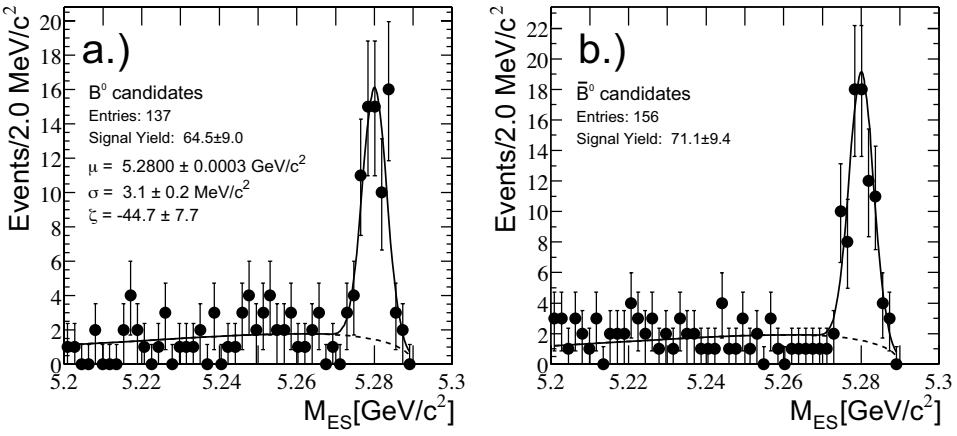

Figure 4.14: Results of the simultaneous extended maximum-likelihood fit for A_{CP} measurement in the mode $B^0 \to K^{*0}\gamma,\ K^{*0}K^+\pi^-$. a.) $K^{*0} \to K^+\pi^-$ candidates. b.) $\overline{K^{*0}} \to K^-\pi^+$ candidates

using the ARGUS threshold function, under the assumption that the continuum background is charge-symmetric.

The free parameters of each fit are the signal yields in the signal band for B and $\overline{B}$, a common ARGUS parameter for all three samples, a common yield of background events for both signs in the signal band, the yield of background in the sideband and the off-resonance data, and the signal PDF parameters, which are fixing or floating as in the branching fraction fit, but fixed between the B and $\overline{B}$ in each mode. The fit is illustrated in Figure 4.14 for the $K^{*0} \to K^+\pi^-$ mode, and the results for all modes tabulated in Table 4.6.

The direct CP violation in the modes is quantified by:

$$A_{CP} = \frac{1}{1-2\eta}\frac{\Gamma(\overline{B} \to \overline{K^*}\gamma) - \Gamma(B \to K^*\gamma)}{\Gamma(\overline{B} \to \overline{K^*}\gamma) + \Gamma(B \to K^*\gamma)} \tag{4.8}$$

where η is the fraction of events which are mistagged. The mistag rate is found from the Monte Carlo simulation to be very small (0.0025 ± 0.0008) and results in negligible dilution of the asymmetry. The charge asymmetry for each mode is tabulated in Table 4.6, where the statistical error is calculated from the errors on

Mode	$\overline{B}^0$ Yield (Events)	B^0 Yield (Events)	A_{CP}(signal) ($\pm$stat. $\pm$ sys.)	A_{CP}(background) ($\pm$stat.)
$K^+\pi^-$	64.5 ± 9.0	71.1 ± 9.4	$-0.049 \pm 0.094 \pm 0.012$	-0.011 ± 0.104
$K^0_S\pi^+$	11.6 ± 3.9	16.5 ± 4.8	$-0.190 \pm 0.210 \pm 0.012$	-0.080 ± 0.080
$K^+\pi^0$	29.2 ± 6.8	26.7 ± 6.5	$0.044 \pm 0.155 \pm 0.021$	-0.022 ± 0.105

Table 4.6: The measured A_{CP} in signal and background samples.

the fitted conjugate yields. The systematic error is discussed later in Section 4.8. In order to check our assumption that the background is charge-symmetric, we calculate A_{CP} from the background yields in the sideband regions $5.20 < m_{\rm ES} < 5.27\,{\rm GeV}/c^2$ and $-0.2 < \Delta E^* < 0.1\,{\rm GeV}$ and find that they are all consistent with zero.

	% Uncertainty in $\mathcal{B}[B \to K^*\gamma]$			
	$K^+\pi^-$	$K^0_S\pi^0$	$K^0_S\pi^+$	$K^+\pi^0$
$m_{\rm ES}$ line shape	-	7.4	1.7	1.9
Background shape	1.0	-	-	3.8
Down-feed modeling	1.0	1.5	1.0	1.2
$K^\pm/\pi^\pm$ tracking efficiency	2.4	-	1.2	1.3
K^0_S eefficiency	-	4.5	4.5	-
Kaon identification	0.7	-	-	1.0
Photon efficiency	1.3	1.3	1.3	1.3
Photon distance cut	2.0	2.0	2.0	2.0
π^0 efficiency	-	2.5	-	2.5
π^0/η veto	1.0	1.0	1.0	1.0
Energy resolution	2.5	2.5	2.5	2.5
Energy scale	1.0	1.0	1.0	1.0
MC statistics	1.9	2.4	1.5	2.1
B counting	1.6	1.6	1.6	1.6
Total	5.3	10.3	6.7	7.0

Table 4.7: Systematic uncertainties expressed as percent of $\mathcal{B}[B \to K^*\gamma]$ in each mode.

4.8 Systematic Uncertainties

The systematic uncertainties for the branching fraction measurement are summarized in Table 4.7. With the exception of the $m_{\rm ES}$ line shape, the background shape and the B counting systematic, they are associated with the Monte Carlo prediction of the signal reconstruction efficiency. In particular, there are a number of systematics uncertainties associated with the photon reconstruction efficiency which are common across all four modes. A second set is associated with the reconstruction of the K^* and are different for each of the K^* decay modes. Finally, there are a set of systematic uncertainties associated with the signal extraction, the finite number of Monte Carlo simulated events, and the uncertainty in the number of $B\overline{B}$ events in the on-resonance data sample [39].

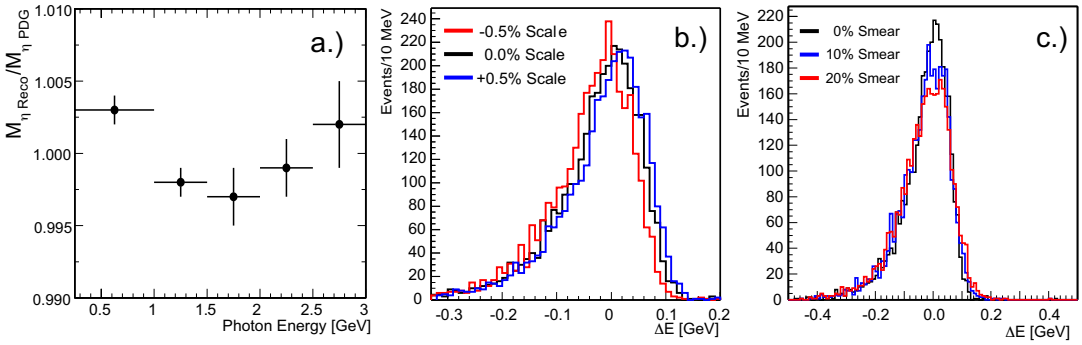

Figure 4.15: a.) Ratio of the mass of reconstructed symmetric $\eta \to \gamma\gamma$ decays as function of photon energy and nominal η mass. Effect of b.) scale shifts or c.) broadening of the EMC energy resolution on the signal ΔE^* distribution.

4.8.1 Photon Reconstruction

The selection criteria for the photon candidate carry systematic uncertainties which result from the accuracy of the Monte Carlo simulation of the photon response in the EMC and our ability to estimate any discrepancy. The first systematic uncertainty is associated with the efficiency for finding a photon in the EMC, resulting from the study described in Section 4.6.1. A second class of systematic uncertainties results

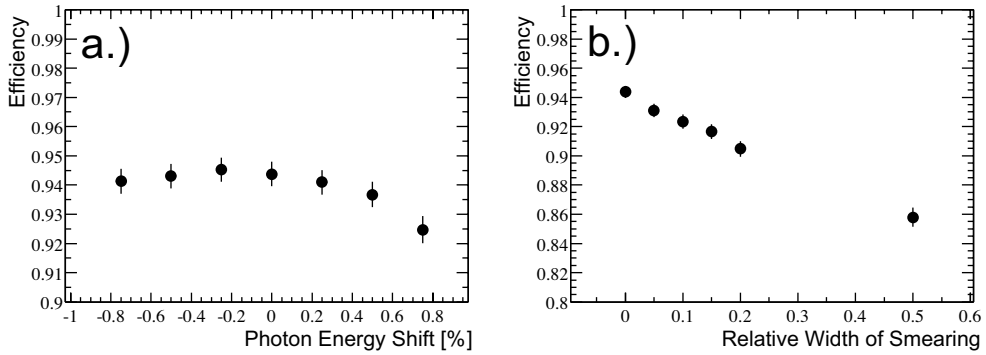

Figure 4.16: Variation in efficiency for the ΔE^* selection as function of a.) fractional offset in the energy, and b.) smearing of the energy resolution (right).

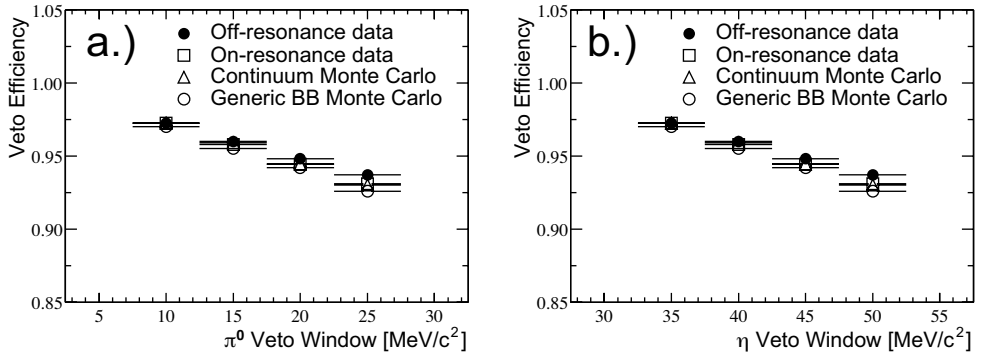

Figure 4.17: Efficiency of the a.) π^0 veto and b.) η veto as a function of the veto window width with various samples of data and Monte Carlo simulation as described in the text.

from differences in the energy resolution of the EMC between the Monte Carlo simulation and the data. Since the ΔE^* resolution of the B candidate is dominated by the photon energy resolution, the ΔE^* selection efficiency is particularly sensitive to calibration errors of the EMC response or mis-modeling of the resolution in the Monte Carlo simulation. Two control samples, consisting of energetic π^0 decays in which one photon converts to an e^+e^- pair reconstructed in the tracking, and symmetric η decays (described in Chapter 3.3) crosscheck any such effects. The peak of the reconstructed symmetric $\eta \to \gamma\gamma$ decays as a function of photon energy is

shown in Figure 4.15. The deviations of the peak value from the nominal value of 542.3 MeV/c^2 are less than 0.5%, thus constraining any offset in the energy calibration. A comparison of the width of the reconstructed mass distribution the data and Monte Carlo constrain any broadening of the EMC energy response in the data relative to the Monte Carlo to 10%.[40].

The effect of a systematic shift in the energy scale or broadening of the EMC energy resolution on the signal ΔE^* reconstruction is shown in Figure 4.15. The broadening is simulated by convoluting the original distribution with a Gaussian distribution. The effect on the efficiency of the ΔE^* selection due to energy scale uncertainty is shown on the right in Figure 4.16. The deviations in the ΔE^* selection efficiency is less than 1% for a 0.5% variation; this is taken as the systematic uncertainty resulting from energy scale deviations in the EMC. The effect of poorer resolution on the ΔE^* selection efficiency results in deviations of up to 2.5% with Gaussian smearing corresponding to 10% wider width, as shown in Figure 4.16.

A third set of systematic uncertainties result not from the modeling of the signal photon response, but from the overall occupancy of the EMC from objects other than the signal photon. The efficiency for the photon isolation and the π^0 and η vetoes is sensitive to any discrepancy in the simulation: if there are more(less) calorimetric objects in the event, then it will be more(less) likely that one of these objects will be close to the signal photon, or that one of these photons will form an invariant mass with the signal photon close to the π^0 or η mass. The effect of any difference in occupancy is studied by "embedding" the photon response into events both from the Monte Carlo simulation and in the data. In the case of the isolation cut, the response of the EMC to photons from radiative Bhabha events in the data is added to the information already present in Monte Carlo simulated $B\overline{B}$ events and a sample of exclusively reconstructed $B\overline{B}$ events in the data. The event is then reconstructed again with the new photon and the isolation efficiency in the data and Monte Carlo simulation compared. The resulting distance distributions are shown in Figure 4.18, along with the efficiency as a function of the required isolation. The deviation of the efficiencies between the two samples at 25 cm (the value actually used) of 2.0% is taken as the systematic uncertainty.

For the π^0 and η veto, the full response of the photon is not embedded. Rather, the π^0 and η vetoes are applied to invariant mass combinations formed from momentum vectors randomly generated from the photon spectrum of $B \to K^*\gamma$ events and the photons actually reconstructed in the event. A comparison of the efficiency in generic continuum and $B\overline{B}$ Monte Carlo simulation and off and on-resonance data is shown in Figure 4.17. The differences between the Monte Carlo simulation and data is less than 1% for the chosen veto windows. This is taken as the systematic uncertainty in the efficiency for the π^0 and η veto.

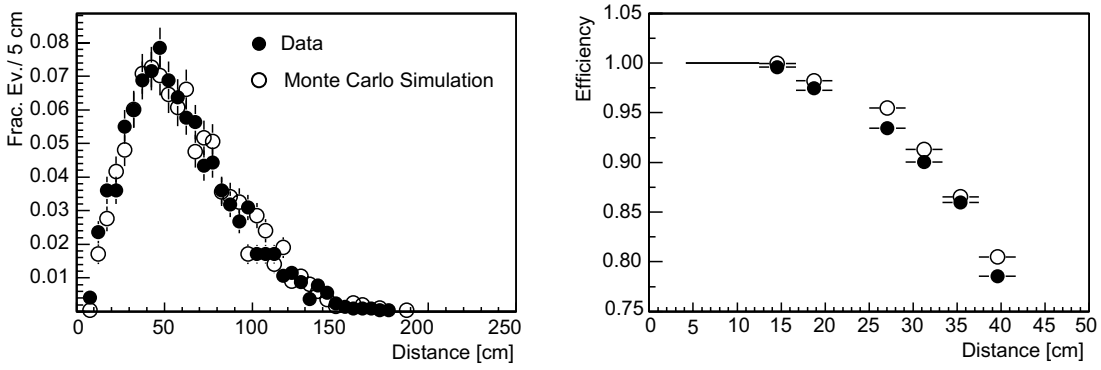

Figure 4.18: Distance distributions from photons candidates embedded in $B\overline{B}$ Monte Carlo simulation and exclusively reconstructed $B \to D\pi$ events. Left: distance distribution. Right: Efficiency as a function of isolation.

4.8.2 K^* Reconstruction

The systematic uncertainties for the K^* reconstruction are different for each mode. For the track reconstruction and K^0_S reconstruction, a systematic uncertainty is derived from the statistical uncertainties in the tabulated empirical corrections described in Section 4.6.2. For modes involving kaon selection ($K^{*0} \to K^+\pi^-$ and $K^{*+} \to K^+\pi^0$), the selection is compared between Monte Carlo and data for kaons identified from $D^* \to D^0\pi^+$, $D^0 \to K^-\pi^+$ decays. The statistical uncertainty in this comparison is the systematic uncertainty for the selection.

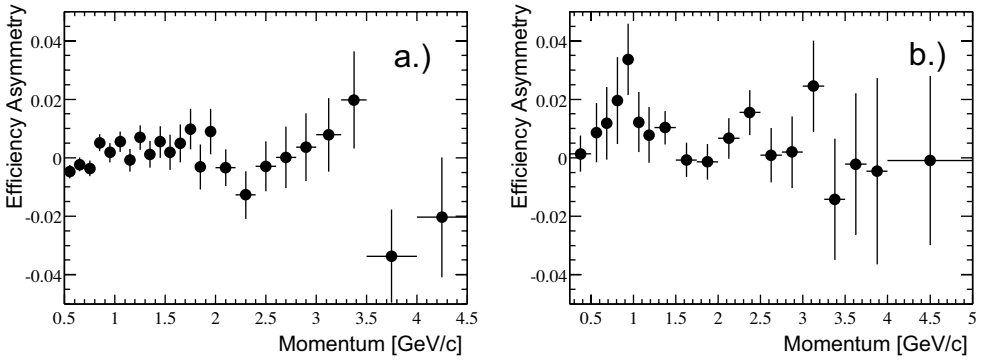

Figure 4.19: a.) Asymmetry of the inclusive $K^0_s \to \pi^+\pi^-$ yield as a function of the π^+ momentum. b.) Asymmetry of the kaon selection efficiency as a function of kaon momentum from $D^{*+} \to D^0\pi^+,\ D^0 \to K^+\pi^-$ decays.

4.8.3 Systematics for A_{CP} Measurement

Charge dependent asymmetries in the K^* reconstruction can produce systematic uncertainties in the A_{CP} measurement by biasing the reconstruction of one sign of the B decay over the other. The sources of possible biases are in the particle identification and the track reconstruction.

Particle Identification

Possible asymmetries in the kaon efficiency are estimated using the $D^{*+} \to D^0\pi^+,\ D^0 \to K^+\pi^-$ sample and its charge conjugate. The efficiencies are measured separately for positive and negative kaon samples as a function of momentum. The relative difference in the efficiencies of the K^+ selection to the K^- selection is shown on the right in Figure 4.19. The weighted average of the statistical errors in the efficiency differences according to the phase space of the kaons in the $B \to K^*\gamma$ process is found to be 0.7%. This is taken as the systematic uncertainty due to possible asymmetries in the kaon selection.

Track Reconstruction

In direct CP-violation searches involving final states with unequal numbers of positive and charged tracks (*e.g.* $K^{*+} \to K^+\pi^0$ and charge conjugate mode), an overall asymmetry between the reconstruction efficiency for positive and charged tracks translates directly into an asymmetry in the reconstruction efficiency between the mode and its charge conjugate mode. A study of such effects is performed in the same control samples used to determine the charged-averaged track efficiency by considering each charge separately. While statistically significant biases are observed, none exceed 0.5%; this is taken as a systematic uncertainty for these modes [38].
In searches involving an equal number of positive and negative tracks (*e.g.* $K^{*0} \to K^+\pi^-$), overall tracking asymmetries of this kind have no affect on A_{CP}: the relative inefficiency for reconstructing positive tracks and negative tracks affects both the mode and its charge conjugate identically. It is possible only for phase space-dependent effects to produce a systematic bias. This arises from the difference in the momentum distribution of the the kaon and pion in the $B \to K^*\gamma$ decay. In this case the asymmetry must be quantified at each momentum and corrected based on the phase space of the charged particles in the decay to determine its effect on A_{CP}. The inclusive $K^0_S \to \pi^+\pi^-$ decay provides a clean sample of pion tracks of both signs with which to study momentum-dependent asymmetries in the tracking efficiency. The momentum spectrum of the π^+ in these decays can be compared with the spectrum of π^-. Since the decay is symmetric between the two daughter pions, the spectra should be identical. An asymmetry at a particular momentum p would distort the spectrum of one sign with respect to the other at that momentum, yielding a non-zero value of $A(p)$ defined as:

$$A(p) = \frac{N_+(p) - N_-(p)}{N_+(p) + N_-(p)} \tag{4.9}$$

where $N_\pm(p)$ is the yield of $\pi^\pm$ in the sample with momentum p. The results are shown in Figure 4.19. The systematic uncertainty is estimated by a weighted average according to the reconstructed track momenta and found to be less than 1%. This is assigned as a systematic error on the A_{CP} measurement.

Mode	ζ with kaon selection	ζ without kaon selection
$K^{*0} \to K^+\pi^-$	-60.3 ± 10.7	-61.2 ± 5.2
$K^{*+} \to K^+\pi^0$	-62.7 ± 8.8	-61.4 ± 3.7

Table 4.8: ARGUS ζ with and without kaon selection.

4.8.4 Signal Extraction

The lineshape used to describe the $m_{\rm ES}$ distribution for the signal are treated in various ways for the different modes, resulting in different systematic uncertainties. For the mode $K^{*0} \to K^+\pi^-$, the parameters are free in the fit; the uncertainty in the yield incorporates the uncertainty in the line shape. For the other modes, certain parameters are fixed, and the uncertainties in these parameters lead to systematic uncertainties which are estimated by varying the parameters and re-extracting the signal yield. The variations in the fixed parameters are summarized in Table 4.4. The errors on the $m_{\rm ES}$ widths are the range of variations used to estimate the uncertainty on the signal yield. The Novosibirsk τ parameter is fixed and varied to the number in parentheses.

For $K^{*0} \to K^0_S\pi^0$, we fix the width to the Monte Carlo prediction with an empirical correction from the $K^{*0} \to K^+\pi^-$, where the observed width is larger than that predicted by the Monte Carlo simulation, as described in Section 4.7. The statistical uncertainty in this correction defines the range of values shown in Table 4.4. The tail parameter τ of the Novosibirsk function for this mode is varied between the Monte Carlo prediction and zero, corresponding to the Gaussian limit, and the resulting variations in the signal yield taken as another source of systematic uncertainty. For the modes $K^{*+} \to K^+\pi^0$, the Novosibirsk width is free in the fit, but the tail parameter is fixed to the Monte Carlo expectation. The signal extraction is performed with the tail parameter also floating, and the change in yield taken as a systematic uncertainty. Finally, for the mode $K^{*+} \to K^0_S\pi^+$, the width is varied within the uncertainties of the empirical correction in the manner described for the $K^{*0} \to K^0_S\pi^0$.

A second systematic uncertainty results from the relaxing of the particle identification requirements for the off-resonance data used in the signal extraction for modes with a charged kaon ($K^{*0} \to K^+\pi^-$ and $K^{*+} \to K^+\pi^0$). The concern is that candidates with "fake" kaons may distort the $m_{\rm ES}$ distribution of this background and bias the signal yield. The distribution of events with the kaon selection and the loosened selection are compared in the Monte Carlo and found to be compatible. A systematic uncertainty is derived by fixing the off-resonance ζ parameter by a fixed amount relative to the on-resonance data, where the particle identification is not relaxed, thus simulating the possibility that the two distributions have different $m_{\rm ES}$ distributions. The range of possible offsets is determined from the statistical uncertainty in the comparison of off-resonance data shown in Table 4.8, where the ζ parameter with and without the kaon selection are compared and found to be in agreement. The values are obtained with a loosened $\cos\Theta_T^*$ selection to enhance the statistics.

4.9 Cross checks

The reconstructed events in the signal region can be cross-checked by examining kinematic quantities associated with the reconstruction of the K^* and the photon. For the K^*, we expect the reconstructed $M_{K\pi}$ for the signal events to follow the Breit-Wigner distribution. The $M_{K\pi}$ distribution for the $K^{*0} \to K^+\pi^-$ mode for events in the region $m_{\rm ES} > 5.27\,{\rm GeV}/c^2$ and $-200\,{\rm MeV} < \Delta E^* < 100\,{\rm MeV}$ is shown in Figure 4.20. The distribution is consistent with the expected Breit-Wigner peaked at $896\,{\rm MeV}/c^2$ with a width of $50\,{\rm MeV}/c^2$. A linear shape describes the background. For the photon reconstruction, we expect that the ΔE^* distribution is dominated by the photon resolution, since the tracks in the $K^{*0} \to K^+\pi^-$ are reconstructed with greater precision. The ΔE^* distribution for $K^{*0} \to K^+\pi^-$ is shown on the right in Figure 4.20 together with the distribution expected from the Monte Carlo simulation. The background is described by a linear function. The agreement confirms the accuracy of the Monte Carlo simulation of the photon reconstruction, as well as the energy calibration of the EMC.

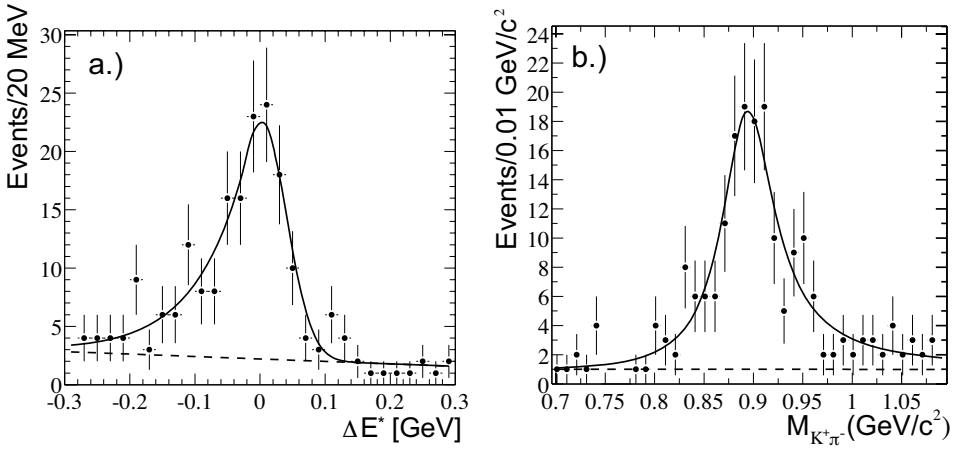

Figure 4.20: a.) $M_{K\pi}$ for $K^{*0} \to K^+\pi^-$ mode candidates with $m_{\rm ES} > 5.27\,{\rm GeV}/c^2$ and $-200\,{\rm MeV} < \Delta E^* < 100\,{\rm MeV}$. b.) ΔE^* for the $K^{*0} \to K^+\pi^-$ mode candidates with $m_{\rm ES} > 5.27\,{\rm GeV}/c^2$.

4.10 Averaged Results and Conclusions

The branching fraction of the decay $B \to K^*\gamma$ is measured in four decay modes of the K^* resonance along with the direct CP violation parameter A_{CP} in the three tagging modes as shown in Table 4.9. The signal reconstruction efficiency is determined from Monte Carlo simulation with corrections and systematic uncertainties determined from a number of control samples in the data. Likewise, charge-dependent reconstruction biases which may affect the A_{CP} measurements are studied and constrained.

The branching fraction for the individual partial branching fractions are averaged to determine a branching fraction for $B^0 \to K^{*0}\gamma$ and $B^+ \to K^{*+}\gamma$. We do not average the B^0 and B^+ modes due to the possibility of isospin violation which would result in different branching fractions. In order to account properly for the uncorrelated statistical and systematic errors and the correlated systematic errors, the average branching fractions are determined by minimizing the χ^2:

$$\chi^2 = \vec{x}^T V^{-1} \vec{x} \tag{4.10}$$

Mode	$\mathcal{B}[B \to K^*\gamma]$ $/10^{-5}$	A_{CP}
$K^{*0} \to K^+\pi^-$	$4.24 \pm 0.41 \pm 0.22$	$-0.049 \pm 0.094 \pm 0.012$
$K^{*0} \to K^0_S\pi^0$	$4.10 \pm 1.71 \pm 0.42$	
$K^{*+} \to K^+\pi^0$	$5.52 \pm 1.07 \pm 0.38$	$0.044 \pm 0.155 \pm 0.021$
$K^{*+} \to K^0_S\pi^+$	$3.01 \pm 0.76 \pm 0.21$	$-0.190 \pm 0.210 \pm 0.012$

Table 4.9: Branching fraction and A_{CP} measurements for individual final states.

Average	
$\mathcal{B}[B^0 \to K^{*0}\gamma]$	$[4.23 \pm 0.40 \pm 0.22] \times 10^{-5}$
$\mathcal{B}[B^+ \to K^{*+}\gamma]$	$[3.83 \pm 0.62 \pm 0.22] \times 10^{-5}$
A_{CP}	$-0.44 \pm 0.076 \pm 0.012$
	$-0.17 < A_{CP} < 0.082$ at 90% C.L.

Table 4.10: Averaged results for $\mathcal{B}[B^0 \to K^{*0}\gamma]$, $\mathcal{B}[B^+ \to K^{*+}\gamma]$ and A_{CP} for all self tagging modes.

where x is the vector of the two branching fraction measurements in each mode that we wish to average, and V is the covariance matrix which accounts for the correlated and uncorrelated uncertainties. The errors on the branching fraction are likewise determined from the covariance matrix to account for correlations. Explicitly, the covariance matrix takes the form:

$$V = \begin{pmatrix} \sigma_1^2 + \kappa_1^2 & 0 & 0 & 0 \\ 0 & \sigma_2^2 + \kappa_2^2 & 0 & 0 \\ 0 & 0 & \sigma_3^2 + \kappa_3^2 & 0 \\ 0 & 0 & 0 & \sigma_4^2 + \kappa_4^2 \end{pmatrix} + F \times (\sigma_\gamma^2 + \sigma_{\mathcal{L}}^2) + \begin{pmatrix} 0 & 0 & 0 & 0 \\ 0 & \sigma_{\pi^0}^2 & \sigma_{\pi^0}^2 & 0 \\ 0 & \sigma_{\pi^0}^2 & \sigma_{\pi^0}^2 & 0 \\ 0 & 0 & 0 & 0 \end{pmatrix} + \begin{pmatrix} 0 & 0 & 0 & 0 \\ 0 & \sigma_{K^0_S}^2 & 0 & \sigma_{K^0_S}^2 \\ 0 & 0 & 0 & 0 \\ 0 & \sigma_{K^0_S}^2 & 0 & \sigma_{K^0_S}^2 \end{pmatrix} \tag{4.11}$$

where F is the matrix composed of 1 in every entry. The matrices are indexed by mode (1 for $K^+\pi^-$, 2 for $K^0_S\pi^0$, 3 for $K^+\pi^0$ and 4 for $K^0_S\pi^+$). The first matrix accounts for the statistical error and systematic error which are particular to the individual modes, the second term describes the photon selection and $B\overline{B}$ counting systematic errors which are common across all modes, while the third and fourth terms describe the common systematic errors in the π^0 and K^0_S reconstruction for the appropriate modes. The individual systematic errors are tabulated in Table 4.7, and the statistical error is obtained from the signal extraction fit. For the A_{CP} measurement, we average the three self-tagging modes in the same manner. The averaged results are summarized in Table 4.10.

Chapter 5

The Search for $B \to \rho\gamma$

5.1 Introduction

The $B \to \rho\gamma$ analysis proceeds by reconstructing the decays $B^0 \to \rho^0\gamma$, $\rho^0 \to \pi^+\pi^-$ and $B^+ \to \rho^+\gamma$, $\rho^+ \to \pi^+\pi^0$ in a manner analogous to the $B \to K^*\gamma$ analysis. The analysis is peformed on $56.2\,\mathrm{fb}^{-1}$ of on-resonance data ($61.7 \times 10^6 B\overline{B}$ decays) and $6.4\,\mathrm{fb}^{-1}$ of off-resonance data taken in 2000 and 2001 The presence of severe backgrounds has led to a more aggressive approach in the background suppression and signal extraction. As in the $B \to K^*\gamma$ analysis, the primary background is from continuum π^0 and η production and initial state radiation of high energy photons. We can expect, however, that the background for $B \to \rho\gamma$ will be considerably worse for several reasons:

- With the expectation $\mathcal{B}[B^0 \to \rho^0\gamma] \sim 10^{-6}$, the signal rate is ~ 50 times less than for $B \to K^*\gamma$. This requires that the background be reduced by this factor relative to the background in $B \to K^*\gamma$ in order to achieve the same signal-to-background ratio. In addition, the $B \to K^*\gamma$ itself poses a dangerous background as it is topologically identical and kinematically similar. The excellent kaon/pion separation abilities of the DIRC is expected to allow substantial suppression of this background relative to previous analyses.

- The natural width of the ρ resonance is three times wider than the K^* ($150\,\mathrm{MeV}/c^2$

vs. $50\,\mathrm{MeV}/c^2$). In order to obtain the same signal efficiency, a resonance mass selection three times wider must be used, introducing proportionately higher background.

- The use of kaon identification to positively identify the kaon in the decays $K^{*0} \to K^+\pi^-$ and $K^{*+} \to K^+\pi^0$ reduced the combinatoric background in the continuum by a factor of ~ 5. The ability to reject kaons using pion identification in the $B \to \rho\gamma$ does not result in the same benefit, since pions are much more copiously produced than kaons in the continuum.

- The $B^+ \to \rho^+\gamma$ suffers an additional background from $B^+ \to \rho^+\pi^0$. The branching fraction for this mode is unmeasured and expected to be $\sim 10 \times \mathcal{B}[B^+ \to \rho^+\gamma]$. The different helicity structure of the ρ decay in this mode is used to suppress this background.

We employ a neural network and a maximum likelihood fit in three variables in order to obtain optimal background suppression and signal sensitivity. As in the $B \to K^*\gamma$ analysis, we make use of the off-resonance data as a control sample to cross check the properties of the continuum background. In addition, we use the copiously produced $B \to D\pi$ sample in the data, as well the $B \to K^*\gamma$ itself to cross check the signal properties.

The current theoretical and experimental status of $B \to \rho\gamma$ is summarized in Table 5.1. Isospin symmetry predicts that the rate of $B^+ \to \rho^+\gamma$ is twice that of $B^0 \to \rho^0\gamma$. The experimental limits lie approximately an order of magnitude above the theoretical predictions.

The $B \to \rho\gamma$ analysis was performed "blind": the event selection and signal extraction procedure were studied and defined without knowledge of the yield or distribution of events in the signal region of $-0.2\,\mathrm{GeV} < \Delta E^* < 0.1\,\mathrm{GeV}$ and $m_{\mathrm{ES}} > 5.27\,\mathrm{GeV}/c^2$.

Author	$\mathcal{B}[B^0 \to \rho^0\gamma]/10^{-6}$	$\mathcal{B}[B^+ \to \rho^+\gamma]/10^{-6}$
Bosch & Buchalla		1.6 ± 0.5
Ali & Parkhomenko	0.49 ± 0.17	0.85 ± 0.30
CLEO	< 17	< 13
BELLE	< 10.6	< 9.9

Table 5.1: Current theoretical predictions and experimental limits for $B \to \rho\gamma$.

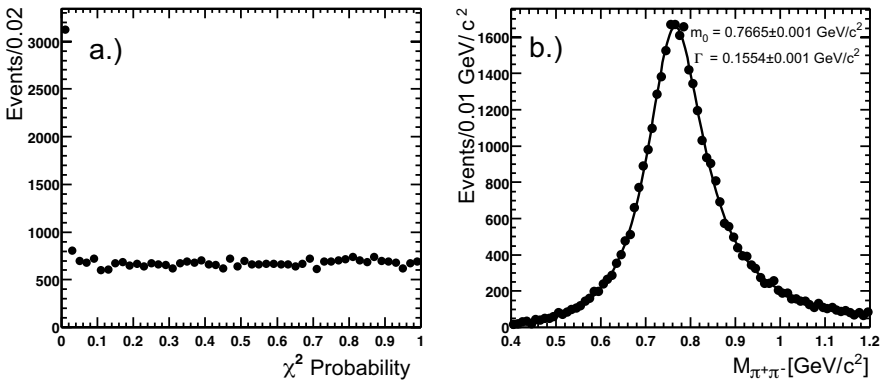

Figure 5.1: a.) χ^2 probability of the fitted vertex for Monte Carlo $B^0 \to \rho^0\gamma$ events. b.) Reconstructed ρ resonance mass $M_{\pi\pi}$.

5.2 Event Reconstruction

The event reconstruction for $B^0 \to \rho^0\gamma$ and $B^+ \to \rho^+\gamma$ is similar to the analogous modes in $B \to K^*\gamma$, *i.e.* $B^0 \to K^{*0}\gamma$, $K^{*0} \to K^+\pi^-$ and $B^+ \to K^{*+}\gamma$, $K^{*+} \to K^+\pi^0$. The global event selection, photon, π^0 and track reconstruction are identical to that described in Sections 4.1, 4.2 , 4.3.4 and 4.3.1.

The ρ resonance is reconstructed in the decays $\rho^0 \to \pi^+\pi^-$ and $\rho^+ \to \pi^+\pi^0$. For the ρ^0 reconstruction, we require that the χ^2 probability of the vertex fit is at least 0.01. We select ρ candidates in a broad mass window of $0.520 < M_{\pi\pi} < 1.020\,\mathrm{GeV}/c^2$ in anticipation of utilizing the $M_{\pi\pi}$ distribution in the maximum likelihood fit. Finally, we require that the CMS frame momentum of the ρ candidate lie between $2.35 < p^*_\rho < 2.8\,\mathrm{GeV}/c$. This selection has nearly no inefficiency for the signal, but eliminates spurious $\pi\pi$ combinations from the decay of the other B meson. The

reconstruction of the ρ candidates is illustrated in Figure 5.1.

A tight charged pion selection has been developed for this analysis. The primary purpose of the pion selection is to veto the $B \to K^*\gamma$ decays which are topologically identical apart from the charged kaon produced in the K^* decay. Since the $B \to K^*\gamma$ is expected to occur at a rate ~ 50 times that of $B \to \rho\gamma$, it is desirable to achieve kaon rejection of about the same factor.

The basis for the pion selection used in this analysis is a veto on the loosest kaon selection developed in Reference [44]. The performance of this selection is shown on the left in Figure 5.2, where the pion efficiency and kaon misidentification rates have been determined from a sample of $D^{*+} \to D^0\pi^+$, $D^0 \to K^+\pi^-$ decays.

The kaons misidentified as pions by this selector typically have a lower number of reconstructed Cherenkov photons N_γ in the DIRC. Further improvement in the selection can be obtained by comparing N_γ to the expected number of photons based on the momentum and entrance angle of the track into the DIRC under the hypothesis that it is a pion. The consistency of the observed N_γ to the expected number of photons is calculated and required to be greater than 0.0001 for tracks with momentum greater than $0.6\,\mathrm{GeV}/c$. With this additional requirement, a significant reduction in kaon misidentification rate is achieved in the momentum range $1 - 3\,\mathrm{GeV}/c$ where most of the kaons from $B \to K^*\gamma$ lie, at the cost of a modest decrease in pion efficiency, as shown in Figure 5.2.

The B candidate in both modes are reconstructed from the photon and ρ candidates. The m_{ES} and ΔE^* distributions for the two signal modes are shown in Figure 5.3. Candidates with $m_{\mathrm{ES}} > 5.2\,\mathrm{GeV}/c^2$ and $-0.3 < \Delta E^* < 0.3$ are selected. In the case of multiple candidates, the candidate with the smallest ΔE^* is chosen. The poorer resolution of the $B^+ \to \rho^+\gamma$ relative to the $B^0 \to \rho^0\gamma$ in both m_{ES} and ΔE^* results from the π^0 in the final state, which has poorer resolution than the charged pion in $B^0 \to \rho^0\gamma$.

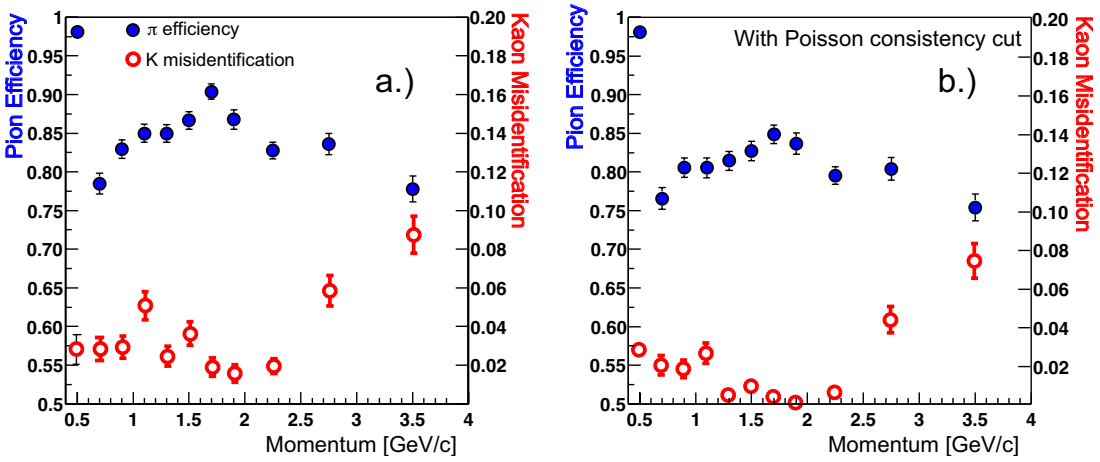

Figure 5.2: Pion efficiency and kaon misidentification rates for pion selection a.) without Cherenkov photon consistency cut and b.) consistency > 0.0001. The data are from $D^{*0} \to D^0\pi^+$, $D^0 \to K^+\pi^-$ decays

5.3 Continuum Background Supression

Due to the severe continnuum backgrounds in this analysis, we employ the event topology variables R_2' (the ratio of second and zeroth Fox-Wolfram moments in the frame recoiling from the photon candidate) and the energy E^*_{Ci} in 18 cones centered on the photon momentum in the CMS frame, in addition to the variables $\cos\Theta^*_T$, $\cos\Theta^*_B$ and $\cos\Theta_H$ used in the $B \to K^*\gamma$ analysis in order to achieve more background suppression. We find that the vertex separation of the reconstructed signal candidate with the rest of the event, as well as an analysis of the flavor content in the event provide useful information for background rejection. The variables are combined in a neural network (described in Section 5.3.4) to produce one background suppression variable.

5.3.1 Vertexing: Δz ($B^0 \to \rho^0\gamma$ only)

The asymmetric energies of the colliding beams at $PEP-II$ produce $B\overline{B}$ pairs moving along the z-axis with $\beta\gamma = 0.56$. This allows the $B\overline{B}$ mesons to traverse on average $250\,\mu$m in z before decaying. If one is able to reconstruct the decay points

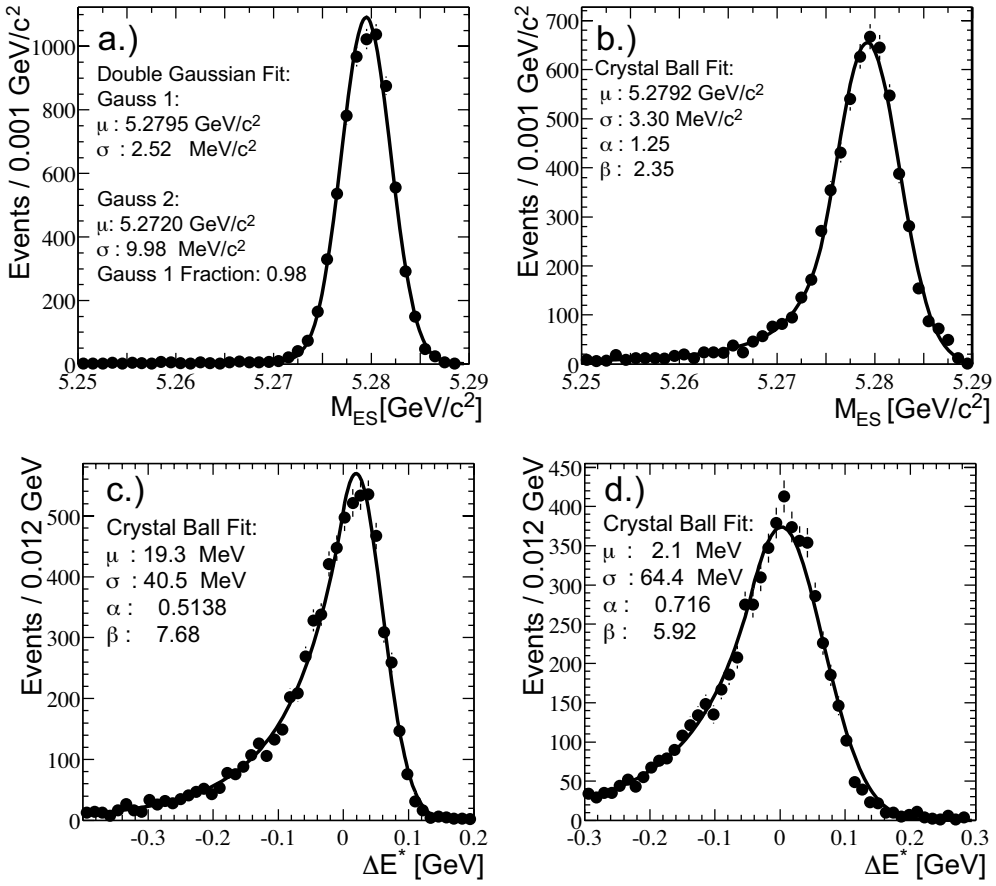

Figure 5.3: Left: $m_{\rm ES}$ for a.) $B^0 \to \rho^0\gamma$ and b.) $B^+ \to \rho^+\gamma$ candidates in the signal Monte Carlo simulation. ΔE^* for c.) $B^0 \to \rho^0\gamma$ and d.) $B^+ \to \rho^+\gamma$.

of both the B^0 and $\overline{B}^0$, the uncorrelated decay times of the two mesons results in an exponential distribution for the difference of the flight distances:

$$\Delta z = z_{\rho\gamma} - z_{\rm tag} \tag{5.1}$$

as for the individual flight distances. Here, $z_{\rho\gamma}$ is the z position of the $B^0 \to \rho^0\gamma$ decay and $z_{\rm tag}$ is the z position of the "tag" B, that is the other B which did not decay to $\rho^0\gamma$. Since at least two charged tracks in the reconstructed B candidate are needed for the vertexing algorithm, we use this variable only for $B^0 \to \rho^0\gamma$.

The continuum production which dominates the background originates from a common vertex; the tracks from the background candidates come from the same point as the other tracks in the event. In this case the Δz distributions should be tighter than for the $B^0 \to \rho^0\gamma$, where the other tracks in the event come from an origin displaced in z relative to the $B^0 \to \rho^0\gamma$ decay.

The Δz for each $B^0 \to \rho^0\gamma$ candidate is determined by a vertex-finding algorithm utilizing the tight beam spot constraint in the y axis (approximate 15 μm) together with the reconstructed momentum of the $B^0 \to \rho^0\gamma$ candidate to constrain the decay vertex of the tag B by pointing the B_{CP} momentum back to beam spot to obtain the production point (the $\Upsilon(4S)$ decay vertex) [46]. The momentum vector of the $B_{\rm tag}$ can be inferred from the beam momentum in the lab frame and the reconstructed $B^0 \to \rho^0\gamma$ momentum. The flight path of the $B_{\rm tag}$ is then constrained to lie along the momentum vector extending from the reconstructed production vertex. The algorithm proceeds iteratively by calculating a vertex for all tracks in the event not associated with the $B^0 \to \rho^0\gamma$, removing the track with largest χ^2 contribution if the overall χ^2 is greater than 6, and recalulating the vertex until the χ^2 is less than six.

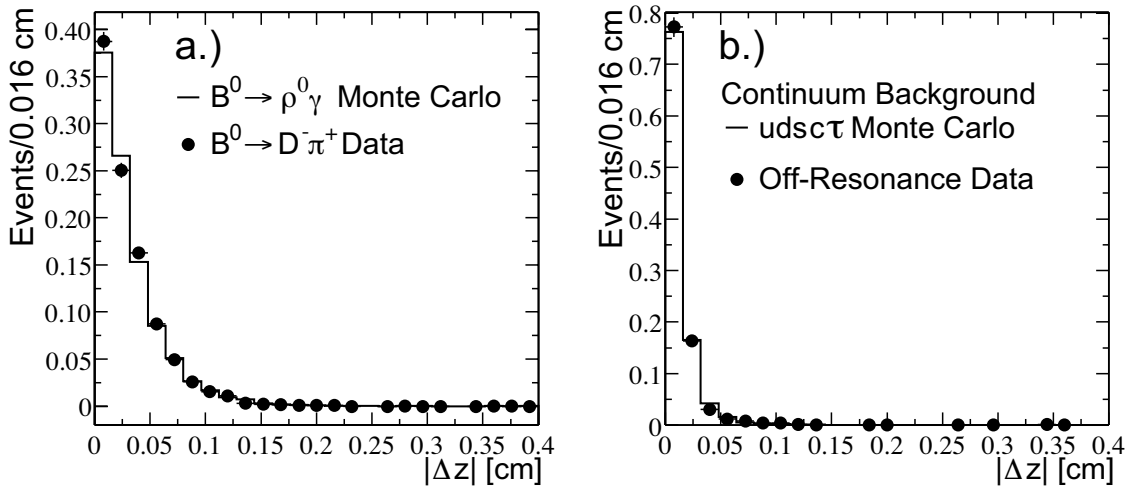

Figure 5.4: $|\Delta z|$ distribution. a.) Signal Monte Carlo events and $B^0 \to D^-\pi^+$ events in the data. b.) Monte Carlo simulated continuum events and off-resonance data

The vertexing algorithm returns an error on Δz based on the fit errors. We require that this error $\sigma(\Delta z)$ is less than 400 μm. We further require that the measured $|\Delta z|$ is less than 4000 μm, approximately fifteen times the expected average decay distance for the signal process. The signal $|\Delta z|$ distribution is shown in Figure 5.4 for Monte Carlo simulated signal events and a control sample of $B^0 \to D^-\pi^+$ events in the data. The reconstructed distributions are in good agreement. Figure 5.4 also shows the $|\Delta z|$ distribution for the continuum Monte Carlo simulation and the off-resonance data. The distribution is narrower than that for the signal process, as expected. The Monte Carlo-simulated continuum background is in good agreement with the off-resonance data.

5.3.2 Tagside Flavor

The decay of $B\overline{B}$ events proceed through weak interaction which allow flavor-tagging of B decays via lepton and kaon production without fully reconstructing the decay. In the case of $B \to \rho\gamma$, the tracks in the event not associated with the signal process originate from the decay of the other B. We then expect that these tracks will contain net lepton, charm and kaon production.
The primary background for the $B \to \rho\gamma$ is the light hadronic continuum ($u\overline{u}/d\overline{d}/s\overline{s}$ production) where the particles are produced through the flavor conserving strong interaction. If kaons are produced, they are produced in pairs with zero net strangeness. Lepton production occurs primarily through decays of pions and kaons. e^+e^- pairs can be produced through photons conversions, Dalitz decays of the π^0 and η, and other internal conversion processes, where e^+e^- pairs are produced. Thus, we expect no net lepton or kaon generation in the continuum. In order to quantify these heuristic notions in a discriminating variable, we consider the following quantities:

1. Net kaon number: N_K = Number of K^+ minus the number of K^-.

2. Net electron number:N_e= Number of e^+ minus the number of e^-.

3. Net muon number: N_μ = Number of μ^+ minus the number of μ^-.

4. Net slow π number: $N_{Sl.\pi}$= Number of slow π^+ minus the number of slow π^-.

5. K_S^0 number: $N_{K_S^0}$= Number of K_S^0.

Each quantity specifies net flavor production of some sort, leptons in the case of 2 and 3, strangeness in the case of 1, and charm (D^*) for 4. We identify charged kaons with a tight selection for the charged kaons [44], electrons with momentum greater than 0.5 GeV/c with tight electron selection [47] and muons with momentum greater than 1.0 GeV/c with a tight muon selection [48]. Slow pions are selected from tracks with momentum p^* in the CMS frame less than 250 MeV/c with the requirement that the momentum be correlated with the thrust axis $\mathbf{T}$ of the tag B requiring $|\cos\Theta_{\mathbf{T}/p^*}| > 0.8$. The K_S^0 candidates are obtained from pairs of oppositely charged tracks with a successfully calculated vertex displaced at least 1 mm from the primary vertex and $M_{\pi\pi} = [0.480, 0.516]$ GeV/c^2. We further require that $\cos\Theta > 0.98$, where Θ is the angle between the vector pointing to the K_S^0 vertex and the reconstructed momentum. The *net flavor* variable

$$\mathcal{F} = |N_e| + |N_\mu| + |N_K| + |N_{Sl.\pi}| + N_{K_S^0} \tag{5.2}$$

then quantifies the net flavor production in the event. The flavor production in $B^0 \to D^-\pi^+$ events from Monte Carlo simulation and data, along with the $B^0 \to \rho^0\gamma$ candidates in the continuum Monte Carlo and off-resonance data is shown in Figure 5.5. Also shown is the net flavor for $B^- \to D^0\pi^-$ events and $B^+ \to \rho^+\gamma$ background candidates. There is good agreement between the Monte Carlo simulation and corresponding data. Since the tag-side flavor production is a property of generic B decays, we expect that the flavor production will be identical for $B^0 \to \rho^0\gamma$ and $B^0 \to D^-\pi^+$ ($B^0\overline{B}^0$ production) and $B^+ \to \rho^+\gamma$ and $B^- \to D^0\pi^-$ (B^+B^- production). The distributions confirm that more net flavor is produced in B decays than in the continuum.

5.3.3 Event Shape Variables

The differences in event topology between the continuum background and the signal $B \to \rho\gamma$ can be quantified by a number of variables. For this analysis, we choose:

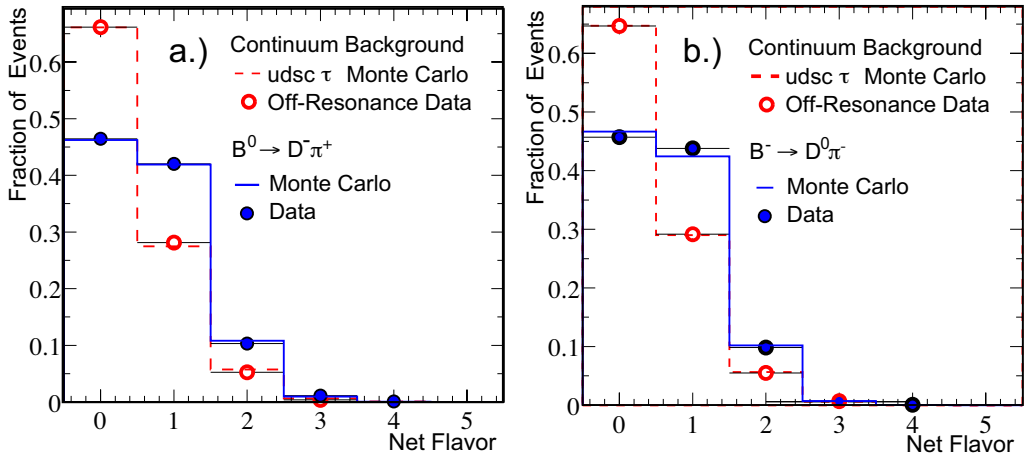

Figure 5.5: Tag-side Flavor production. a.) $B^0 \to D^-\pi^+$ Monte Carlo and Data (blue) compared with $B^0 \to \rho^0\gamma$ candidates in Continuum Monte Carlo and off-resonance data (red). b.) $B^- \to D^0\pi^-$ Monte Carlo and data compared with $B^+ \to \rho^+\gamma$ candidates in Continuum Monte Carlo and off-resonance data.

1. $\cos\Theta^*_T$, $\cos\Theta_H$, $\cos\Theta^*_B$: these angles are described in Section 4.5

2. Energies E^*_{Ci}: Energy contained in cones in 10° increments in the CMS frame centered on the photon momentum, for a total of 18 energies.

3. R'_2: The ratio of second and zeroth Fox-Wolfram moments in the recoil frame of the photon.

Energy Cones

Additional information on the event topology can be obtained by considering the distribution of the tracks and photons in the event relative to the candidate. For this purpose, we define "Energy Cones": the momentum vector in the CMS frame for each track and photon unassociated with the B candidate are summed in 10 deg intervals ranging from parallel to anti-parallel relative to the photon momentum. The result is eighteen variables E^*_{Ci} that characterize the distribution of energy in the event (excluding the B candidate) relative to the photon momentum in the CMS. The E^*_{Ci} for the signal Monte Carlo are shown in Figure 5.6, while the corresponding

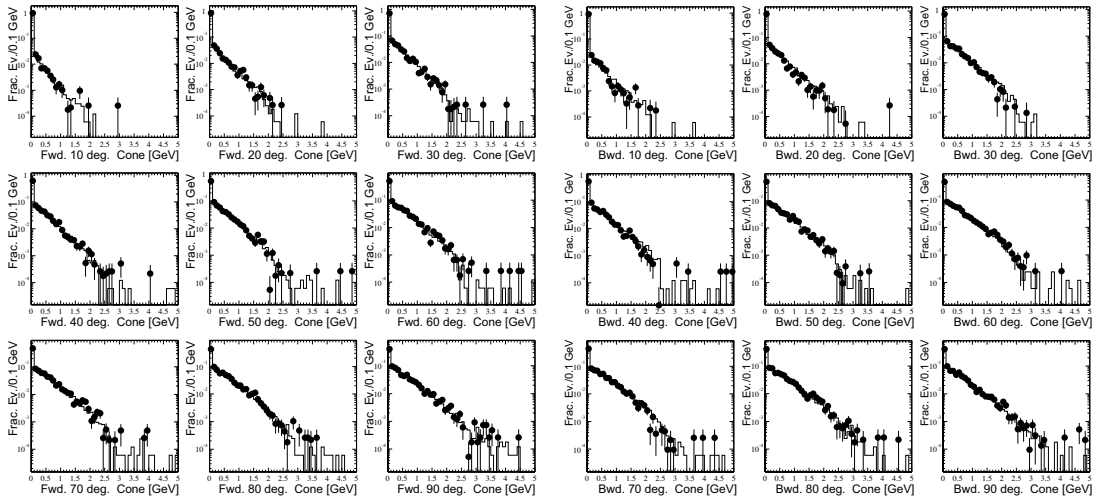

Figure 5.6: E^*_{Ci} for $B^0 \to D^-\pi^+$ events: Monte Carlo(histogram) and Data (points). Left: Forward cones. Right: Backward cones.

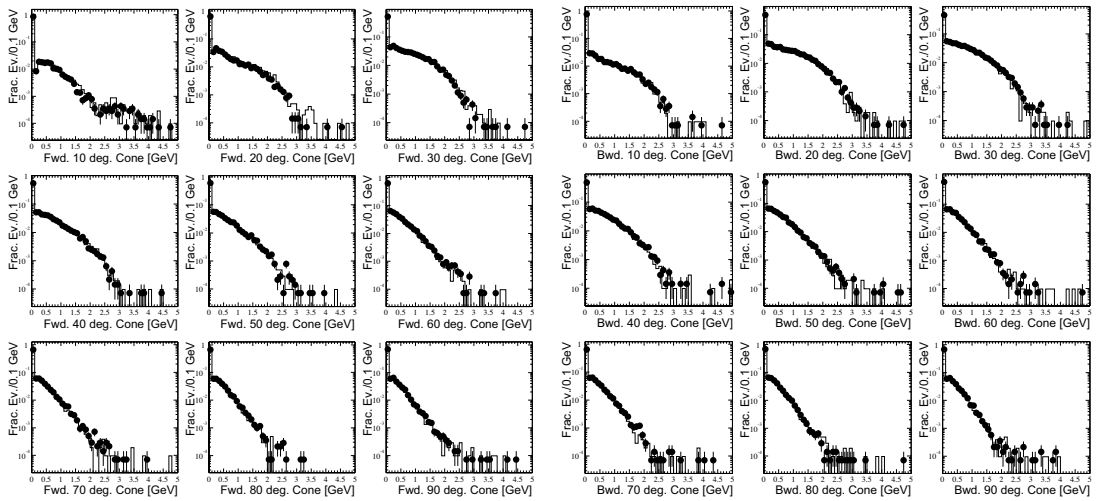

Figure 5.7: E^*_{Ci} for continuum Monte Carlo (histogram) and off-resonance data (points). Left: Forward cones. Right: Backward cones.

distributions from the continuum Monte Carlo compared with off-resonance data are shown in Figure 5.7. The discrimination again comes from the jet-like structure of the continuum background that places more energy in the cones parallel and anti-parallel to the photon versus the more spherical distribution of $B\overline{B}$ events which result in more evenly distributed energy cones.

The off-resonance data and continuum Monte Carlo in good agreement. The signal distribution of the Monte Carlo is checked by comparing the $B \to D\pi$ Monte Carlo with the events reconstructed in this channel in the data. This distribution is shown in Figure 5.6; the Monte Carlo is in good agreement with the data.

The E^*_{Ci} individually carry little information; they must be combined with information from the other cones, in particular the correlations between the cone distributions.

5.3.4 Neural Network

Introduction to Neural Nets

A neural network is used to combine the variables ($\cos\Theta^*_T$, $\cos\Theta^*_B$, $\cos\Theta_H$, 18 cones energies E^*_{Ci}, $|\Delta z|$ (for $B^0 \to \rho^0\gamma$), R'_2 and Flavor) into a single variable to separate the signal and background processes. The basic structure of a neural network is depicted in Figure 5.8. At the bottom of the diagram, event variables x_i enter the network as *input nodes* (red). Linear combinations of these variables are sent to the *hidden nodes* (blue): the jth hidden node receives the linear combination:

$$y_j = \sum a_{ij} x_j \tag{5.3}$$

Each hidden node receives a different linear combination of the input variables. This input is then transformed by an *activation function*, in this case the hyperbolic tangent (tanh) function. The activation function allows the neural network to produce non-linear responses to the input variables.

At each stage, there is *bias node* (violet) which provides a constant output. The bias node is used to set the threshold for the node output.

A linear combination of the output from the hidden nodes $g(y_j)$

$$z = \sum b_j g(y_j) \tag{5.4}$$

is then passed to the *output node* where it is again transformed by an activation function. The mathematical chain from input to output is also shown in Figure 5.8. A neural network can in principle have many hidden layers and output nodes.

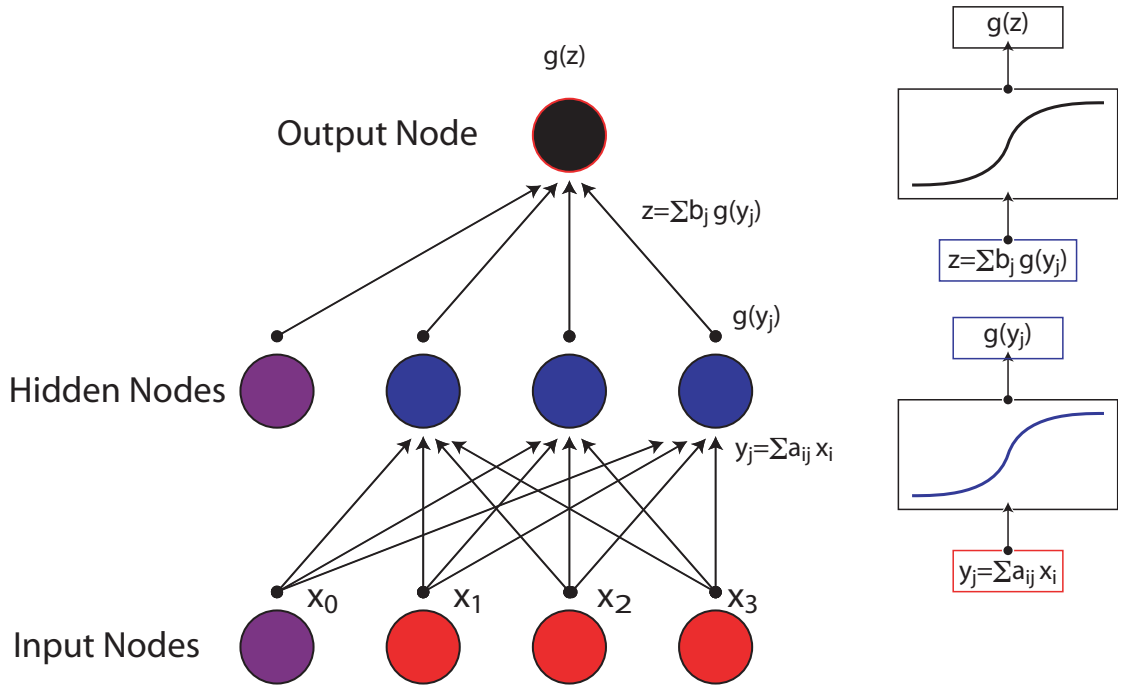

Figure 5.8: Basic structure of a single hidden layer neural network.

Training the Neural Network

The free parameters of the neural network are the coefficients a_{ij} and b_j that are used to form the linear combination of input nodes to the hidden nodes, and the hidden node outputs to the output node, respectively. The optimal set of coefficients are determined by a process known as *back-propagation*. The performance of the neural network for any given set of coefficients is summarized by the sum-squared error (SSE):

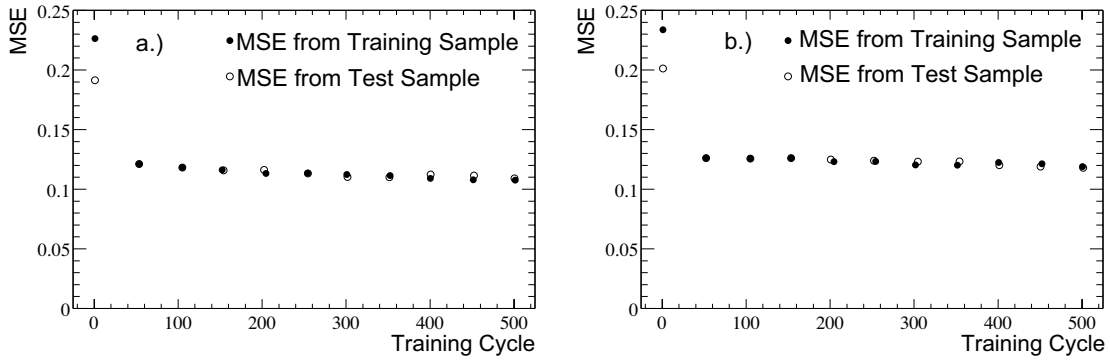

Figure 5.9: MSE (mean squared error) vs. training cycle comparison for the training (solid circles) and test (open circles). a.) the $B^0 \to \rho^0\gamma$ neural network. b.) the $B^+ \to \rho^+\gamma$ neural network.

$$\mathrm{SSE}(a_{ij}, b_j) = \sum_{a=1}^{N} [\mathrm{NN}(\vec{x_a}; a_{ij}, b_j) - F(\vec{x_a})]^2 \tag{5.5}$$

The $\vec{x}_a$ represents the vector of input variables for the event a, $\mathrm{NN}(\vec{x_a}; a_{ij}, b_k)$ is the neural network output for this vector with the coefficients a_{ij} and b_j, and $F(\vec{x_a})$ is the desired output for this vector (e.g. $= 0$, if it is a vector corresponding to a background event, or $= 1$, if it is a signal event). The SSE then represents a "χ^2" for the network configuration that can be minimized in a manner completely analogous to a fit via gradient descent. This describes precisely the function of the back-propagation algorithm: the derivatives of the SSE relative to changes in each of the coefficients are evaluated and the coefficients adjusted accordingly and iteratively to minimize the SSE.

Implementing the Neural Network

The neural network package used for this analysis is the Stuttgart Neural Network Simulator (SNNS)[49][50]. Separate neural networks are implemented and trained for $B^0 \to \rho^0\gamma$ and $B^+ \to \rho^+\gamma$. In both cases, the neural networks have 10 hidden layer nodes and one output node.

Network Training

The network is trained in 500 cycles of back-propagation through half the Monte Carlo signal and continuum background sample with weights updated after every fifty events. The events from signal and background are presented in random order. The resulting network and its output are validated on an independent Monte Carlo sample and data control samples.

The training process is summarized in Figure 5.9. The network performance is quantified by the Mean Squared Error (MSE) defined as:

$$\text{MSE} = \frac{\text{SSE}}{\text{Number of Events}}$$

The MSE is evaluated after each training cycle both for the training sample and an independent sample of Monte Carlo events (the "test" sample). If the MSE in the test sample is considerably higher than the MSE in the training sample, the neural network may have been "overtrained": the neural network has optimized itself on a feature that results from a statistical fluctuation.

In Figure 5.9, the network improves dramatically with only 100 cycles, followed by small improvements beyond. The MSE of the test and training samples are in agreement throughout the training, indicating that no overtraining has occurred.

Neural Network Output:

The neural network output from various samples are shown in Figures 5.10 and 5.11 for $B^0 \to \rho^0\gamma$ and Figures 5.12 and 5.13 for $B^+ \to \rho^+\gamma$. In Figures 5.10 and 5.12, the signal and continuum background outputs are shown. The Monte Carlo expectation for the continuum agree well with the off-resonance data. In order to have a similar validation of the signal output, we evaluate the neural network output from $B^0 \to D^-\pi^+$ events for the $B^0 \to \rho^0\gamma$ neural network and $B^+ \to D^0\pi^+$ for the $B^+ \to \rho^+\gamma$ neural network. The data and Monte Carlo simulation of these samples are shown in Figures 5.11 and 5.13. The neural network output for the data events are in good agreement with the Monte Carlo simulation. The on-resonance sideband

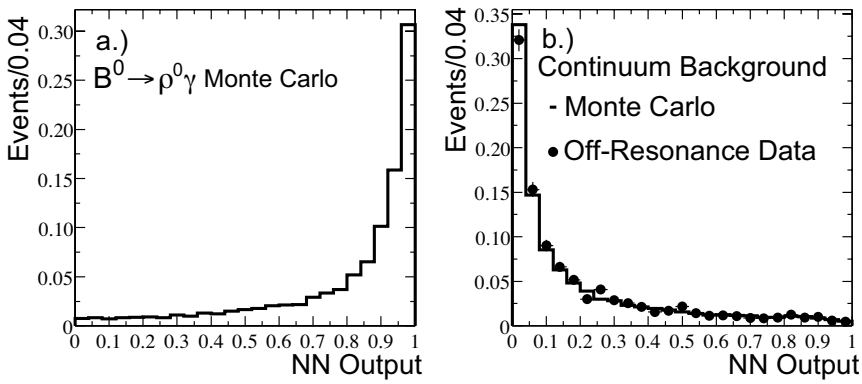

Figure 5.10: $B^0 \to \rho^0\gamma$ neural network output for a.) Signal $B^0 \to \rho^0\gamma$ Monte Carlo. b.) Continuum Monte Carlo and off-resonance data.

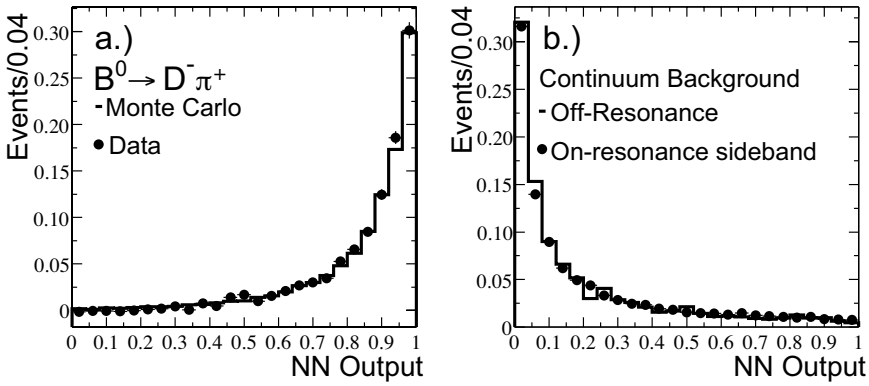

Figure 5.11: $B^0 \to \rho^0\gamma$ neural network output for a.) $B \to D\pi$ Monte Carlo and data and b.) off-resonance data and on-resonance sideband

(events with $M_{ES} < 5.27\,\mathrm{GeV}/c^2$ and $|\Delta E^*| < 0.5\,\mathrm{GeV}$) is compared with the off-resonance data. Here again, the distributions are in good agreement, demonstrating that the presence of $B\overline{B}$ events does not significantly change the distribution of the neural network output.

5.3.5 Background Suppression

The continuum background is suppressed with a selection on the neural network output determined by maximizing the $S^2/(S+B)$. The optimization is performed

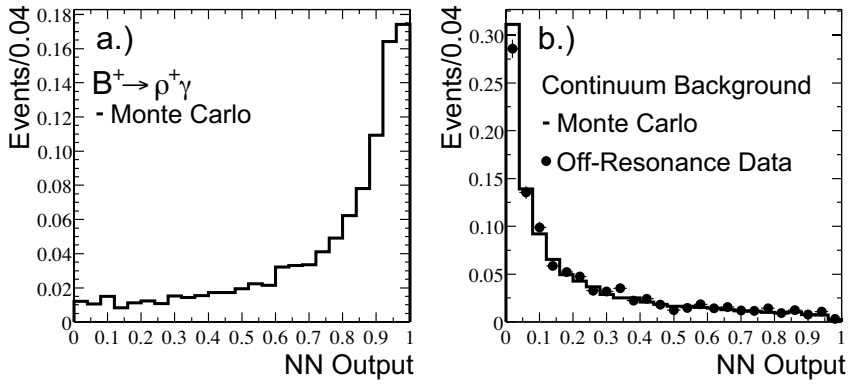

Figure 5.12: $B^+ \to \rho^+\gamma$ neural network output for a.) $B^+ \to \rho^+\gamma$ Monte Carlo and b.) Continuum Monte Carlo and off-resonance data.

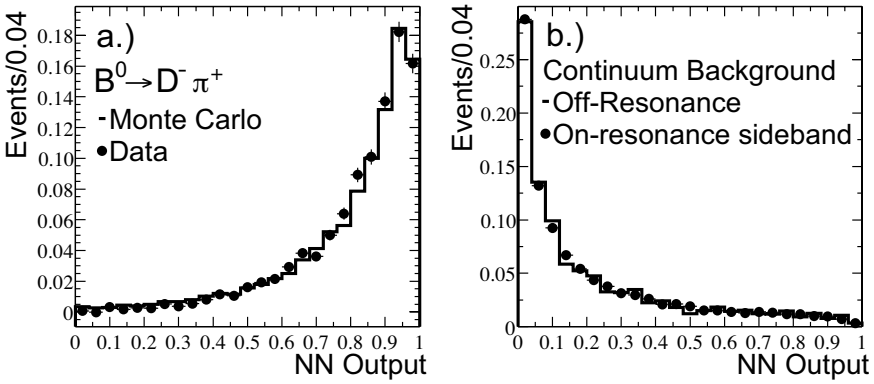

Figure 5.13: $B^+ \to \rho^+\gamma$ neural network output for a.) $B^- \to D^0\pi^-$ Monte Carlo and data and b.) off-resonance data and on-resonance sideband.

assuming that the fit will be performed in the Grand Side Band (GSB) of $m_{\rm ES} = [5.2, 5.3]\,{\rm GeV}/c^2$, $\Delta E^* = [-0.3, 0.3]\,{\rm GeV}$ and $M_{\pi\pi} = [0.520, 1.020]\,{\rm GeV}/c^2$ with $\mathcal{B}[B^0 \to \rho^0\gamma] = 10^{-6}$ and $\mathcal{B}[B^+ \to \rho^+\gamma] = 2 \cdot 10^{-6}$. The predicted signal and background expectations are obtained from the signal and continuum Monte Carlo simulation for $56.2{\rm fb}^{-1}$ of on-resonance data. The background estimates in the signal box are made by scaling the grand sideband yield by the ratio of $\Delta E^* \times m_{\rm ES}$ phase space between signal box and the grand sideband region assuming a flat background distribution. The optimization is shown in Figures 5.14. The maximum value of $S^2/(S+B)$ is obtained by requring the neural network output to be greater than 0.91 and and 0.90

for $B^0 \to \rho^0\gamma$ and $B^+ \to \rho^+\gamma$, respectively. This corresponds to approximately 7.6 signal and 250 continuum background events for $B^0 \to \rho^0\gamma$ and 11.4 signal and 400 continuum background events for $B^+ \to \rho^+\gamma$.

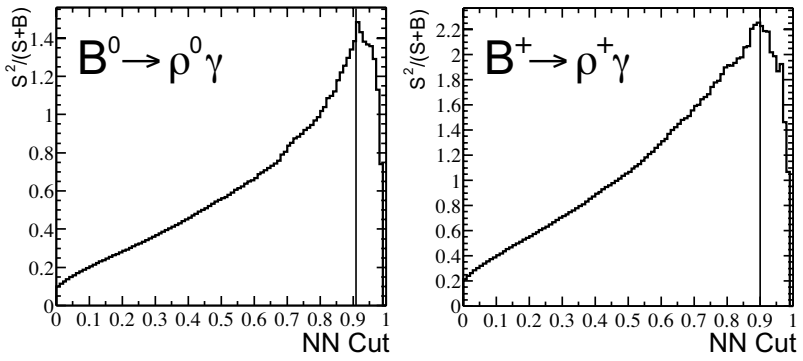

Figure 5.14: $S^2/(S+B)$ optimization of neural network selection for $B^0 \to \rho^0\gamma$ (Left) and $B^+ \to \rho^+\gamma$ (Right). The vertical line indicates the chosen selection.

5.3.6 Helicity Angle Cut

The decay mode $B^+ \to \rho^+\pi^0$ presents a serious background to $B^+ \to \rho^+\gamma$ due to its large expected (though unmeasured) branching fraction of $\sim 2.5 \times 10^{-5}$, an order of magnitude larger than the signal process. The analogous mode $B^0 \to \rho^0\pi^0$ for $B^0 \to \rho^0\gamma$ occurs at much smaller rates ($\sim 1 \times 10^{-6}$) due to color suppression.

The recoil of the vector meson ρ^+ against the pseudoscalar meson π^0 in this decay results in a $\cos^2\Theta_H$ helicity distribution as opposed to the $\sin^2\Theta_H$ distribution for the ρ^+ recoiling against the photon (see Section 4.5.3). While $\cos\Theta_H$ is included in the neural network, the training of the neural network was based on separation of the signal process from the continuum background; there is additional benefit from using $\cos\Theta_H$ explicitly in suppressing the $B^+ \to \rho^+\pi^0$.

Figure 5.15 shows the distribution of the $\cos\Theta_H$ for $B^+ \to \rho^+\pi^0$ and for $B^+ \to \rho^+\gamma$ after the neural network selection. While there is a clear depletion of events at large $\cos\Theta_H$, the $B^0 \to \rho^0\pi^0$ still has a distribution which is enhanced at large $\cos\Theta_H$

relative to the signal process.

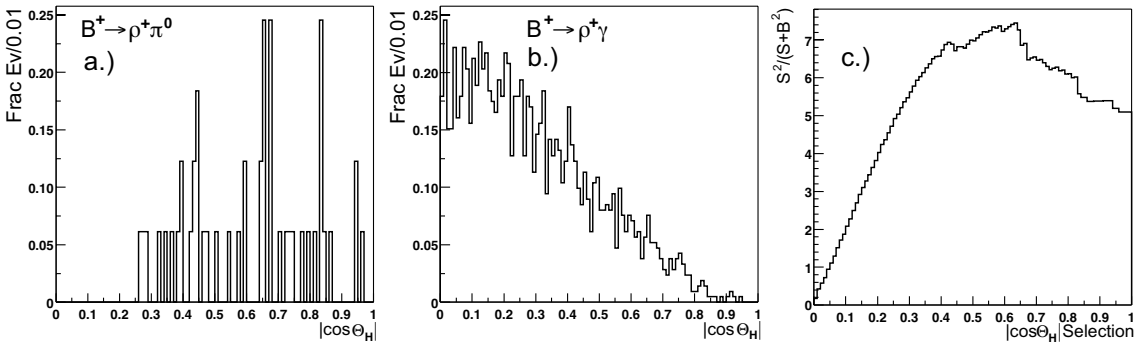

Figure 5.15: Helicity angle distributions of a.) $B^+ \to \rho^+\pi^0$ background and b.) $B^+ \to \rho^+\gamma$ signal *after* the neural network output selection. c.) Optimization of $\cos\Theta_H$ selection.

The current 90% confidence level limit for $B^+ \to \rho^+\pi^0$ from the CLEO collaboration is $\mathcal{B}[B^+ \to \rho^+\pi^0] < 4.2 \times 10^{-5}$ [51]. Since the branching fraction of this process is unknown, the uncertainty in the signal yield due to its contribution scales linearly with the yield of $B^0 \to \rho^+\pi^0$ rather than the square root. As a result, we optimize $\frac{S^2}{S+B^2}$. Figure 5.15 shows the optimization of this variable. Based on this optimization, we select events with $|\cos\Theta_H| < 0.6$.

5.4 Signal Extraction

5.4.1 Event Rates

The expected background rates from Monte Carlo simulation of the generic continuum and $B\overline{B}$ backgrounds and some exclusive decay modes of the $B\overline{B}$ are tabulated in Tables 5.3 and 5.4 for $B^0 \to \rho^0\gamma$ and $B^+ \to \rho^+\gamma$, respectively. The "preselection" columns record the yield of events with a reconstructed B candidate in the region $5.2 < m_{\rm ES} < 5.3\,{\rm GeV}/c^2$ and $-0.3 < \Delta E^* < 0.3\,{\rm GeV}$. For the purposes of comparing how many of these events are close to the signal region of $m_{\rm ES} = 5.28\,{\rm GeV}/c^2$ and $\Delta E^* = 0$, we divide the yield into events in the "signal box" defined as the region $5.27 < m_{\rm ES} < 5.29\,{\rm GeV}/c^2$ and $-0.2 < \Delta E^* < 0.1\,{\rm GeV}$, and the sideband region

Description	Efficiency $(B^0 \to \rho^0\gamma)$	$(B^+ \to \rho^+\gamma)$
Global event selection	0.762	0.745
Photon eeconstruction	0.768	0.759
Track reconstruction	0.831	0.918
Pion Selection	0.671	0.815
π^0 reconstruction	N.A.	0.557
ρ selection	0.844	0.873
B candidate selection	0.924	0.959
Cumulative reconstruction (truth matched)	0.253	0.199
Cumulative reconstruction (all)	0.261	0.233
Background Suppression		
Helicity selection	N.A.	0.866
Neural Network selection	0.471	0.456
Cumulative Efficiency	0.123	0.092

Table 5.2: Reconstruction efficiency for $B \to \rho\gamma$ from Monte Carlo simulation.

which consists of the rest. The numbers are scaled according to the equivalent luminosity of the sample to obtain predictions for the $56.2\,\mathrm{fb}^{-1}$ of data used in this analysis. Additional exclusive decay modes were considered; only those found to contribute more than 0.1 events are shown. Due to the low statistics of the generic continuum background samples, the background expectations in the signal box after the neural network selection (and the $\cos\Theta_H$ selection for $B^+ \to \rho^+\gamma$) were obtained by scaling the sideband yield after the selection by the ratio of the signal box yield and sideband yield before the selection under the assumption that the events after the selection follow a similar distribution.

5.4.2 Signal Extraction Strategy

While the background is predominantly from the continuum, there is a significant contribution from $B\overline{B}$ decays. While we could extract the yield of each background mode, we adopt instead the following simplified strategy for the signal extraction:

Mode	Cross section	Preselection		NN Selection	
		Sideband	Signal Box	Sideband	Signal Box
Continuum					
uds	2.09 nb	11897	1578	161	21.4
$c\overline{c}$	1.35 nb	1737	192	62	6.8
$\tau^+\tau^-$	0.94 nb	2458	281	5	0.6
$B\overline{B}$					
Generic $B^0\overline{B}^0$	0.525 nb	27.7		9.2	0
Generic B^+B^-	0.525 nb	26.5		8.3	0
$B^0 \to K^{*0}\gamma$	22.2 fb	1.8	6.4	0.4	2.6
$B^+ \to K^{*+}\gamma$	20.1 fb	3.8	0.6	0.9	0.2
$B^0 \to X_s^0\gamma$	143 fb	9.1	1.6	2.1	0.7
$B^+ \to X_s^+\gamma$	143 fb	8.4	2.1	1.9	0.9
$B^0 \to \rho^0\pi^0$	0.525 fb	0.2	0.7	0.0	0.2
$B^+ \to \rho^+\pi^0$	13.7 fb	1.2	0.8	0.2	0.1
On-resonance				276	

Table 5.3: Expected backgrounds for $B^0 \to \rho^0\gamma$ in 56.2 fb^{-1} of on-resonance data.

Mode	Cross section	Preselection		NN Selection	
		Sideband	Signal Box	Sideband	Signal Box
Continuum					
uds	2.09 nb	20944.6	2790.7	238.1	31.7
$c\overline{c}$	1.35 nb	4191.2	463.3	98.7	10.9
$\tau^+\tau^-$	0.94 nb	1436.6	134.9	6.8	0.6
$B\overline{B}$					
Generic $B^0\overline{B}^0$	0.525 nb	74		1.8	1.8
Generic B^+B^-	0.525 nb	81		5.0	1.7
$B^0 \to K^{*0}\gamma$	22.2 fb	10.7	2.5	2.6	0.8
$B^+ \to K^{*+}\gamma$	20.1 fb	11.7	5.0	2.6	1.8
$B^0 \to X_s^0\gamma$	143 fb	30.3	5.8	3.5	0.9
$B^+ \to X_s^+\gamma$	143 fb	30.5	10.5	2.6	0.5
$B^0 \to \rho^0\pi^0$	0.525 fb	0.1	0.1	0.0	0.0
$B^+ \to \rho^+\pi^0$	13.7 fb	7.2	13.0	0.6	1.3
On-resonance				306	

Table 5.4: Expected backgrounds for $B^+ \to \rho^+\gamma$ in 56.2 fb^{-1} of data at the $\Upsilon(4S)$ resonance. The expected yields in the last two columns include the $\cos\Theta_H$ selection.

- The yield of signal events will be extracted by an extended maximum likelihood fit in the manner described in Section 4.7 for the $B \to K^*\gamma$, but in the three variables $m_{\rm ES}$, ΔE^* and $M_{\pi\pi}$. This maximizes the sensitivity of the fit by using the full information about the distribution of the signal and background in each variable, rather than making a selection.

- The extraction will only have two components: a signal component, and a continuum component. We assume that all the background, despite the presence of significant backgrounds from $B\overline{B}$ decays, can be adequately described by the continuum distribution. This assumption will be checked by simulating the $B\overline{B}$ backgrounds and assessing any biases in the fitting procedure.

5.4.3 Validation of Signal Extraction Procedure

A study was performed to check the signal extraction procedure, evaluate the sensitivity of the analysis to the signal process, and determine the effect of $B\overline{B}$ backgrounds. In these "toy" Monte Carlo studies, simulated events consisting of values of $m_{\rm ES}$, ΔE^* and M_ρ are randomly generated for the signal and background hypotheses from the probability distribution functions summarized in Tables 5.5 and 5.6 for $B^0 \to \rho^0\gamma$ and $B^+ \to \rho^+\gamma$, respectively. Figures 5.16 and 5.17 show the distributions from the off-resonance data used to obtain the background parameterizations.
Events for the combined signal and background distribution are generated according to the expected signal and background yields given in Table 5.3 and 5.4, resulting in a simulated "experiment" representing a possible outcome of the data. The actual number of generated events for each hypothesis is allowed to vary according to Poisson statistics.
Each experiment is fit to the three-dimensional probability density function of signal and background composed of the product of $m_{\rm ES}$, ΔE^* and $M_{\pi\pi}$ distributions for the signal and background hypotheses to determine the signal and background yield. The signal description is identical to the generator: the same parameterizations and parameters are used. For the background, the same functional parameterizations as the generator are used, but the parameters are allowed to vary in the fit, with the

$B^0 \to \rho^0\gamma$ Signal		
$m_{\rm ES}$	Gaussian	$\mu = 5.280\,{\rm GeV}/c^2$, $\sigma = 2.5\,{\rm MeV}/c^2$
ΔE^*	Crystal Ball	$\mu = -11.0\,{\rm MeV}$, $\sigma = 43.6\,{\rm MeV}$
		$\alpha = 0.981$, $\beta = 0.912$
$M_{\pi\pi}$	Breit-Wigner	$m_0 = 767\,{\rm MeV}/c^2$, $\Gamma = 155\,{\rm MeV}/c^2$
$B^0 \to \rho^0\gamma$ Background		
$m_{\rm ES}$	ARGUS Threshold	$\zeta = -54.0$
ΔE^*	2nd order polynomial	$p_1 = -1.0$, $p_2 = 0.30$
$M_{\pi\pi}$	Breit-Wigner+linear	$m_0 = 767\,{\rm MeV}/c^2$, $\Gamma = 155\,{\rm MeV}/c^2$,
		$p_1 = -0.48$, Fraction=0.205

Table 5.5: Parameterizations used for $m_{\rm ES}$, ΔE^*, $M_{\pi\pi}$ signal extraction studies in the $B^0 \to \rho^0\gamma$ analysis.

$B^+ \to \rho^+\gamma$ Signal		
$m_{\rm ES}$	Crystal Ball	$\mu = 5.2793\,{\rm GeV}/c^2$, $\sigma = 2.5\,{\rm MeV}/c^2$
		$\alpha = 1.12$, $\beta = 2.4$
ΔE^*	Crystal Ball	$\mu = -29.0\,{\rm MeV}$, $\sigma = 57.0\,{\rm MeV}$
		$\alpha = 0.68$, $\beta = 7.0$
$M_{\pi\pi}$	Breit-Wigner	$m_0 = 767\,{\rm MeV}/c^2$, $\Gamma = 157\,{\rm MeV}/c^2$
$B^+ \to \rho^+\gamma$ Background		
$m_{\rm ES}$	ARGUS Threshold	$\zeta = -53.3$
ΔE^*	2nd order polynomial	$p_1 = -1.2$, $p_2 = -0.4$
$M_{\pi\pi}$	Breit-Wigner+linear	$m_0 = 767\,{\rm MeV}/c^2$, $\Gamma = 157\,{\rm MeV}/c^2$,
		$p_1 = -0.64$, Fraction=0.12

Table 5.6: Parameterizations used for $m_{\rm ES}$, ΔE^*, $M_{\pi\pi}$ signal extraction studies in the $B^+ \to \rho^+\gamma$ analysis.

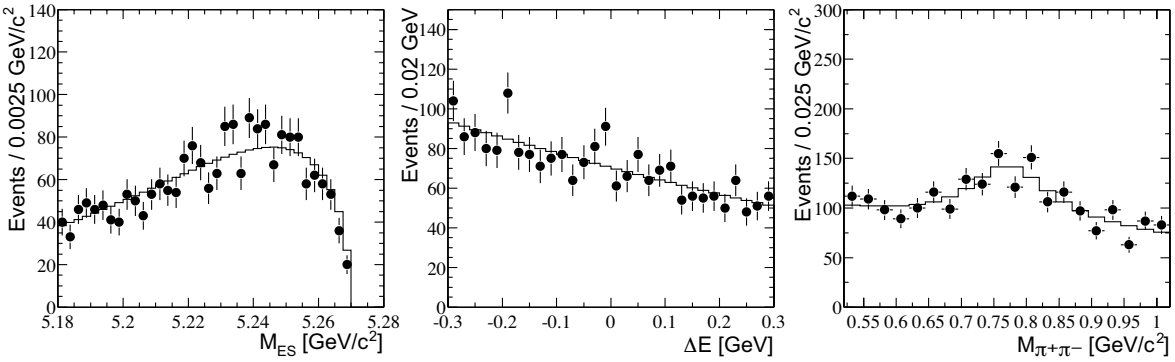

Figure 5.16: $m_{\rm ES}$, ΔE^*, $M_{\pi\pi}$ distributions for $B^0 \to \rho^0\gamma$ candidates in the off-resonance data.

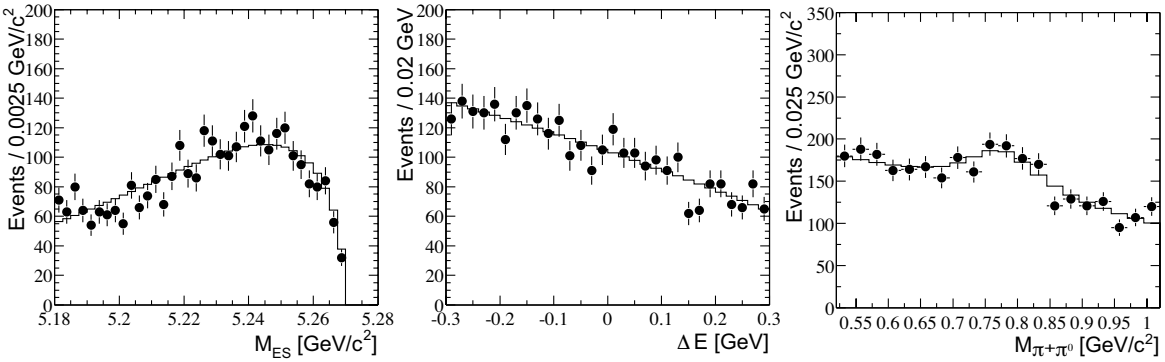

Figure 5.17: $m_{\rm ES}$, ΔE^*, and $M_{\pi\pi}$ distributions for $B^+ \to \rho^+\gamma$ candidates in the off-resonance data.

exception of the ρ resonance fraction in the $M_{\pi\pi}$ distribution, which is fixed. The systematic uncertainties due to the fixed parameters is determined in Section 5.5.1. In the first stage of the studies, we generate only signal and continuum background events in each experiment, so that the generated and fitted distributions are consistent. Later, we explore the effects of $B\overline{B}$ backgrounds. Table 5.7 summarizes the mean number of generated signal and background events, the number of generated background events and the mean error on the signal yield returned by the fit.

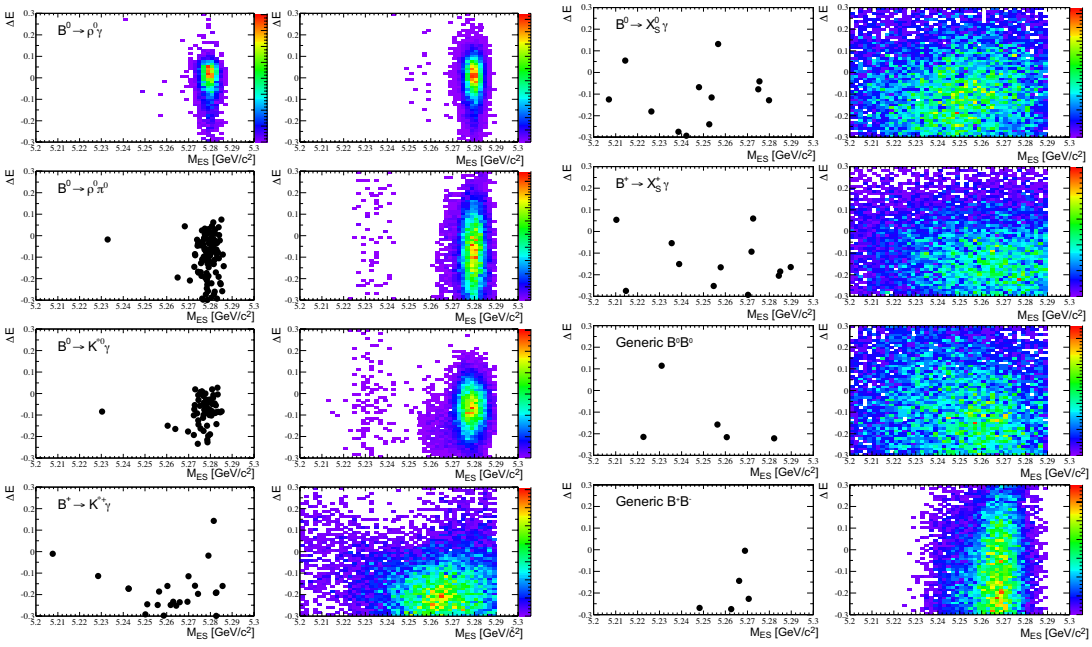

Figure 5.18: ΔE^* vs. $m_{\rm ES}$ distribution for $B^0 \to \rho^0\gamma$ candidates in $B\overline{B}$ background Monte Carlo simulations. The left plot of each pair shows the raw distribution and the right shows 10,000 events generated from a non-parameteric model.

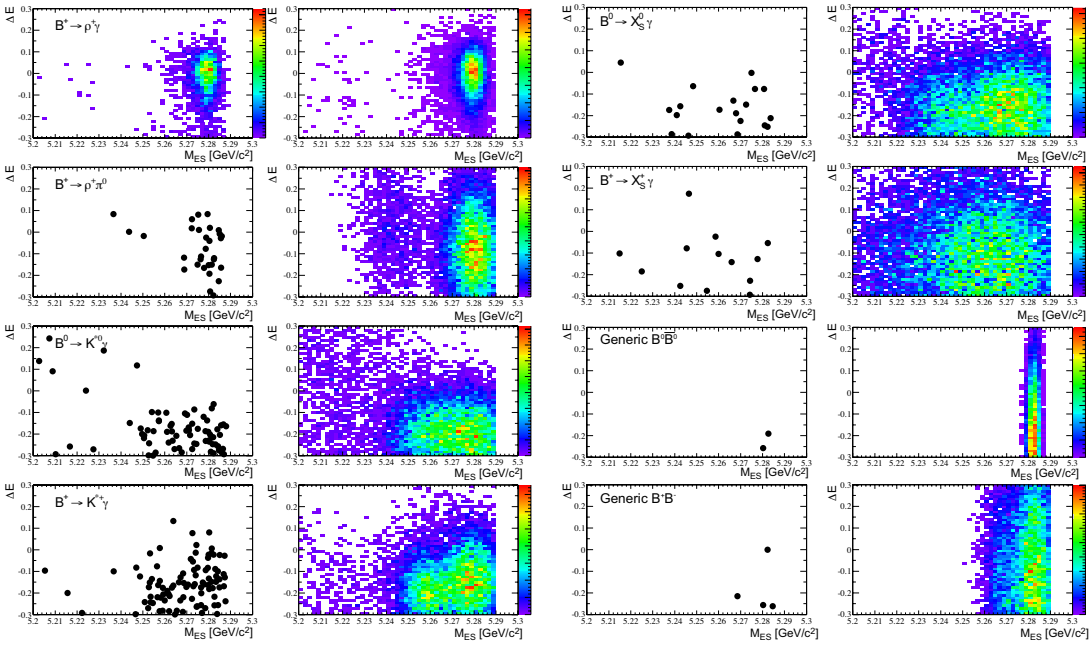

Figure 5.19: ΔE^* vs. $m_{\rm ES}$ distribution for $B^+ \to \rho^+\gamma$ candidates in $B\overline{B}$ background Monte Carlo simulations. The left plot of each pair shows the raw distribution and the right shows 10,000 events generated from a non-parameteric model.

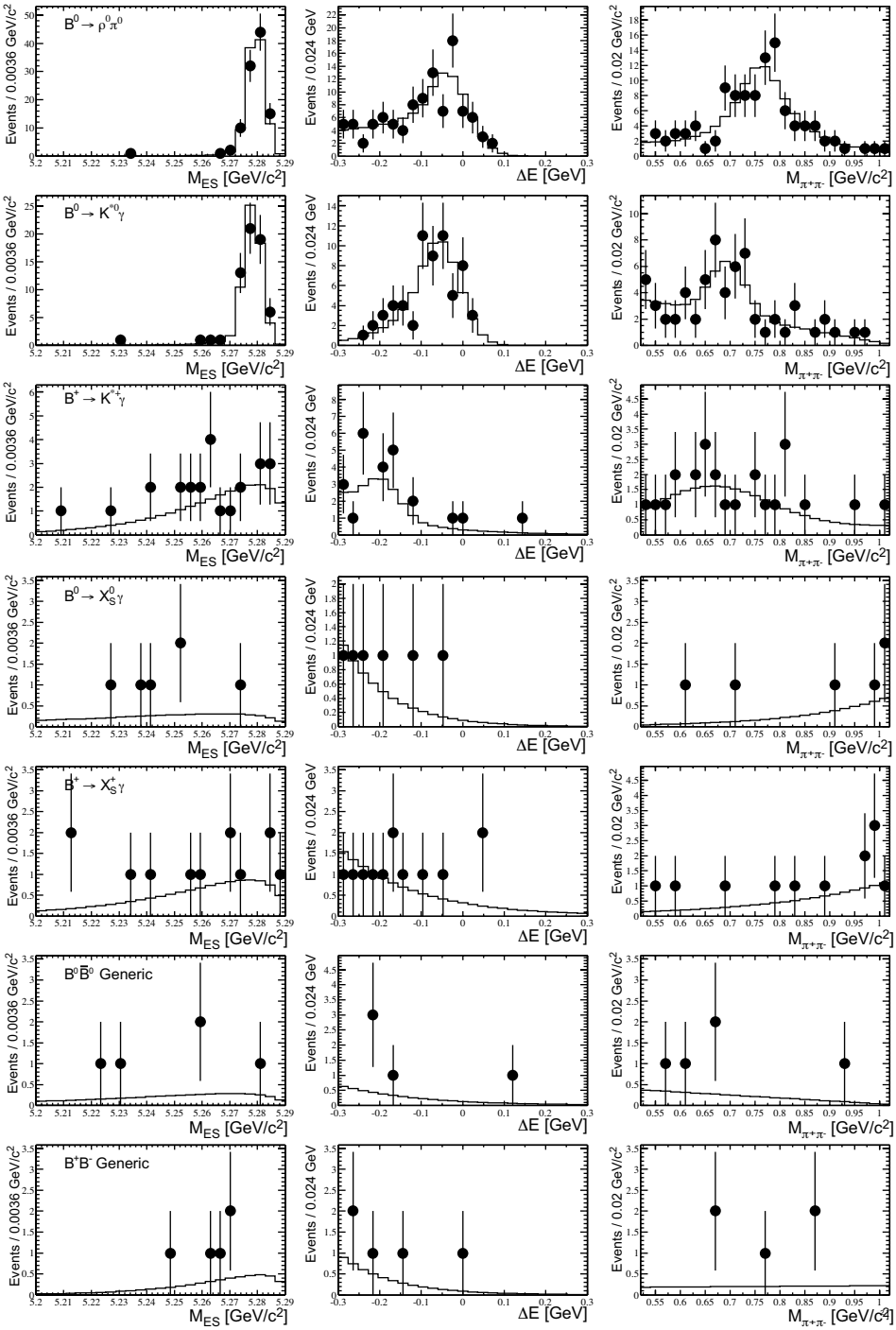

Figure 5.20: $m_{\rm ES}$, ΔE^*, $M_{\pi\pi}$ projections for $B^0 \to \rho^0\gamma$ background candidates in Monte Carlo-simulated $B\overline{B}$ events.

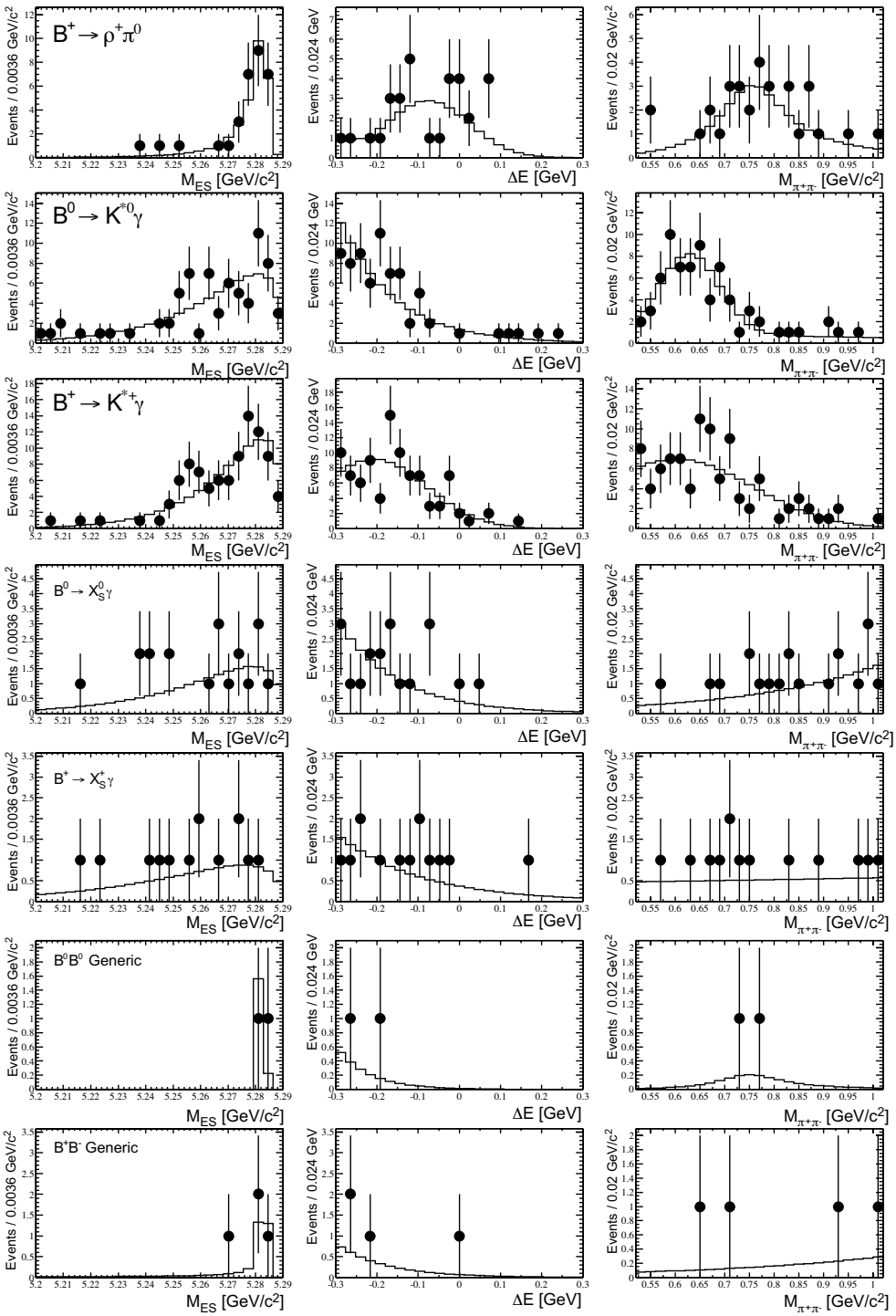

Figure 5.21: $m_{\rm ES}$, ΔE^*, M_ρ projections for $B^+ \to \rho^+\gamma$ background candidates in Monte Carlo-simulated $B\overline{B}$ events.

	Expected N_S	N_B	$\langle \delta N_S \rangle$	$\delta N_S / N_S$
$B^0 \to \rho^0 \gamma$	7.6	250	4.4	0.57
$B^+ \to \rho^+ \gamma$	11.4	375	6.1	0.54

Table 5.7: Mean number of generated events, fitted yield and error and relative error for a toy Monte Carlo study for $B^0 \to \rho^0\gamma$ and $B^+ \to \rho^+\gamma$ with no $B\overline{B}$ backgrounds.

5.4.4 B decay backgrounds:

The study of the signal extraction procedure thus far assumes that the background is entirely continuum and ignores backgrounds from $B\overline{B}$ decays which are distributed differently in $m_{\rm ES}$, ΔE^* and $M_{\pi\pi}$. We simulate the presence of these backgrounds with two models:

- The ΔE^* vs. $m_{\rm ES}$ distribution of these background is modeled two dimensions using the Keys non-parametric model[52].This model simulates the distribution as a sum of two-dimensional Gaussian distributions centered at each ΔE^* vs. $m_{\rm ES}$ point. The $M_{\pi\pi}$ is modeled independently from a functional parameterization.

- Each variable is parameterized independently.

The ΔE^* vs. $m_{\rm ES}$ distributions for these events are shown in Figures 5.18 and 5.19 together with their KEYS representation. The parameterized one-dimensional projections are shown in Figures 5.20 and 5.21. The difference in the observed bias between these two models is taken as a systematic uncertainty.

We simulate uncertainties in the background rates by considering the possibility of an underestimated kaon misidentification rate by doubling the $b \to s\gamma$ background rates, as well as enhancing the $B^+ \to \rho^+\pi^0$ rate to the upper limit of $\mathcal{B}[B^+ \to \rho^+\pi^0] < 4.2 \times 10^{-5}$ established by the CLEO collaboration.

The observed signal yields are shown in Figure 5.22 and 5.23 for $B^0 \to \rho^0\gamma$ and Figure 5.24 and Figure 5.25 for $B^+ \to \rho^+\gamma$. For the $B^0 \to \rho^0\gamma$, the biases range from -0.5 events to 0.8 events. For the $B^+ \to \rho^+\gamma$, the biases range from -0.1 to 2.0 events. In both case, we take the full range of values as the systematic uncertainty

due to biases from B decay backgrounds.

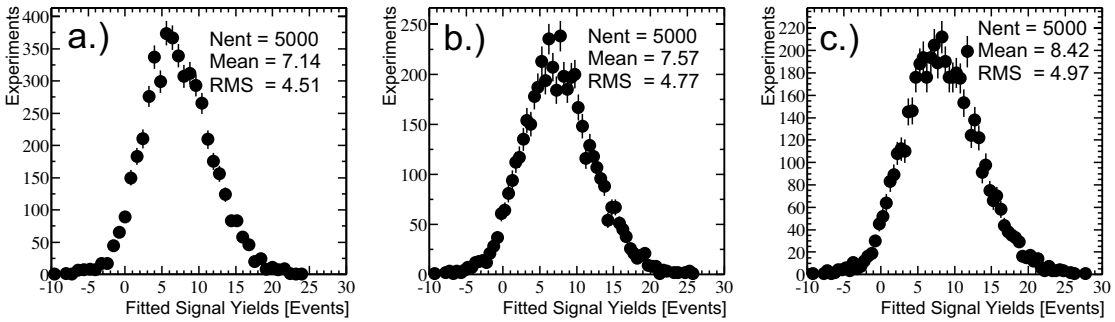

Figure 5.22: Fitted signal yields for $B^0 \to \rho^0\gamma$ with B decay backgrounds modeled using KEYS for ΔE^* and $m_{\rm ES}$: a.) No B backgrounds, b.) B backgrounds at nominal Monte Carlo rates, c.) B backgrounds with $b \to s\gamma$ rates doubled.

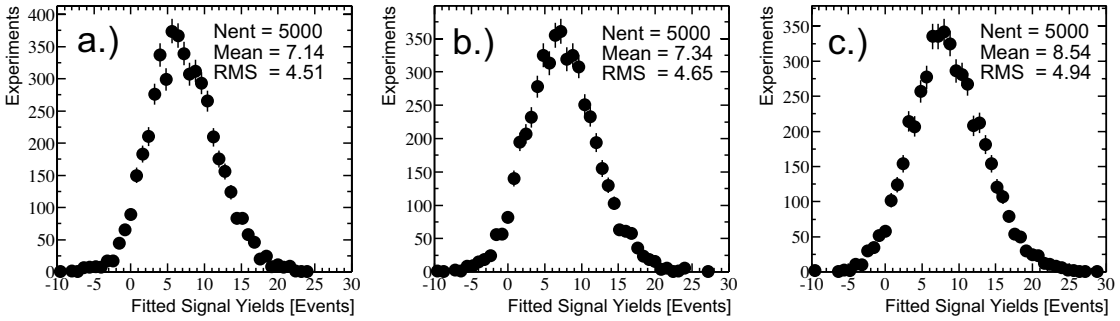

Figure 5.23: Fitted signal yields for $B^0 \to \rho^0\gamma$ with B decay backgrounds modeled by one-dimensional parameterizations in $m_{\rm ES}$, ΔE^* and $M_{\pi\pi}$: a.) No B backgrounds, b.) B backgrounds at nominal Monte Carlo rates, c.) B backgrounds with $b \to s\gamma$ rates doubled.

5.5 Systematic Studies of PDF Parameterzations:

In the previous Monte Carlo studies, the signal distributions were assumed to be known perfectly: the parameters of the fitted distributions are fixed in the fit to the values used in the generation. This is also the case with the $M_{\pi\pi}$ resonant fraction in the background. In practice, these parameters carry uncertainties which result in

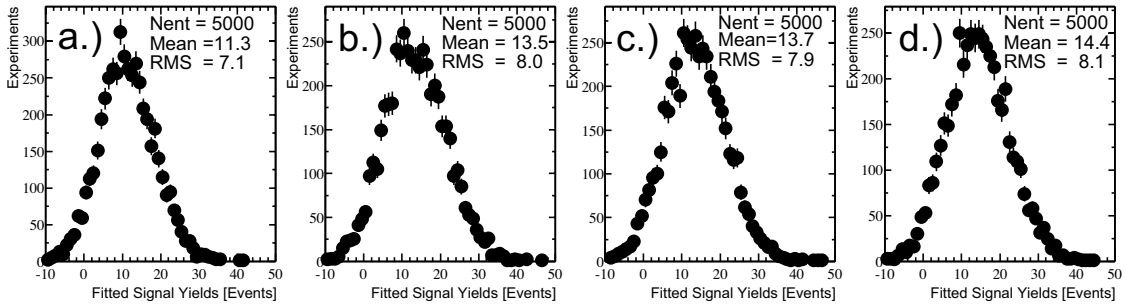

Figure 5.24: Fitted signal yields for $B^+ \to \rho^+\gamma$ with B decay backgrounds modeled with ΔE^* and $m_{\rm ES}$ modeled with KEYS: a.) No B backgrounds, b.) B backgrounds at nominal Monte Carlo rates, c.) B backgrounds with $b \to s\gamma$ rates doubled, and d.) B backgrounds with $B^+ \to \rho^+\pi^0$ rate increased to $\mathcal{B}[B^+ \to \rho^+\pi^0] = 4.3 \times 10^{-5}$.

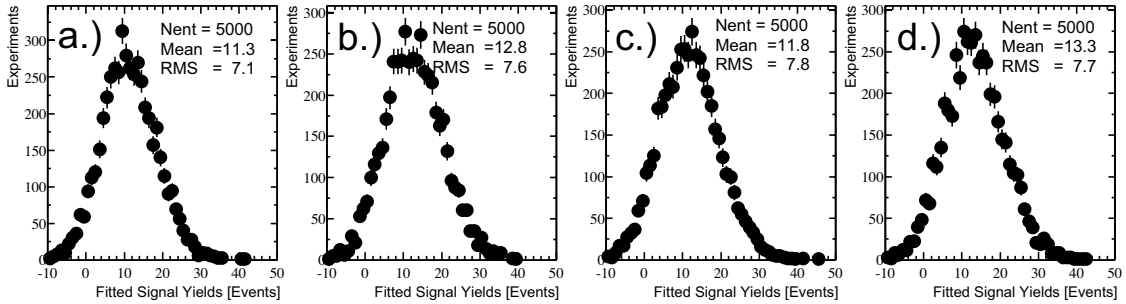

Figure 5.25: Fitted signal yields for $B^+ \to \rho^+\gamma$ with B decay backgrounds modeled with one-dimensional parameterization in $m_{\rm ES}$, ΔE^* and $M_{\pi\pi}$: a.) No B backgrounds, b.) B backgrounds at nominal Monte Carlo rates, c.) B backgrounds with $b \to s\gamma$ rates doubled, and d.) B backgrounds with $B^+ \to \rho^+\pi^0$ rate increased to $\mathcal{B}[B^+ \to \rho^+\pi^0] = 4.3 \times 10^{-5}$.

systematic uncertainties on the extracted signal for each parameter fixed in the fit. These uncertainties may be estimated by cross-checking the parameters in data control samples and varying the fixed parameters within the uncertainties. We obtain the range of reasonable values for each parameter from the appropriate $B \to K^*\gamma$ control channels. By varying each of these parameters according to these ranges, we obtain the systematic uncertainty on the signal yield.

For the background parameters, the largest sample of continuum background occurs within the on-resonance data itself. Thus, we allow the background parameters to

float (with the exception of the resonant fraction in the $M_{\pi\pi}$) and incorporate the uncertainty of these parameters into the statistical uncertainty in the yield determined by the fit.

5.5.1 Uncertainties from Fixed Parameters

We identify the following fixed signal probability distribution function parameters which may introduce systematic error due to uncertainty in their values:

- $m_{\rm ES}$: The width of the signal $m_{\rm ES}$ distribution (resolution).
- ΔE^*: The peak position and width of the signal ΔE^* distribution.
- $M_{\pi\pi}$: The fraction of ρ resonance contribution to the continuum $M_{\pi\pi}$ distribution.

We obtain the range of uncertainty for the $m_{\rm ES}$ and ΔE^* parameters from the $B^0 \to K^{*0}\gamma$ and $B^+ \to K^{*+}\gamma$ shown in Figure 5.26. For the resonant fraction, we use the off-resonance data. The parameters in the signal extraction are then offset from the values used in the generation to determine any bias in the extracted signal yield. The parameters from the $B \to K^*\gamma$ data, the parameter variations and the resulting fractional offset in the mean fitted signal yield are summarized in Table 5.8. Each study has a statistical precision of approximately 1.0%. In cases where the variations are smaller than this uncertainty, 1.0% is taken as the systematic uncertainty. Based on the variations seen in the study, we conservatively assign a 5% systematic on the signal yield for $B^0 \to \rho^0\gamma$ and 10% to $B^+ \to \rho^+\gamma$ due to uncertainties in these parameters. In each case, the range covers the sum in quadrature of all the observed observations (2.4% for $B^0 \to \rho^0\gamma$ and 7.0% for $B^+ \to \rho^+\gamma$).

5.5.2 Systematic Error on the Neural Network Selection

The efficiency of the neural network output selection for both modes is cross-checked using the $B \to D\pi$ decays as control samples. For this purpose, we use the $B^0 \to D^-\pi^+$ decays to study the selection $B^0 \to \rho^0\gamma$, and $B^- \to D^0\pi^-$ for $B^+ \to \rho^+\gamma$

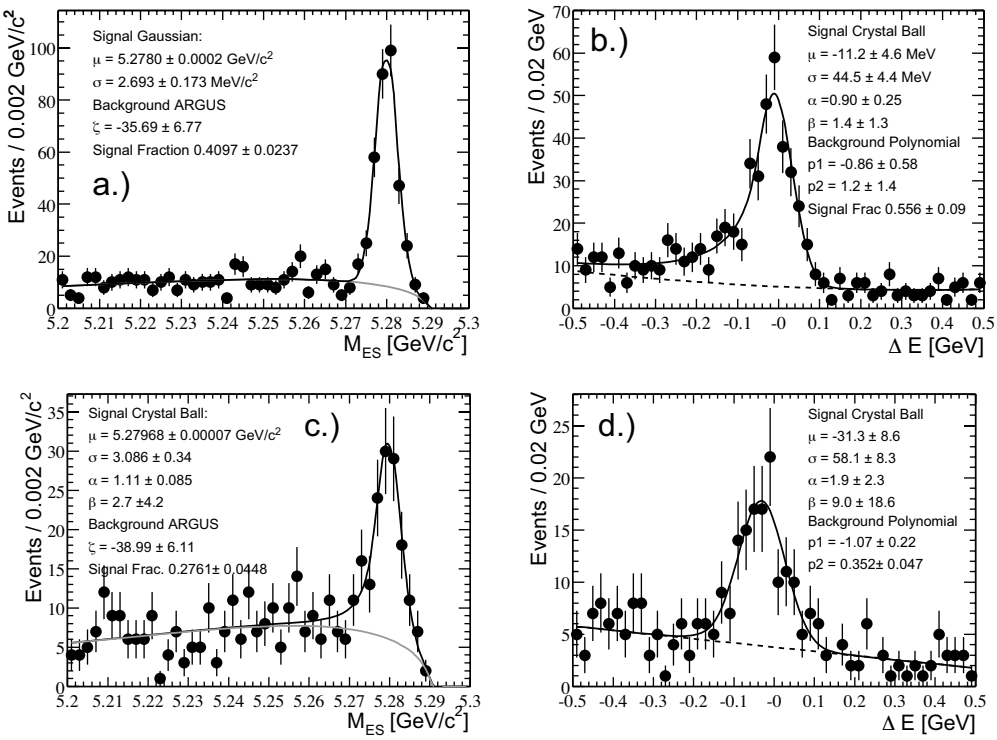

Figure 5.26: Fitted distributions of a.) $m_{\rm ES}$ and b.) ΔE^* for $B^0 \to K^{*0}\gamma$, and c.) $m_{\rm ES}$ and d.) ΔE^* for $B^+ \to K^{*+}\gamma$.

decays. To obtain a systematic uncertainty, we compare the efficiency for the signal Monte Carlo to the control samples in both the data and the Monte Carlo simulation for events with neural network output greater than 0.9. The largest discrepency between these three samples is taken as the systematic uncertainty. While we do not expect the neural network behavior of the control samples to be exactly the same as the signal processes (for example, due to different different helicity structure of the meson decays), we conservatively take any difference as a systematic uncertainty. Based on the results tabulated in Table 5.9 we assign a relative systematic uncertainty of 8% and 6% for the neural network selection in $B^0 \to \rho^0\gamma$ and $B^+ \to \rho^+\gamma$, respectively. The efficiencies tabulated here are somewhat different from those in Table 5.2 due to the fact that the helicity requirement is not applied in the $B^+ \to \rho^+\gamma$ and that the selection is slightly different for $B^0 \to \rho^0\gamma$.

$B^0 \to \rho^0\gamma$	$B^0 \to K^{*0}\gamma$ Fit	Parameter Variation	Fitted Yield Variation (%)
$m_{\rm ES}$ Width	$2.69 \pm 0.17\,{\rm MeV}/c^2$	$\pm 0.2\,{\rm MeV}/c^2$	$+0.05/-0.08$
ΔE^* Peak	$-11.0 \pm 4.1\,{\rm MeV}$	$\pm 5.0\,{\rm MeV}$	$-0.3/+1.4$
ΔE^* Width	$44.5 \pm 4.4\,{\rm MeV}$	$\pm 5.0\,{\rm MeV}$	$-0.2/+0.2$
$M_{\pi\pi}$ Res. Frac.	0.205 ± 0.045	± 0.05	$+1.4/-0.3$

$B^+ \to \rho^+\gamma$	$B^+ \to K^{*+}\gamma$ Fit	Parameter Variation	Fitted Yield Variation (%)
$m_{\rm ES}$ Width	$3.09 \pm 0.34\,{\rm MeV}/c^2$	$\pm 0.34\,{\rm MeV}/c^2$	$+3.3/-5.3$
ΔE^* Peak	$-31.2 \pm 8.6\,{\rm MeV}$	$\pm 8.6\,{\rm MeV}$	$-1.5/+2.2$
ΔE^* Width	$58.1 \pm 8.3\,{\rm MeV}$	$\pm 8.3\,{\rm MeV}$	$-2.2/-1.0$
$M_{\pi\pi}$ Res. Frac.	0.120 ± 0.020	± 0.02	$+3.4/-2.3$

Table 5.8: Signal probability distribution function parameters obtained from $B \to K^*\gamma$ control samples and systematic uncertainties on the average signal yield resulting from variations on parameters.

Mode	$B \to \rho\gamma$ MC	$B \to D\pi$ MC	$B \to D\pi$ Data
$B^0 \to \rho^0\gamma$	$52.5 \pm 1.7\%$	$53.5 \pm 1.1\%$	$56.5 \pm 0.5\%$
$B^+ \to \rho^+\gamma$	$39.7 \pm 1.6\%$	$41.5 \pm 0.9\%$	$42.0 \pm 0.6\%$

Table 5.9: Efficiency for the neural network selection for the signal $B \to \rho\gamma$ Monte Carlo and $B \to D\pi$ control samples in Monte Carlo and data.

5.5.3 Consistency Check: $B \to K^*\gamma$

As a final consistency check, we can look at an orthogonal subspace of events based on the particle identification requirements. For the $B^0 \to \rho^0\gamma$, the relevant sample are those events for which one track passes the pion selection and one fails. For the $B^+ \to \rho^+\gamma$, the sample consists of events where the pion track fails the pion selection. We expect these events to be populated heavily by the $B^0 \to K^{*0}\gamma,\ K^{*0} \to K^+\pi^-$ in the first case, and $B^+ \to K^{*+}\gamma,\ K^{*+} \to K^+\pi^0$ in the latter. We run the entire analysis on the $B \to K^*\gamma$ Monte Carlo with the identical selection criteria up to the particle identification to obtain efficiencies and probability distribution functions for the $B \to K^*\gamma$. We then fit these samples in the on-resonance data to check that

	Efficiency (%)	Fitted Yield (Events)	Expected Yield (Events)
$B^0 \to K^{*0}\gamma$	9.3	238.6 ± 17.3	243 ± 26
$B^+ \to K^{*+}\gamma$	3.26	73.5 ± 11.2	77 ± 13

Table 5.10: Results of signal extraction procedure on $B \to K^*\gamma$-enhanced sample with comparison to the expected yield based on the measured branching fractions and efficiencies predicted by the Monte carlo simulation.

the yield obtained is consistent with the known branching fractions and efficiencies. This procedure cross checks the entire analysis chain up to the particle identification requirements.

The $m_{\rm ES}$, ΔE^* and $M_{\pi^+\pi^-}$ distributions for the two $B \to K^*\gamma$ modes are shown in Figure 5.27. Since the kaon mass hypothesis is not applied to the meson reconstruction (the kinematics and mass are calculated as a $\pi\pi$ combination), the ΔE^* and $M_{\pi\pi}$ are offset to lower values and distorted from what is expected for a properly reconstructed $B \to K^*\gamma$ candidate.

The corresponding on-resonance data is shown in Figure 5.28. A clear cluster of events can be seen at the B mass ($5.28\,{\rm GeV}/c^2$), with the expected negative offset in the ΔE^*. The fitted and expected yields are shown in Table 5.10. The observed yields are in agreement with the expectations.

Systematic Uncertainty Selection Criteria	$B^0 \to \rho^0\gamma$ (%)	$B^+ \to \rho^+\gamma$ (%)
B Count	1.14	1.14
γ Eff.	1.5	1.5
π^0 Eff.	N/A	5.0
π^0/η Veto	1.0	1.0
γ Dist Cut	2.0	2.0
Tracking Eff.	2.4	1.3
π Selection	6.0	3.0
Neural Network	8.0	6.0
Fit Distributions	5.0	10.0
Total	11.8%	13.4%

Table 5.11: Summary of systematic errors for $B \to \rho\gamma$

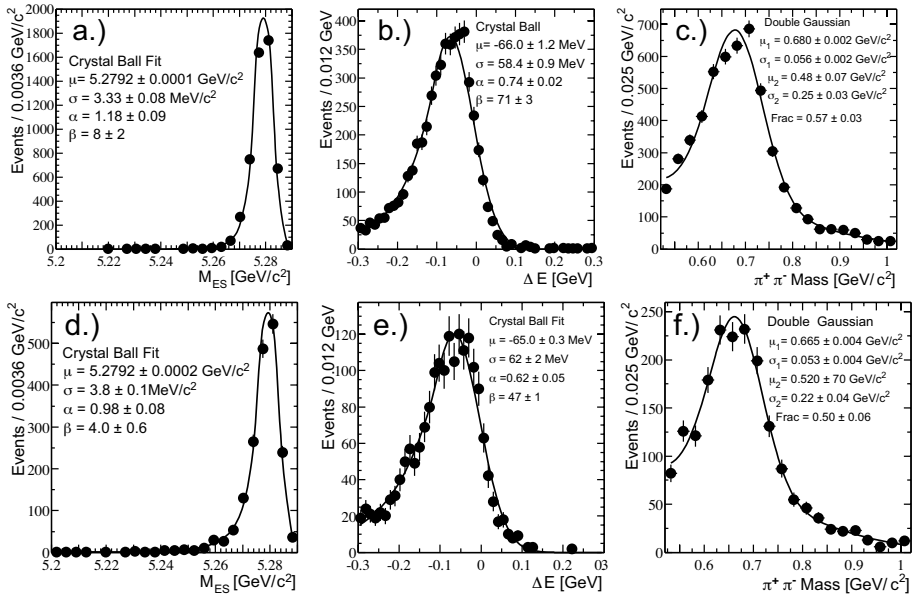

Figure 5.27: Parameterized distributions of a.) $m_{\rm ES}$, b.) ΔE^* and c.) $M_{\pi\pi}$ for $B^0 \to K^{*0}\gamma$ Monte Carlo and d.) $m_{\rm ES}$, ΔE^* and $M_{\pi\pi}$ for $B^+ \to K^{*+}\gamma$ Monte Carlo.

5.5.4 Summary of Systematic Uncertainties

Table 5.11 summarizes the systematic uncertainties in the reconstruction efficiency for $B \to \rho\gamma$. Many of the systematic uncertainties overlap with the $B \to K^*\gamma$ analysis due to the common photon reconstruction and identical topology of the events. The differences are primarily in the efficiency of the neural network selection and the resolution uncertainties. The latter have been translated into uncertainties in the fit distributions used in the signal extraction.

Mode	Yield Events	90% C.L. Yield Events	Bias Events	Efficiency (%)
$B^0 \to \rho^0\gamma$	3.1 ± 4.2	9.5	[-0.5,0.8]	12.3
$B^+ \to \rho^+\gamma$	4.6 ± 5.8	13.5	[-0.1,2.0]	9.2

Table 5.12: The fitted yields, biases from $B\overline{B}$ backgrounds, reconstruction efficiencies for $B^0 \to \rho^0\gamma$ and $B^+ \to \rho^+\gamma$.

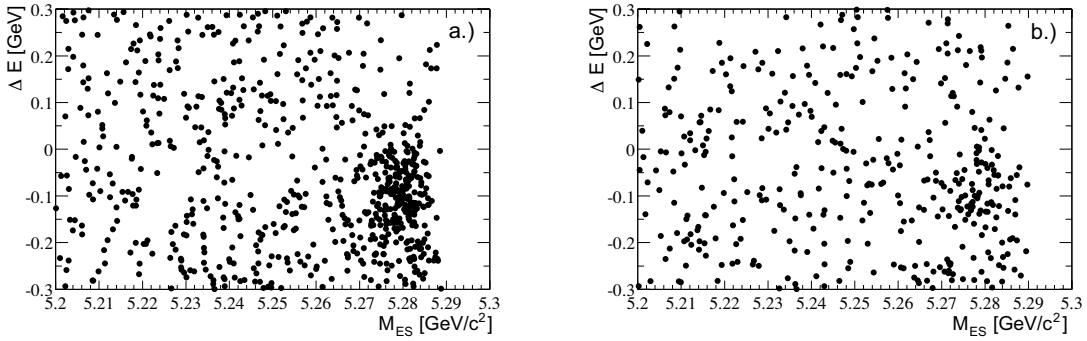

Figure 5.28: Distributions of ΔE^* vs. $m_{\rm ES}$ for $B \to K^*\gamma$-enhanced sampled in the on-resonance data. a.) $B^0 \to \rho^0\gamma$ candidates in which one fails the pion selection, b.)$B^+ \to \rho^+\gamma$ candidates in which the charged pion candidate fails the pion selection.

5.6 Results

Before unblinding the signal yield, the fit is performed to obtain the $-\log\mathcal{L}$ value of the fit without disclosing any of the parameters. The results are compared to the distributions from the toy Monte Carlo exeriments, as shown in Figure 5.29. In the toy Monte Carlo experiments, the events are actually generated from the parameterizations; the distribution of $-\log\mathcal{L}$ from these experiments represents the quality of fit from a sample of experiments where the fit parameterizations perfectly describe the data. The comparison shows that the $-\log\mathcal{L}$ values in the data are consistent with the range expected from the toy Monte Carlo experiments, indicating that the data set is well-modeled by the fit hypotheses.
The unblinded ΔE^* vs. $m_{\rm ES}$ distributions are shown in Figure 5.30. There is no visible evidence for a signal. The fitted yields are:

- $B^0 \to \rho^0\gamma$: 3.1 ± 4.2 Events
- $B^+ \to \rho^+\gamma$: 4.6 ± 5.8 Events

The $m_{\rm ES}$ and ΔE^* projections in the signal region defined by $\Delta E^* = [-0.2, 0.1]$ GeV for the $m_{\rm ES}$ projection and $m_{\rm ES} > 5.27\,{\rm GeV}/c^2$ for ΔE^* projection are shown in Figure 5.31. The projections are visibly consistent with the full multivariate result.

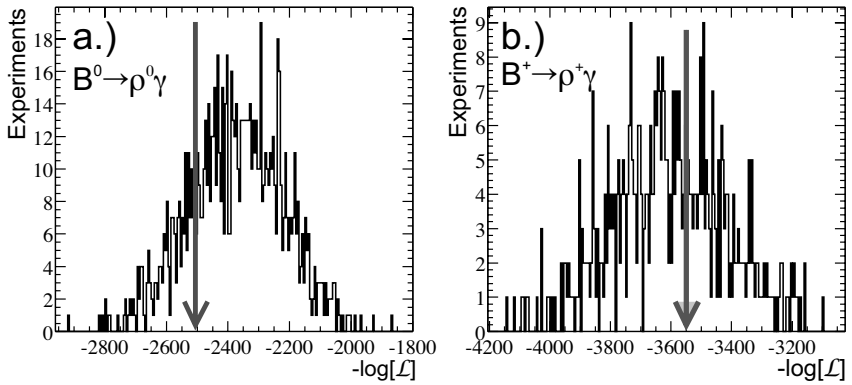

Figure 5.29: Minima of $-\log\mathcal{L}$ of the signal extraction fit (arrow) compared with toy Monte Carlo distributions for a.) $B^0 \to \rho^0\gamma$ and b.) $B^+ \to \rho^+\gamma$).

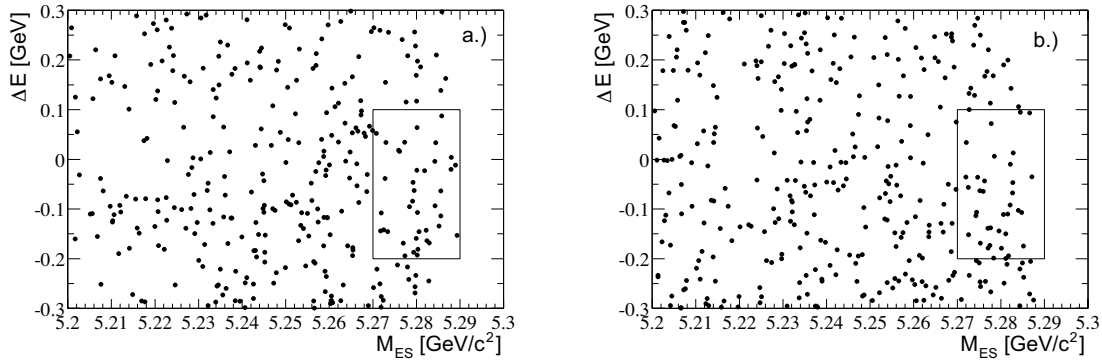

Figure 5.30: ΔE^* vs. M_{ES} distributions for a.) $B^0 \to \rho^0\gamma$ and b.) $B^+ \to \rho^+\gamma$.

In the absence of a significant signal yield, we set 90% confidence level limits on the branching fractions. We determine the 90% confidence level maximum yield allowed by the observed data by refitting the data with increasing fixed signal yield and evaluating the $-\log\mathcal{L}$ of the fit as show in Figure 5.32. The maximum yield is defined as the point at which the $-\log\mathcal{L}$ of the fit deviates by 0.82 (corresponding to a two-sided 90% confidence level interval) from the minimum $-\log\mathcal{L}$ which defines the central value. For conservatism, we subtract the minimum observed bias from our systematic studies: for $B^0 \to \rho^0\gamma$ we *add* 0.5 events, and for $B^+ \to \rho^+\gamma$, we add 0.1 events to the signal yield. This yield is then divided by the signal efficiency

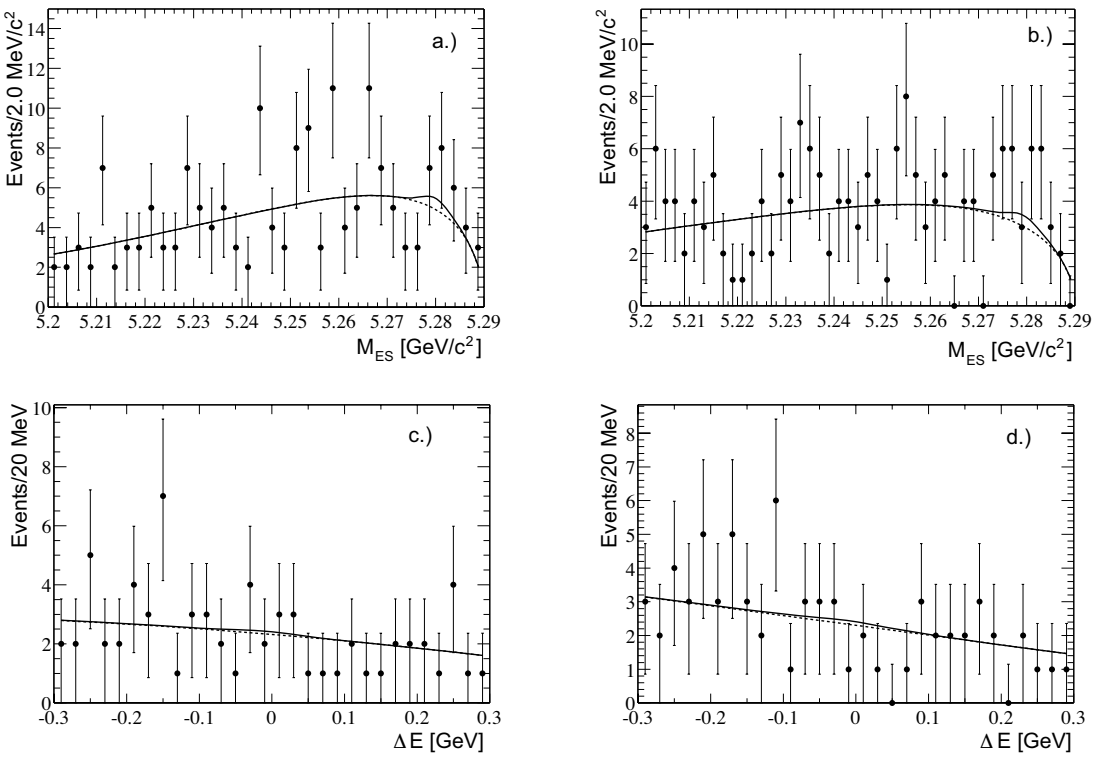

Figure 5.31: Fit projections: $m_{\rm ES}$ fit projections for a.) $B^0 \to \rho^0\gamma$ and b.) $B^+ \to \rho^+\gamma$ for candidates with $-0.2 < \Delta E^* < 0.1\,\text{GeV}$. ΔE^* fit projections for c.) $B^0 \to \rho^0\gamma$ and d.) $B^+ \to \rho^+\gamma$ for candidates with $m_{\rm ES} > 5.27\,\text{GeV}/c^2$.

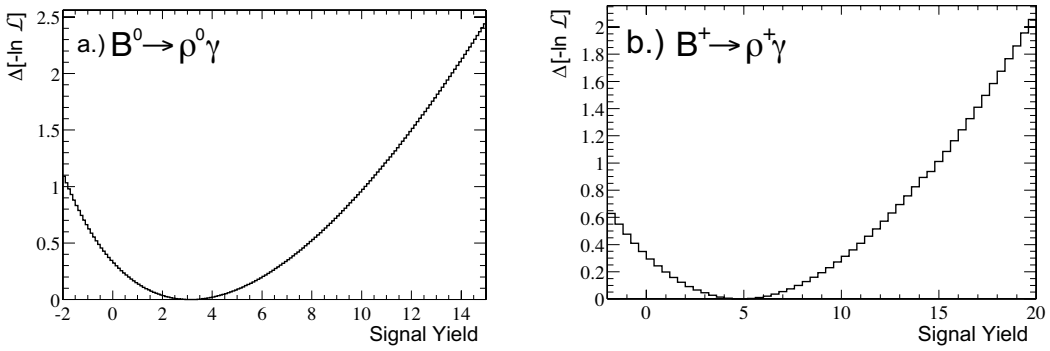

Figure 5.32: Change in $-\log\mathcal{L}$ as a function of signal yield with all other fit parameters allowed to float.

reduced by one standard deviation of the systematic uncertainty to determine the corresponding yield of events in the dataset. Finally, to obtain the branching fraction, we divide by the estimated number of $B\overline{B}$ events in the sample, again lowered by one standard deviation. The procedure is tabulated in Table 5.12, resulting in $\mathcal{B}[B^0 \to \rho^0\gamma] < 1.5 \times 10^{-6}$ and $\mathcal{B}[B^+ \to \rho^+\gamma] < 2.8 \times 10^{-6}$.

Chapter 6

Conclusions

6.1 Interpretation of Results

The results of the $B \to K^*\gamma$ and $B \to \rho\gamma$ analyses are summarized in Tables 6.1 and 6.2 together with the CLEO measurements and recent preliminary results from the BELLE collaboration. The predictions of Ali and Parkhomenko [24] are also shown as a representative theoretical prediction.

6.1.1 $B \to K^*\gamma$ Analysis

The *BABAR* $B \to K^*\gamma$ measurements represent an improvement in precision over the the CLEO results as expected from the increase in statistics. The preliminary BELLE result represents an update of their analysis with approximately three times more data. The branching fraction measurements from the three experiments are compatible, and no experiment observes evidence for direct CP violation. The theoretical predictions of the branching fraction are all quite high; nearly twice the experimental measurements. It has been suggested that the form factor $F_1^{B\to K^*}(0)$ calculated in the light cone sum rule approach used in these calculations may be incorrect. The basis for this is that the predicted ratio $\zeta = F_1^{B\to\rho}(0)/F_1^{B\to K^*}(0) = 0.76 \pm 0.06$ in this approach suggests a significantly higher form factor for the $B \to K^*$ transition

	$B\overline{B}$ ($/10^6$)	$\mathcal{B}[B^0 \to K^{*0}\gamma]$ ($/10^{-5}$)	$\mathcal{B}[B^+ \to K^{*+}\gamma]$ ($/10^{-5}$)	A_{CP} (%)
BABAR	22.7	$4.23 \pm 0.40 \pm 0.22$	$3.83 \pm 0.62 \pm 0.22$	$-4.4 \pm 7.6 \pm 1.2$
CLEO [31]	9.7	$4.55 \pm 0.70 \pm 0.34$	$3.76 \pm 0.89 \pm 0.28$	$8.0 \pm 13.0 \pm 3.0$
BELLE (prelim.)[53]	31.7	$4.08 \pm 0.35 \pm 0.26$	$4.92 \pm 0.59 \pm 0.37$	$3.2 \pm 6.9 \pm 2.0$
Ali and Parkhomenko		7.2 ± 2.7	7.2 ± 2.7	$< 0.5\%$

Table 6.1: Experimental results on $B \to K^*\gamma$ with theoretical predictions

	$B\overline{B}$ ($/10^6$)	$\mathcal{B}[B^0 \to \rho^0\gamma]$ ($/10^{-6}$)	$\mathcal{B}[B^+ \to \rho^+\gamma]$ ($/10^{-6}$)
BABAR	61.7	< 1.5	< 2.8
CLEO [31]	9.7	< 17	< 13
BELLE (prelim.) [55]	45.1	< 5.7	< 7.2
Ali and Parkhamenko		0.5 ± 0.2	0.9 ± 0.4

Table 6.2: Experimental results on $B \to \rho\gamma$ with theoretical predictions

relative to the $B \to \rho$ transition. Due to the hard recoil of the daughter meson relative to its mass in this process, it is difficult to explain why the two processes should be so different [54]. Indeed, the lattice QCD calculations suggest that the difference is small, albeit in a different kinematic region [19]. A comparison of $F_1^{B\to K^*}(q^2)$ calculated using the light cone sum rule to the points obtained in the lattice QCD calculations shows that the former are consistently higher. Together, these arguments suggests that the $F_1^{B\to K^*}(0)$ form factor obtained by this method may be artificially high, resulting in a similar artificial enhancement of $\mathcal{B}[B \to K^*\gamma]$.

6.1.2 $B \to \rho\gamma$ Analysis

The limits obtained on $\mathcal{B}[B \to \rho\gamma]$ represent a significant improvement over the published CLEO results. While the improvement is due in part to the large increase in statistics, this accounts for only a factor of ~ 2.5 in sensitivity. The additional gain in sensitivity (a total of about a factor of ten in $\mathcal{B}[B^0 \to \rho^0\gamma]$ and five in

$\mathcal{B}[B^+ \to \rho^+\gamma]$) can be attributed to the improved background suppression and signal extraction techniques. A preliminary BELLE result is also shown in Table 6.2 [55]. Even the most optimistic prediction of $\mathcal{B}[B^+ \to \rho^+\gamma] = 1.53 \times 10^{-6}$ [22] is a factor of two lower than the *BABAR* limits.

A bound on $|V_{td}/V_{ts}|$ can be obtained from Equation 1.24 using the limits on $\mathcal{B}[B \to \rho\gamma]$ and the measurement of $\mathcal{B}[B \to K^*\gamma]$. By assuming isospin symmetry ($2 \times \mathcal{B}[B^0 \to \rho^0\gamma] = \mathcal{B}[B^+ \to \rho^+\gamma] \equiv \mathcal{B}[B \to \rho\gamma]$), the likelihood curves for the two modes can be combined to obtain a single limit $\mathcal{B}[B \to \rho\gamma] < 2.3 \times 10^{-6}$. This results in a limit on the ratio $\mathcal{B}[B \to \rho\gamma]/\mathcal{B}[B \to K^*\gamma] < 0.06$. Taking the conservative limits on the parameters $\zeta = 0.7$ and $\Delta R = -0.25$, we derive a limit $|V_{td}/V_{ts}| < 0.4$.

An more detailed analysis of the constraint has been performed by Ali and Lunghi [56]. The result is conveniently summarized in the unitarity triangle shown in Figure 6.1. The figure shows the bound expressed as a maximum radius from the lower right point of the unitarity triangle. The bound is compared to analogous constraints from B^0_d mixing and B_s mixing; while the bound from $\mathcal{B}[B \to \rho\gamma]$ is still not competitive, with an additional factor of two in sensitivity of $\mathcal{B}[B \to \rho\gamma]$, non-trivial constraints will be possible. Observation of $B \to \rho\gamma$ will also constrain the radius from within.

6.2 Future Prospects

The *BABAR* detector continues to accumulate data at a rapid rate. Within a few years, it is likely that a sample of $B\overline{B}$ events an order of magnitude larger than that analyzed here will be available for analysis.

For $B \to K^*\gamma$, the branching fractions are likely to be measured with such precision (a few percent) that systematic uncertainties may be become dominant. We have already shown that $B \to K^*\gamma$ is a useful experimental testing ground for more challenging searches like $B \to \rho\gamma$. It is likely that precision measurements of $B \to K^*\gamma$ branching fractions may likewise become a testing ground for the theory of B decays as theorists improve their calculations. Currently, there is considerable theoretical interest in $B \to K^*\gamma$ phenomenology in the form of predictions of isospin violation

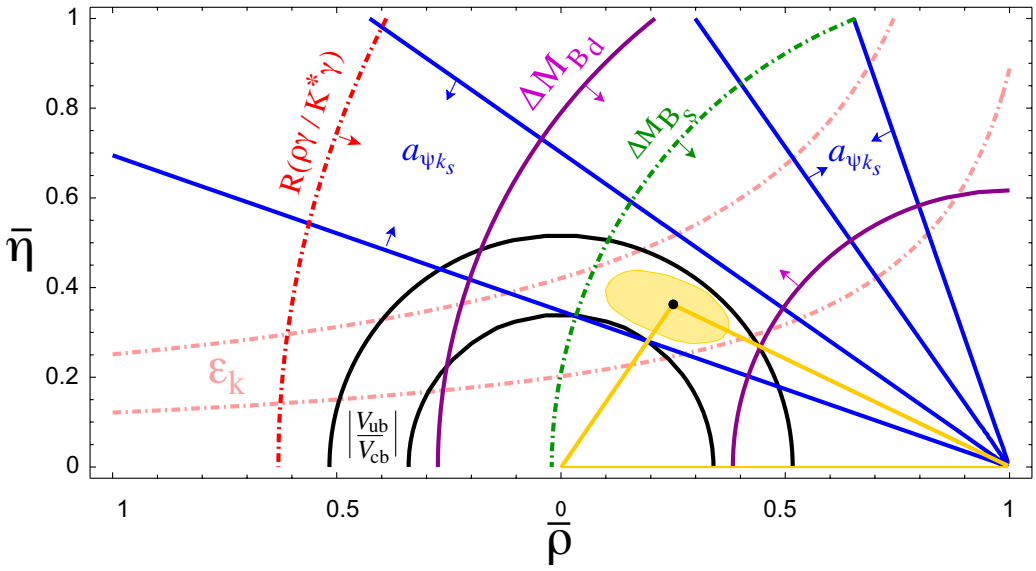

Figure 6.1: Current experimental constraints on the CKM Unitarity Triangle [56].

(where $\mathcal{B}[B^+ \to K^{*+}\gamma] \neq \mathcal{B}[B^0 \to K^{*0}\gamma]$) and CP violation. With larger data sets and more precise measurements, we may soon be able to conclusively confirm or refute these predictions. Since the theoretical framework for these predictions is rather general and applied to the study of many decay modes of the B meson, such comparisons will have general ramifications for the robustness of these theoretical approaches.

For $B \to \rho\gamma$, despite the substantial gains in sensitivity realized in this analysis from a considerably larger data sets and better background suppression, we are still quite far from making an observation of this mode. Limits on $\mathcal{B}[B \to \rho\gamma]$ that would impose non-trivial constraints on the CKM matrix require about a factor of two in sensitivity over the current limits; this can be accomplished with four times more data. At *BABAR*, this may be forthcoming on the time scale of two years.

It is desirable, however, to make a significant observation of this mode. In this case, improvements in the analysis are necessary. There are several areas in which gains in sensitivity can be made. First, the net flavor information used in the neural network is far from the optimal use of this information. Separately categorizing the flavor

into electron, muon and kaon-tagged tracks and using the the momentum of the track may afford significant increases in sensitivity. Second, the rejection of π^0 and η candidates might be improved by a more general veto. The current veto does not reject cases where the photon accompanying the decay converts in the material or proceeds through an internal conversion process (Dalitz decay). The veto will also fail if a track is mistakenly matched to the EMC deposition created by the accompanying photon in the π^0/η decay. If explicitly reconstructed conversion candidates, as well as single electron candidates and charged EMC depositions are also paired with the photon candidate in the veto, it may be possible to reject some part of this background. A third possibility is to include the neural network in the signal extraction fit rather than imposing a selection on it. It is hoped that some or all of these possible improvements can be explored in the next iteration of the analysis with significant enhancement in the sensitivity.

Bibliography

[1] A. Einstein, Annalen Phys. **17**, 891 (1905).

[2] V. Fock, Z. Phys. **39**, 226 (1926) [Surveys High Energ. Phys. **5**, 245 (1926)].

H. Weyl, Z. Phys. **56**, 330 (1929) [Surveys High Energ. Phys. **5**, 261 (1929)].

O. Klein, *New Theories of Physics*, 77,
Intern. Inst. of Intellectual cooperation, League of Nations

C. N. Yang and R. L. Mills, Phys. Rev. **96**, 191 (1954).

[3] Y. Nambu, Phys. Rev. Lett. **4**, 380 (1960).

J. Goldstone, Nuovo Cim. **19**, 154 (1961).

J. Goldstone, A. Salam and S. Weinberg, Phys. Rev. **127**, 965 (1962).

P. W. Higgs Phys. Lett. **12**, 132 (1964).

P. W. Higgs, Phys. Rev. **145**, 1156 (1966).

[4] M. Y. Han and Y. Nambu, Phys. Rev. **139**, B1006 (1965).

[5] S. Weinberg, Phys. Rev. Lett. **19**, 1264 (1967).

A. Salam, *Originally printed in *Svartholm: Elementary Particle Theory, Proceedings Of The Nobel Symposium Held 1968 At Lerum, Sweden*, Stockholm 1968, 367-377.*

S. L. Glashow, Nucl. Phys. **22**, 579 (1961).

[6] M. Kobayashi and T. Maskawa, Prog. Theor. Phys. **49**, 652 (1973).

[7] S. L. Glashow, J. Iliopoulos and L. Maiani, Phys. Rev. D **2**, 1285 (1970).

[8] S. Weinberg, Phys. Rev. Lett. **27**, 1688 (1971).

[9] E. C. Stueckelberg and A. Petermann, Helv. Phys. Acta **26**, 499 (1953).

M. Gell-Mann and F. E. Low, Phys. Rev. **95**, 1300 (1954).

C. G. Callan, Phys. Rev. D **2**, 1541 (1970).

K. Symanzik, Commun. Math. Phys. **34**, 7 (1973).

[10] K. G. Wilson, Phys. Rev. **179**, 1499 (1969).

[11] S. Bertolini, F. Borzumati and A. Masiero, Phys. Rev. Lett. **59**, 180 (1987).

N. G. Deshpande, P. Lo, J. Trampetic, G. Eilam and P. Singer, Phys. Rev. Lett. **59**, 183 (1987).

[12] . Adel and Y. P. Yao, Phys. Rev. D **49**, 4945 (1994) [hep-ph/9308349].

K. Chetyrkin, M. Misiak and M. Munz, Phys. Lett. B **400**, 206 (1997) [Erratum-ibid. B **425**, 414 (1997)] [hep-ph/9612313].

[13] C. Greub, T. Hurth and D. Wyler, Phys. Rev. D **54**, 3350 (1996) [hep-ph/9603404].

[14] V. L. Chernyak and A. R. Zhitnitsky, JETP Lett. **25**, 510 (1977) [Pisma Zh. Eksp. Teor. Fiz. **25**, 544 (1977)].

G. P. Lepage and S. J. Brodsky, Phys. Lett. B **87**, 359 (1979).

[15] I. I. Balitsky, V. M. Braun and A. V. Kolesnichenko, Deep Inelastic Scattering From Polarized Targets," Phys. Lett. B **242**, 245 (1990) [Erratum-ibid. B **318**, 648 (1990)] [hep-ph/9310316].

V. L. Chernyak and I. R. Zhitnitsky, Nucl. Phys. B **345**, 137 (1990).

[16] K. G. Wilson, Phys. Rev. D **10**, 2445 (1974).

[17] A. Ali, V. M. Braun and H. Simma, Z. Phys. C **63**, 437 (1994) [hep-ph/9401277].

[18] P. Ball and V. M. Braun, Phys. Rev. D **58**, 094016 (1998) [hep-ph/9805422].

[19] L. Del Debbio, J. M. Flynn, L. Lellouch and J. Nieves [UKQCD Collaboration], Phys. Lett. B **416**, 392 (1998) [hep-lat/9708008].

[20] P. Ball, [hep-ph/9308244].

[21] E. V. Shuryak, Phys. Lett. B **93**, 134 (1980).

E. Eichten and F. Feinberg, Phys. Rev. D **23**, 2724 (1981).

W. E. Caswell and G. P. Lepage, Phys. Lett. B **167**, 437 (1986).

B. Grinstein, Nucl. Phys. B **339**, 253 (1990).

A. F. Falk, B. Grinstein and M. E. Luke, Nucl. Phys. B **357**, 185 (1991).

[22] S. W. Bosch and G. Buchalla, Nucl. Phys. B **621**, 459 (2002) [hep-ph/0106081].

[23] M. Beneke, T. Feldmann and D. Seidel, Nucl. Phys. B **612**, 25 (2001) [hep-ph/0106067].

[24] A. Ali and A. Y. Parkhomenko, Eur. Phys. J. C **23**, 89 (2002) [hep-ph/0105302].

[25] M. Bander, D. Silverman and A. Soni, Phys. Rev. Lett. **43**, 242 (1979).

[26] A. L. Kagan and M. Neubert, Phys. Rev. D **58**, 094012 (1998) [hep-ph/9803368].

[27] B. Grinstein and D. Pirjol, Phys. Rev. D **62**, 093002 (2000) [hep-ph/0002216].

[28] B. Aubert *et al.* [BABAR Collaboration], Nucl. Instrum. Meth. A **479**, 1 (2002) [hep-ex/0105044].

[29] Fluorinert (polychlorotrifluoro-ethylene) is manufactured by the 3M Corporation.

[30] R. Brun, R. Hagelberg, M. Hansroul and J. C. Lassalle, CERN-DD-78-2-REV.

[31] T. E. Coan *et al.* [CLEO Collaboration], Phys. Rev. Lett. **84**, 5283 (2000) [hep-ex/9912057].

[32] S. Chen *et al.* [CLEO Collaboration], Phys. Rev. Lett. **87**, 251807 (2001) [hep-ex/0108032].

[33] Y. Ushiroda [Belle collaboration], [hep-ex/0104045].

[34] G. C. Fox and S. Wolfram, Phys. Rev. Lett. **41**, 1581 (1978).

[35] J. Bauer *BABAR* Note 521 (2001)

[36] D. E. Groom *et al.* [Particle Data Group Collaboration], Eur. Phys. J. C **15**, 1 (2000).

[37] M. Procario *et al.* [CLEO Collaboration] Phys. Rev. Lett. **70**, 1207 (1993).

[38] E. Varnes *et al. BABAR* Analysis Document 157 (2001)

[39] C. Hearty *BABAR* Analysis Document 135 (2001)

[40] C.P. Jessop *et. al BABAR* Analysis Document 33 (2001)

[41] T. Colberg *et. al BABAR* Analysis Document 196 (2001)

[42] H.Albrecht *et. al*, Z. Phys. C **4**8 543 1990

[43] C. Touramanis *et. al BABAR* Analysis Document 20 (2000)

[44] S. Spanier *et. al BABAR* Analysis Document 116 (2001)

[45] R. Faccini *et. al BABAR* Analysis Document 19 (2000)

[46] F. Martinez-Vidal *et. al BABAR* Analysis Document 102 (2001)

[47] U. Langenegger *et. al BABAR* Analysis Document 90 (2001)

[48] C. Hearty *et. al BABAR* Analysis Document 126 (2001)

[49] http://www-ra.informatik.uni-tuebingen.de/SNNS

[50] H. Hu *et. al* *BABAR* Analysis Document 103 (2000)

[51] C. P. Jessop *et al.* [CLEO Collaboration], Phys. Rev. Lett. **85**, 2881 (2000) [hep-ex/0006008].

[52] K. S. Cranmer, ALEPH internal note 99-144 (1999)

[53] A. Ishikawa [Belle collaboration], [hep-ex/0205051.

[54] Gudrun Hiller, private communications.

[55] H. Kim, [Belle collaboration], presented at the meeting of the Division of Particles and Fields of the American Physical Society, Williamsburg, VA, May 2002. [hep-ex/0205051].

[56] A. Ali and E. Lunghi, [hep-ph/0206242].